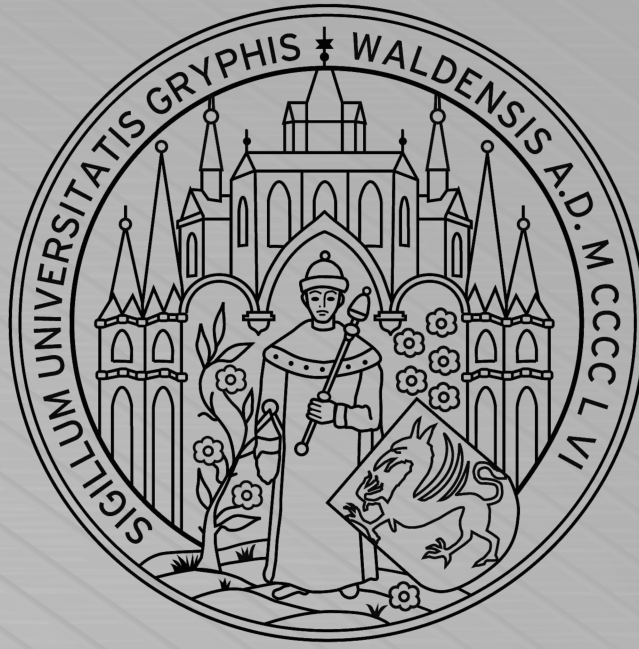Nils Fahrenkamp

A Helicon Plasma Source for Wakefield Accelerators

A Helicon Plasma Source for Wakefield Accelerators

Inauguraldissertation

Nils Fahrenkamp

Mathematisch-Naturwissenschaftliche Fakultät

Universität Greifswald

A Helicon Plasma Source for Wakefield Accelerators

I n a u g u r a l d i s s e r t a t i o n

zur

Erlangung des akademischen Grades eines

Doktors der Naturwissenschaften (Dr. rer. nat.)

der

Mathematisch-Naturwissenschaftlichen Fakultät

der

Universität Greifswald

vorgelegt von

Nils Fahrenkamp

Greifswald, 21. Januar 2019

Dekan:	Prof. Dr. W. Weitschies
1. Gutachter:	Prof. Dr. T. Klinger
2. Gutachter:	Prof. Dr. J. Benedikt
Tag der Promotion:	20.05.2019

"Everything not saved will be lost"

Nintendo "Quit Screen" message

Contents

Chapter 1

Introduction

The term "plasma" was introduced by Irving Langmuir [1928] to describe ionized gases in electric discharges. Plasma is a peculiar state of matter with ionization degrees varying from 0.001% to 100% [Bogaerts et al., 2002]. Even a discharge with a low ionization degree exhibits plasma behavior due to the long range Coulomb forces between the charged particles [Zohm, 2012]. Characteristic for a plasma is an electric conductivity due to the mobility of unbound charged particles. Consequently, a plasma is affected by electromagnetic fields. A plasma usually emits light and is a complex mixture of electrons, ions (positively or negatively charged), as well as neutral atoms and molecules, except for the electrons mostly in excited electronic, vibrational or rotational states [Abdalla, 2004]. Electrons play an important role with their small mass and high mobility as constituent for ionization, dissociation and excitation by collisions with neutral atoms and molecules.

More than 99% of the visible matter in our universe is in the plasma state with naturally occuring plasmas like stars, interstellar gas, the planets' ionosphere and magnetosphere and solar winds [Bogaerts et al., 2002]. Space plasma physics and astrophysics are the key research fields dealing with natural plasmas. Astrophysical plasmas have an extreme variation in density and temperature. In the interstellar space the particle densities vary from $0.1 - 10^{15}\,\mathrm{m^{-3}}$ and the temperatures from $1 - 100\,\mathrm{eV}$. Under more extreme conditions, like in the interior of sun-like stars, the particle density goes up to $10^{32}\,\mathrm{m^{-3}}$ at a temperature of up to $1.5\,\mathrm{keV}$. Technological plasmas are driven by an externally applied power source to sustain the plasma state. In plasma processing material on surfaces is physically removed

by collisions or chemically by reactions with plasma constituents [Hopkins, 2000] [Schulz-von der Gathen, 1996].

During the last decades plasmas have been used to accelerate electrons to energies of multi − GeV [Muggli, 2009]. In this high energetic regime, elementary particle and subatomic processes can be investigated, see figure 1.1. Albeit many are known and well understood, there is certainly new physics beyond today's limits in particle acceleration energy. It is supposed to arise at energies, scales and precisions far greater than e.g. the Large Hadron Collider (LHC) is capable to provide. The need for higher energies in particle colliders led to the development
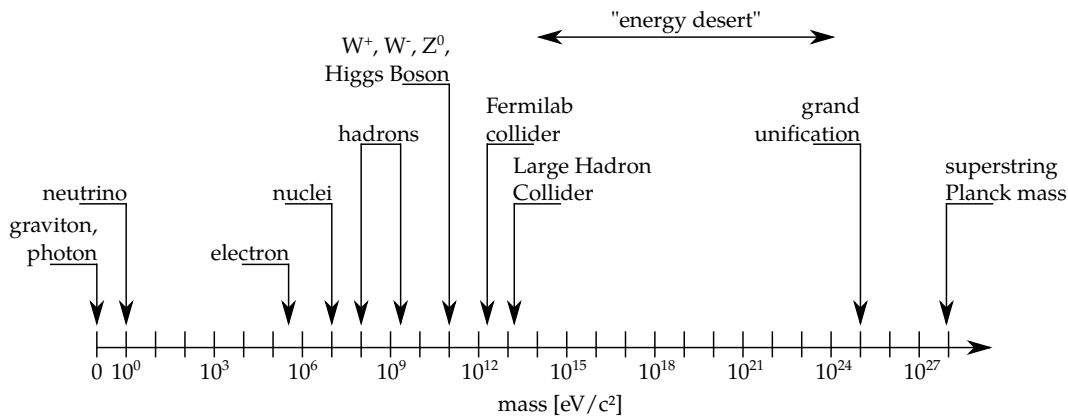
Figure 1.1: Comparison of masses for different particles and the maximum center-of-mass energy for two colliders, Fermilab collider and Large Hadron Collider. The "energy desert" represents the unknown energy area to the point of the grand unification, where all known and unknown particles are included.

of several types of particle accelerators over the last decades. They are either better suitable for hadrons (e.g. protons and anti-protons) or leptons (e.g. electrons and positrons). Circular accelerators exhibit an energy frontier of several TeV for hadrons but just 100 GeV for leptons. High energy losses via synchrotron radiation set limits on the achievable lepton energy [Holzer, 2017]. In particular, to reach the TeV regime for leptons a circular collider with a radius of over 100 km would be needed. Therefore linear colliders are usually preferred for lepton acceleration. The key issue here is the maximum achievable acceleration gradient. At present metallic RF-cavities with an acceleration gradient of up to 30 MV/m still lead to dimensions of more than 30 km accelerator length for particle energies of 1 TeV [Aicheler et al., 2012]. The investigation of new acceleration approaches is therefore desirable. Promising concepts are plasma-based accelerators.

A characteristic feature of plasmas is that a relatively small charge imbalance between electrons and ions result in large electrostatic fields. This has attracted a lot of attention in the field of high-energy physics since the achievable electric fields in a plasma in the order of GV/m exceed by orders of magnitude the conventional electric field generation by RF cavities and scales with the plasma density $E(n)$. These electric fields, however, cannot exist as a stationary case since the charge imbalance would be quickly restored to a quasi-neutral situation. For the displacement of charges an energetic driver is required. Several schemes have been proposed to the non-stationary large electric fields for particle acceleration. The most promising concept up to now is the laser-driven wakefield accelerator [Tajima, 1979], but it fails to accelerate to TeV energy: Assuming an adequate number of electrons of 10^{10} reaching $1\,\mathrm{TeV}$ in energy, the laser has to provide a power of $P = 10^{10} \cdot 1.6 \cdot 10^{-19}\,\mathrm{C} \cdot 1\,\mathrm{TeV} \approx 100\,\mathrm{kJ}$ just for the purpose of particle acceleration assuming an energy transformation efficiency of 100%. Even with modern laser technologies or the coupling of multiple laser this power is hardly achievable. Circular accelerators, like the LHC at CERN, are able to provide an energy of several TeV for 10^{11} protons. This brings another type of plasma wakefield accelerator for high particle energies into play, the proton driven wakefield accelerator [Caldwell et al., 2016]. Here, a relativistic proton bunch serves as drive to induce plasma wakefields, i.e. electric fields to accelerate an electron bunch in a linear plasma column. This means the circular accelerator is used as a driver for linear wakefield accelerators. A current experiment as design study is the AWAKE project [Gschwendtner et al., 2016]. First results in a linear plasma test chamber are encouraging [Adli et al., 2018]. There are still problems to overcome, e.g. total efficiency, beam quality and repetition rate, but it is a promising approach worth studying. To realize a plasma wakefield accelerator, homogeneous, high density plasma columns of $n_\mathrm{e} \approx 10^{21}\,\mathrm{m}^{-3}$ with a low variation in plasma density are needed [Assmann et al., 2014]. The plasma must be centrally peaked with a sufficient discharge duration for moving and accelerating electrons. The plasma cell to be developed must be modular and scalable to the needed target length of up to several $100\,\mathrm{m}$. Such a plasma can be maintained, in principle, by a helicon discharge but it is challenging to achieve the required high plasma density and homogeneity. It is the goal of the present thesis to investigate the temporal evolution of radial plasma parameter profiles, in particular for neutral and charged plasma species and corresponding electron temperatures and plasma densities.

The following questions arise: Do the helicon wave properties support high density plasma columns of $n_e \approx 10^{21}\,\mathrm{m}^{-3}$, are they centrally peaked and reproducable? Does the electron temperature correspond to the principle of helicon wave heating? Does the high plasma density interval last long enough for a proton bunch to pass a whole wakefield accelerator? Is a plasma density limit visible and what operational parameters show the maximum plasma density? Does neutral depletion in the center of the discharge influence the density evolution and maximum plasma density?

The content of this thesis is structured in four main parts: Chapter 2 and 3, 4, 5, and 6. The first main part reviews the necessity of particle-driven plasma wakefield accelerators combined with helicon discharges. In chapter 2 the theory, concepts and limitations of conventional accelerators and particle-driven wakefield accelerators are described. Chapter 3 deals with different radio-frequency discharge types and describes their characteristics and properties. The following chapter 4 introduces a zero dimensional reaction rate model to study the main generation reactions of ions and metastable states in a low-pressure, high-density argon plasma. The principle, the included energy levels and reactions are presented. The calculated densities and rates for varying neutral gas pressures and electron temperatures are shown to quantitatively compare them with the experimental results in the discussions. The experimental set-up, diagnostics and data processing methods are briefly reviewed in chapter 5. Special emphasis is put on a correction function for profile measurements and the laser induced fluorescence technique, an active spectroscopic diagnostic to non-invasively observe ion dynamics, to combine line intensity ratio measurements, laser interferometer results, and the reaction rate model for the calculation of time-resolved electron temperature profiles. In chapter 6 measurements on time-resolved plasma density and laser-induced fluorescence profiles, their dependencies on operational parameters and the calculated electron temperature profiles are presented. The main findings made in this thesis and the conclusions are summarized in chapter 7.

Chapter 2

Plasma wakefield acceleration

To study the basic laws of our universe particle accelerators are the main research tools in the high energy physics community. Experiments conducted at the Large Hadron Collider (LHC) at CERN in Switzerland or at the planned International Linear Collider (ILC) in Japan will give new perceptions into the world around us. To resolve inter- and subatomic processes, as shown in figure 2.1, energies of several TeV are needed. Some representative processes are the production and decay of W or Z bosons or the top-quark for hadronic collisions or electron-positron annihilation processes in electron colliders [Weiglein, 2004]. The energy frontier for experiments in particle physics are currently several TeV, but circular colliders in this energy regime for leptons are very costly and time-consuming to build, thus they are not feasible at these energies. Hence, lepton accelerator designs reaching the TeV regime are based on linear colliders. However, as the proposed beam energy increases, also the costs and scale of linear accelerators become very large, depending on the increasing accelerating gradient in radiofrequency (RF) cavities. Nowadays, the usual metallic cavities achieve accelerating gradients around $30\,\mathrm{MV/m}$, which results in a length of tens of kilometers to reach even the sub-TeV scale as shown in figure 2.3 and table 2.1 for the ILC. Therefore it is meaningful to investigate new methods of accelerating particles to energies in the $10 - 100\mathrm{TeV}$ regime. Direct laser acceleration of electrons in free-space would be a simple assumption to make. But no experimental evidence of direct laser acceleration of electrons in vacuum has been reported using cylindrical laser beams [Carbajo et al., 2015]. The reason behind the shortage has lied upon the ineffectiveness to scale up and deliver the intensity requirements to ac-
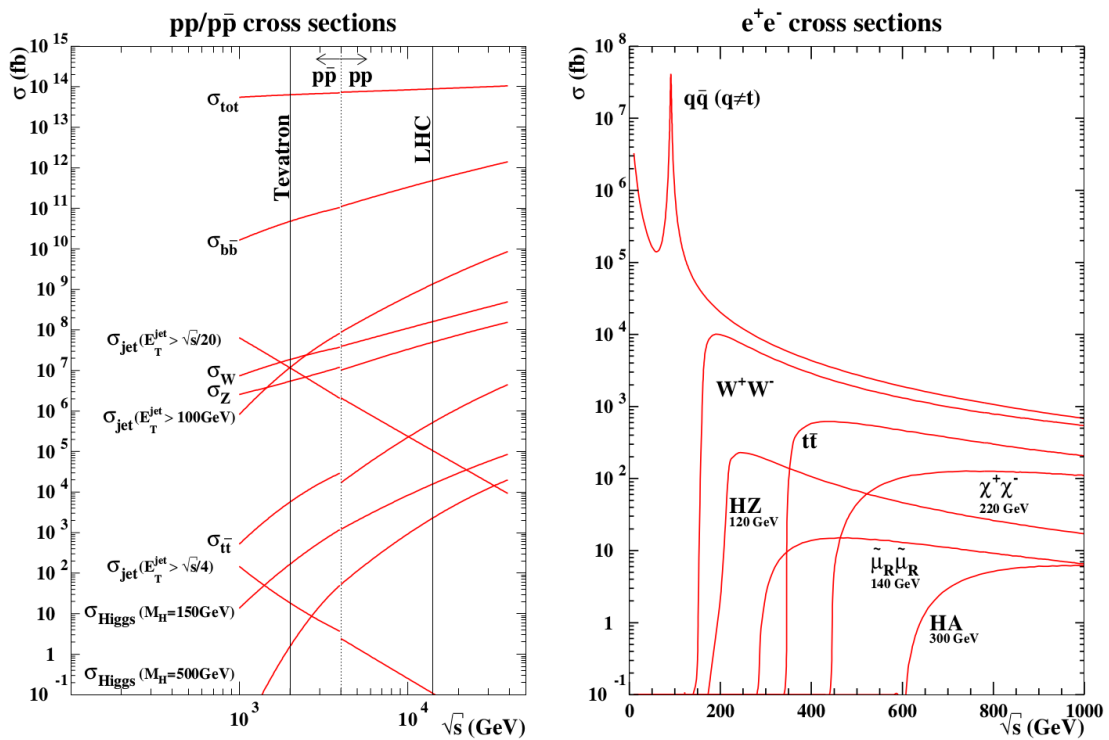
Figure 2.1: Production cross-sections for different processes at hadron colliders (left) and e⁺e⁻ colliders (right) as a function of the center-of-mass energy. The vertical lines in the figure indicate the limit of example accelerators and the dotted line the change of proton-antiproton to proton-proton experiments. The well pronounced peak in the right figure correlates directly to the center-of-mass energy of an e⁺e⁻ pair. Figures taken from [Weiglein, 2004].

cess the relativistic regime of laser-electron interaction well above $1 \cdot 10^{19}$ W/cm^2 for optical pulses [Carbajo et al., 2015]. But even if possible to effectively accelerate particles with high electromagnetic laser fields in the focal point of the beam, a staging with several laser accelerators would be necessary to reach the TeV regime. Plasma-based accelerator concepts are of high interest because they are able to produce accelerating fields, orders of magnitude larger than those in conventional colliders [Tajima, 1979][Chen et al., 1985][Joshi et al., 1984]. Here the plasma wakefield accelerator is the most promising concept being developed [Chen et al., 1985][Ruth et al., 1985][Esarey et al., 2009]. Simply speaking, a plasma is a medium consisting of free ions and electrons. This is why it can maintain very large electric fields in the order of GV/m [Esarey et al., 1996] [Leemans et al., 2006]. Just over the last few decades, remarkable progress has been made. Acceleration gradients more than three orders of magnitude higher than in RF cavities have been demonstrated in laboratory plasmas [Blumenfeld et al., 2007][Tajima, 1979]. One can generally say that a plasma can act as an energy transformer. Current proton synchrotrons are able to produce high energy, multi TeV protons, but not TeV leptons. If possible to efficiently transfer this energy from a proton bunch or a laser (driver) to an electron bunch (witness bunch) via plasma, a new accelerator frontier would be opened.

2.1 Conventional accelerators

Particle accelerators were invented in the late 1920's to supply high energetic particles for the investigation of the inner structure of nuclei. Meanwhile this technique has been used in other areas of physics, biology and medicine [Barbalat, 1994][USdoe, 2018]. Simply put, this apparatus accelerates and thus increases the kinetic energy of a beam of charged particles by generating electric fields for acceleration and it steers and focuses these particles by magnetic fields. There are two main types of accelerators, circular and linear ones.

The principles for a linear particle accelerator (LINAC) were proposed by Ising [1924]. The kinetic energy of charged particles is increased by exposing them to a series of accelerating electric potentials along the beamline as depicted in figure 2.2. While the particle bunch, produced by an ion source, passes one of the metal drift tubes, it remains unaffected. If the particles cross the gap between the drift tubes, they will be accelerated due to the presence of an axial electric

field produced by different potentials attached to the tubes. Subsequently the potentials switch signs to accelerate the particles further in the next gap. The energy gain after the nth step is [Holzer, 2017]

$$E_n = nqU_0 \sin \psi_\mathrm{s}, \tag{2.1}$$

where n denotes the acceleration step, q the charge of the particle, U_0 the applied voltage per gap, and ψ_s the phase between the particle and the AC voltage. The driving frequency of the signal, the length and the spacing between the drift tubes are designed in a way that the maximum voltage difference appears as the particles cross the gap. The time-span of an accelerating half-wave of the driving frequency is defined by the period of the applied frequency, $\Delta t = \tau_\mathrm{RF}/2$. So that the length of the nth drift tube is defined by

$$l_n = v_n \frac{\tau_\mathrm{RF}}{2}, \tag{2.2}$$

with v_n as particle velocity and τ_RF as the period of the RF driving frequency. Taking the kinetic energy of the particle

$$E_\mathrm{kin} = \frac{1}{2}mv^2, \tag{2.3}$$

into account with m as particle mass, we obtain that

$$l_n = \frac{1}{f_\mathrm{RF}} \sqrt{\frac{nqU_0 \sin \psi_\mathrm{s}}{2m}}, \tag{2.4}$$

with f_RF as RF-frequency is the required length for the nth drift tube. The first working LINAC was constructed at the RWTH Aachen by Winderöe [1928b]. One of the most up to date, but just planned, linear accelerator is the ILC in Japan as shown and described in figure 2.3 with a length of 11 km per LINAC for collision energies of 500 GeV. Nowadays linear accelerators have a variety of application possibilities. They generate X-rays and highly energetic electrons for medical purposes or serve as a particle injector for more powerful accelerators, like it is done at CERN and visualized in figure 2.4. If the energy increases further and the speed of the particles approaches at some point the speed of light, the length of the drift tubes in a linear accelerator will reach dimensions that may no longer be feasible. Taking the given accelerating gradient of table 2.1 and (2.4) into account, the overall length of a LINAC for a maximum achievable electron
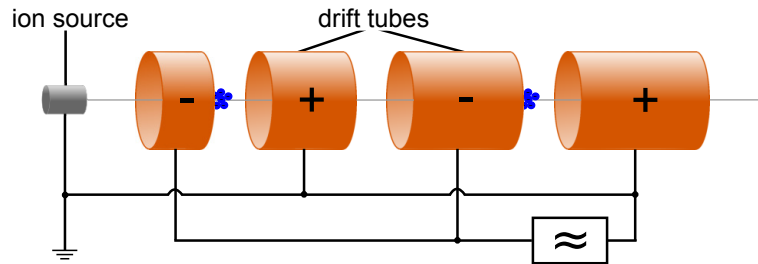
Figure 2.2: Scheme of a linear accelerator. The kinetic energy of charged particles, produced by an ion source, is increased each time the particle bunch passes a gap between the drift tubes. Here they are exposed to an accelerating electric field, produced by different potentials attached to the tubes. While the particle bunch passes one of the metal drift tubes it is unaffected. In the next gap the potentials subsequently switch signs to accelerate the particles further. With increasing velocity the length of the metal tubes have to be increased as well.
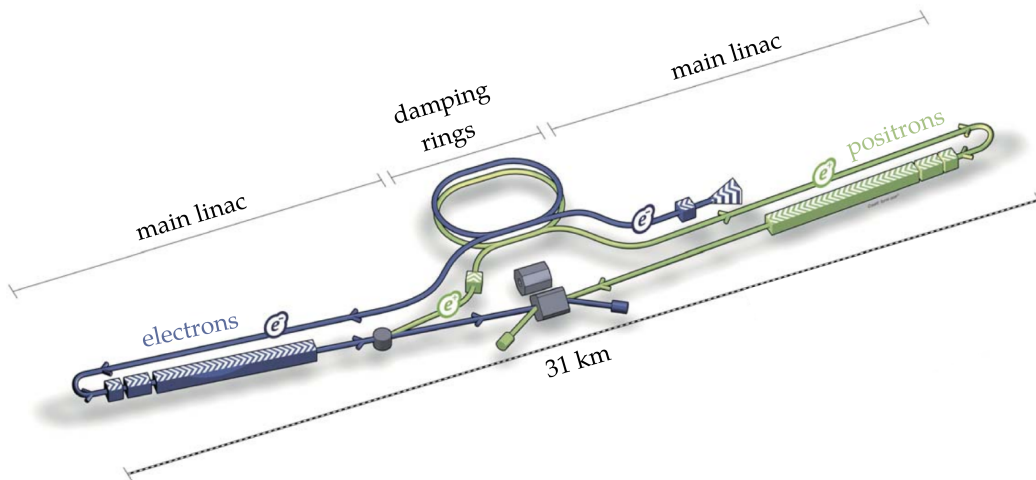
Figure 2.3: Scheme of the ILC accelerator setup, taken from [ILC, 2018]. The electron source is a photocathode ejecting electrons by illuminating it with intense, nanosecond laser light pulses. These electrons are accelerated to $5\,\mathrm{GeV}$ in a $370\,\mathrm{m}$ linac stage (blue). Synchrotron radiation from high energetic electrons in a high power cyclotron produces electron-positron pairs on a titanium-alloy target. The positrons are collected and accelerated to $5\,\mathrm{GeV}$ in a separate linac (green). To reduce the size of the electron and positron bunches sufficiently they circulate in a pair of damping rings with $3.24\,\mathrm{km}$ in circumference. Subsequently the particle bunches are sent to the superconducting RF main linacs of $11\,\mathrm{km}$ in length and accelerated to $250\,\mathrm{GeV}$ each. The bunches are then focused and collide inside one of two particle detectors.

parameter	value
collision energy	$500\,\mathrm{GeV}$
bunch population	$2 \cdot 1010$
number of bunches	1312
bunch spacing	$554\,\mathrm{ns}$
number of collisions	$6560\,\mathrm{s^{-1}}$
acceleration gradient	$31.5\,\mathrm{MW/m}$
RF frequency	$1.3\,\mathrm{GHz}$
power of pulsed RF	$190\,\mathrm{kW/cavity}$
beam size	$474\,\mathrm{nm}\,(\mathrm{width}), 5.9\,\mathrm{nm}\,(\mathrm{thickness})$
circumference of damping ring	$3.2\,\mathrm{km}$
length of main LINAC	$11\,\mathrm{km}$ each
number of detectors	$2\,(\mathrm{push} - \mathrm{pull\ alternation})$

Table 2.1: Specifications of the ILC accelerator setup, taken from [ILC, 2018].

energy of $E_{\mathrm{max}} = 1\,\mathrm{TeV}$ would be approximately $30\,\mathrm{km}$. Thus, the move to circular accelerators was done as a natural step in the historical development process in order to keep the dimensions of the whole accelerators within reasonable limits and to increase the particle energy further. The key idea is to introduce magnetic fields to bend the particle beam into a circle.

A number of different accelerators are joined together in sequence to reach finally particle energies in the TeV regime. Here, the accelerated particle travels around

parameter	value
proton collision energy	$6.5\,\mathrm{TeV}$
electron collision energy	$2.56\,\mathrm{TeV/u}$
number of magnets	9593
number of main dipols	1232
length of main dipols	$15\,\mathrm{m}$
number of main quadrupoles	392
peak magnetic induction	$7.74\,\mathrm{T}$
number of RF cavities	$8\,\mathrm{per\ direction}$
bunch population	$1.2 \cdot 10^{11}$
number of bunches	2808
number of collisions	$1 \cdot 10^9\,\mathrm{s^{-1}}$
circumference of ring	$26.66\,\mathrm{km}$
number of detectors	7

Table 2.2: Specifications of the LHC accelerator setup, taken from [EG CERN, 2017].
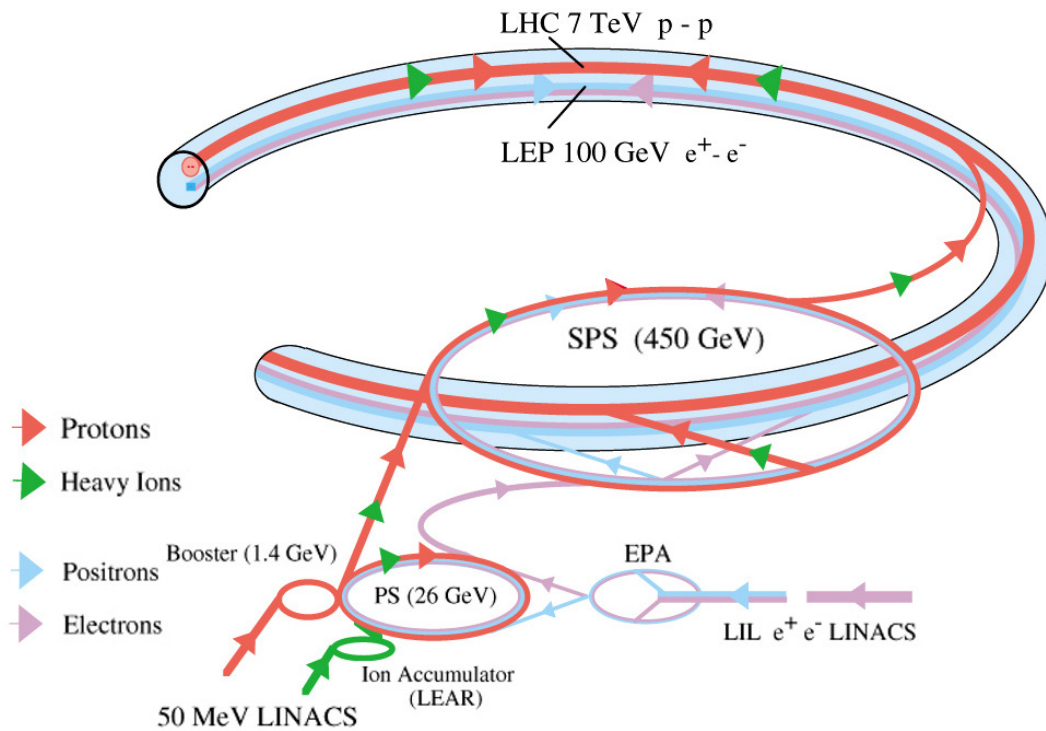
Figure 2.4: The LHC injection complex at CERN, taken from [Caron, 1993]. It is a succession of machines with increasingly higher energies. Each accelerator injects the particle beam into the next one, which takes over to bring the beam to an even higher energy. In the last element, the LHC, each particle beam is finally accelerated up to an energy of 6.5 TeV. Most of the injecting accelerators have their own experimental halls, where the beams can be used for experiments at lower energies, see figure 2.6.

a closed circular path, consisting of separated components for acceleration, beam focusing and bending. The particles get accelerated in a linear setup as described above driven by radio-frequency sources and focused by quadrupole magnets. Bending is also done by magnetic fields, whereby the magnetic induction is synchronized and proportional to the kinetic energy of the particles and increases during the acceleration process. The Lorentz-force that acts on a particle over the magnetic field has to compensate the centrifugal force due to the movement on the orbit. Neglecting the electric fields, the Lorentz force and the centrifugal force of the particle is [Holzer, 2017]

$$F_{\text{Lorentz}} = qvB, \tag{2.5}$$

$$F_{\text{centrifugal}} = \frac{\gamma mv^2}{r}, \tag{2.6}$$

with B as magnetic induction, $\gamma = 1/\sqrt{1 - v^2/c^2}$ as Lorentz factor with c as speed of light, and r as radius of the circular path. If we assume an idealized particle moving along the path, the two conditions will be equal for a perfect circular orbit. This yields the condition

$$\frac{mv}{q} = \frac{p}{e} = Br, \tag{2.7}$$

where we refer to protons and set accordingly $q = e$, as elementary charge, and with p as particle momentum. Br is the so called beam rigidity that is related to the particle momentum carried in the storage ring and directly defines the size of a circular accelerator. Instead of a simplified picture of a continuous dipole field, storage rings are build out of several dipoles closed to a loop. If ϕ is the bending angle, ρ the bending radius of a single magnet and l the particle path length, then [Holzer, 2017]

$$\phi = \frac{\mathrm{d}l}{\rho} = \frac{B\,\mathrm{d}l}{B\rho}. \tag{2.8}$$

The main dipole magnets of the ring have to determine a total bending angle of 2π. Therefore we require that

$$\frac{\int B\,\mathrm{d}l}{B\rho} = 2\pi. \tag{2.9}$$

In the example of the LHC, the dipole field has been designed to achieve the highest possible values. Using (2.7), (2.9) and the values given in table 2.2 with

the specifications of the LHC, we obtain a required magnetic induction of

$$B = \frac{2\pi p/e}{lc} = \frac{2\pi \cdot 6500 \cdot 10^9 \,\text{eV}}{1232 \cdot 15 \,\text{m} \cdot 2.99792 \cdot 10^8 \,\text{ms}^{-1}} = 7.37 \,\text{T}, \qquad (2.10)$$

to bend the beams. That can be realised by using superconducting NbTi filaments operated at $T = 1.9 \,\text{K}$.

The maximum energy of the particles is on the one hand side limited by the obtainable magnetic induction, the maximum curvature, and the size of the circular accelerator. On the other hand side another aspect plays also an important role, mostly important for electron accelerators, i.e. the loss of energy due to the emission of synchrotron radiation. If the electrons become more and more relativistic, $\beta = v/c \approx 1$ and are bent on a circular path, they radiate intense light, the so-called synchrotron radiation. The power loss due to this radiation is inversely proportional to the square of the bending radius and depends on the energy of the particle beam [Holzer, 2017]:

$$P_\text{s} = \frac{2}{3} \alpha \hbar c^2 \frac{\gamma^4}{\rho^2} = \frac{2}{3} \alpha \hbar \frac{E^4}{\rho^2 m^4 c^4}, \qquad (2.11)$$

where α denotes the fine structure constant and $\hbar$ the Planck constant. The particles lose energy with each turn they take. To compensate for these losses, RF-accelerator stations are installed in the straight sections of the ring. The power loss is proportional to the 4th power of the relativistic factor γ, i.e. of the inverse particle mass and sets severe limits on the beam energy in the ring. Electrons are a factor of ≈ 2000 lighter than protons, resulting in a power loss by synchrotron radiation $\approx 10^{13}$ times higher than for protons of the same energy in the same circular accelerator. To overcome this limitation even larger circular accelerators were built and more powerful magnets were installed to maintain the beam path for higher particle energies. A recent plan at CERN is to build a new particle accelerator, the "Future Circular Collider" (FCC), through three countries with a circumference of nearly $100 \,\text{km}$ [APS, 2017], see figure 2.5. For the maximum achievable electron energy of $E = 175 \,\text{GeV}$ the synchrotron radiation would cause an energy loss (2.11) of around $8.6 \,\text{GeV}$ per turn, resulting in an immense need of energy supply. For one thing, this machine would extend the current frontier in particle energies by more than one order of magnitude, but the costs and effort to build this accelerator will be enormous and the electron energies are still not reaching the $1 \,\text{TeV}$ mark.

All these listed limitations for current and future laser, linear and circular accelerators lead to the conclusion that a new type of accelerator is needed. The LHC is able to produce high energy, multi TeV protons, but not electrons. If it would be possible to transfer a fraction of the energy from the protons to the much lighter electrons, a new accelerator frontier would be opened. The goal can be achieved with plasma wakefield accelerators as described in the next section.
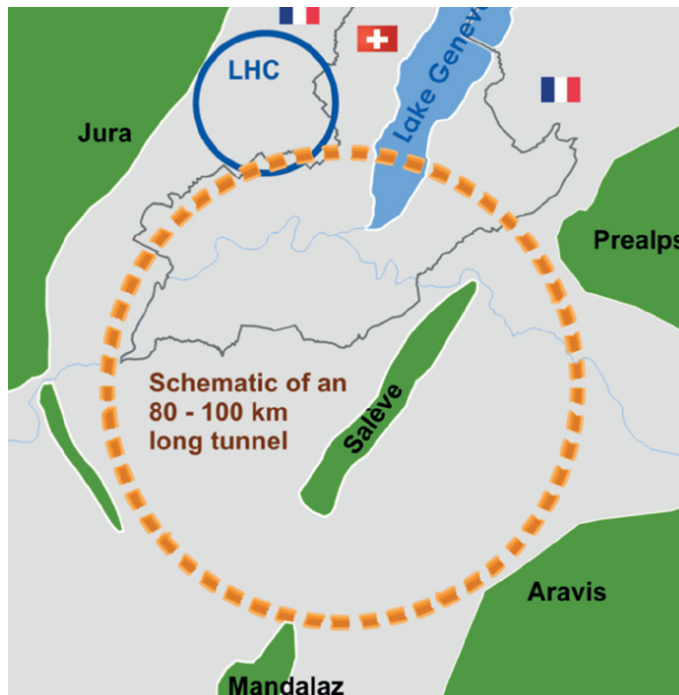

Figure 2.5: Plan of a next accelerator at CERN, the Future Circular Collider (FCC), taken from [APS, 2017]. It would be build through three countries with a circumference of nearly $100\,\mathrm{km}$. The maximum proposed electron energy is $E = 175\,\mathrm{GeV}$.

2.2 Particle-driven wakefield accelerators

Wakefield acceleration has already a long history of scientific development. The first steps towards a plasma wakefield accelerator were taken in the late 1940's by Fermi [1949] and Mc Millan [1950]. They considered cosmic-ray particle acceleration by moving magnetic fields or electromagnetic waves. Based on that, Chan [1971] introduced a possible energy booster for relativistic charged particles by ultraintense laser radiation. Only one year later Palmer [1972] discussed an electron accelerator with lasers directed through a helical magnetic field. Willis [1975] proposed the possibility to accelerate a dilute plasma with a high power laser and a relativistic electron beam. Based on that, plasma-assisted acceleration was recognized as a potential alternative to conventional RF-based acceleration [Tajima, 1979]. They investigated the drive of a plasma wakefield with an intense laser pulse. The electromagnetic radiation sets the electrons into a transverse oscillation producing a space charge in this region by the displacement between electrons and ions. If the light pulse has passed, the generated electric field pulls the electrons back and a plasma oscillation is created. The wake plasma oscillation can trap electrons which can gain a huge amount of energy when they are accelerated forward. Soon after the publication it was realized that charged particle bunches could also drive large amplitude wakefields and the scheme for a plasma wakefield accelerator (PWFA) was introduced [Chen et al., 1985]. In the scheme the plasma electrons are displaced by the electric field of the relativistic particle bunch and not of the laser. Up to now laser-driven wakefield accelerators reach higher maximum plasma densities and accelerating fields compared to particle-driven wakefield accelerators, but latter are a more promising concept towards even higher particle energies. Modern PWFAs are maximizing the accelerating field inside the plasma by increasing the number of particles per volume unit using a high power laser just to ionize the vapor in the plasma cell and a relativistic particle bunch to drive the wakefield (see section 2.2.2 for details).

2.2.1 Theory and concepts

As outlined in section 2.2, in the PWFA scheme the plasma electrons are displaced by the electric field of the relativistic particle bunch. If the particle bunch is negatively charged, plasma electrons are expelled from the volume of the particle

bunch. These electrons leave a net positive charge behind the bunch head, are attracted back, overshoot and sustain plasma oscillations [Caldwell et al., 2016]. The local plasma density n_0 defines the angular frequency of the plasma wave in this region by [Caldwell et al., 2016]

$$\omega_{\rm p} = \sqrt{\frac{n_0 e^2}{\epsilon_0 m_{\rm e}}}, \tag{2.12}$$

where $m_{\rm e}$ is the electron mass. The plasma ions are much heavier than the electrons and can be considered as immobile [Caldwell et al., 2016]. The plasma wake is directly coupled to the drive bunch. Hence, the phase velocity $v_{\rm ph}$ of the wake is close to that of the drive bunch $v_{\rm b}$ which is close to the speed of light c. Therefore its wavelength is

$$\lambda_{\rm p} = \frac{2\pi c}{\omega_{\rm p}}. \tag{2.13}$$

Consequently, the plasma wave is effectively driven by a particle bunch with the length on the order of the wave period [Lu et al., 2005]

$$\sigma_{\rm zb} = \frac{\lambda_{\rm p}}{\sqrt{2\pi}}. \tag{2.14}$$

The maximum longitudinal electric field amplitude, defined by the wave breaking field [Akhiezer, 1956]

$$E_0 = \frac{m_{\rm e}\omega_{\rm p}}{e}c \tag{2.15}$$

is nearly reached for high density plasma wakes. The excited plasma wakefields have an accelerating (decelerating) longitudinal component and a focusing (defocusing) transverse component with comparable amplitudes [Caldwell et al., 2016]. In the plasma wakefield these fields switch periodically and lead to an accumulation of accelerated electrons behind the bunch. Consequently, a plasma wake with high accelerating fields is driven by the movement of an relativistic drive bunch of charged particles through a plasma [Joshi, 2003][Bingham et al., 2004] [Caldwell et al., 2009]. If an additional trailing bunch of relativistic electrons with sufficient charge follows the drive bunch in the wake at an appropriate distance, these electrons are efficiently accelerated to high kinetic energies.

First experimental results were published by Rosenzweig [1988], demonstrating the drive of a plasma wakefield by a relativistic electron bunch and the acceleration of a witness bunch. Previous experiments have shown that, using a single 42 GeV electron drive bunch, plasma electrons are accelerated up to a maximum

energy of 85 GeV in less than a meter of plasma [Blumenfeld et al., 2007]. But the total charge of accelerated electrons was insufficient to be extracted from the plasma. To reach higher resulting energies in such wakefield accelerators, a staging of many plasma sections would be required. In 2009 an alternative proposal was made [Caldwell et al., 2009][Lotov, 2010]. They developed the concept of a proton-driven plasma wakefield accelerator by proof-of-principle simulations. In that type of PWFA a high energy transfer efficiency became possible between the driver and the witness bunch for proton energies above 1 TeV. The PWFA by Litos [2014] produced highly accelerated electrons of a trailing bunch that contains a sufficient charge to extract a significant amount of energy from the plasma wakefield accelerator, but with a lower accelerating field. Over a length of 36 cm the core electrons gain about 1.6 GeV of energy per particle. Thus, additional steps and investigations have to be done to irretrievably implement proton driven PWFAs as a new research tool. One next step is the AWAKE project at CERN [Gschwendtner et al., 2016][Assmann et al., 2014][Caldwell et al., 2016].

2.2.2 The AWAKE project

The Advanced Proton Driven Plasma Wakefield Acceleration Experiment (AWAKE) is an electron accelerator project to study proton driven wakefield generation based at CERN. It is a proof-of-principle experiment demonstrating that relativistic proton bunches of energies around $E_\mathrm{p} = 400$ GeV can drive wake fields in a plasma to accelerate electrons to the TeV regime [Turner et al., 2016]. But to achieve such high accelerating fields of GV/m in a plasma, high particle densities are needed and the driver must be shorter than the plasma wavelength [Pukhov et al., 2012]. The wave breaking limiting field of a plasma (2.15) is also given by [Assmann et al., 2014]

$$E \approx \sqrt{\frac{n_\mathrm{e}}{10^{20}\,\mathrm{m}^{-3}}} \tag{2.16}$$

with E as accelerating electric field and n_e as plasma density. Due to the fact that we are looking for a high gradient acceleration, the plasma density has to be higher than $10^{20}\,\mathrm{m}^{-3}$.

The corresponding plasma wavelength (2.13) [Assmann et al., 2014]

$$\lambda_{\mathrm{p}} \approx \sqrt{\frac{10^{21}\,\mathrm{m}^{-3}}{n_{\mathrm{e}}}}\,\mathrm{mm}, \tag{2.17}$$

is then in the range of a mm and thus much shorter than the available driving proton bunches in a cm scale. To meet these restrictions one takes advantage of a physical mechanism, the self-modulation instability (SMI) in this kind of environment [Kumar et al., 2010]. In the AWAKE experiment a proton beam, which contains around $3 \cdot 10^{11}$ particles, are extracted from the CERN Super Proton Synchrotron (SPS), see figure 2.6 and coupled into the plasma chamber [Pukhov et al., 2012, Gschwendtner et al., 2016]. The proton beam has a bunch length of 12 cm (see table 2.3). The bunch length is rather large compared to the wavelength of the wakefield ($\lambda_{pl} \approx 1\,\mathrm{mm}$), and the experiment relies on the SMI, which modulates the proton driver at the plasma wavelength into smaller groups in a first seperate several meters long plasma chamber [Gschwendtner et al., 2016].
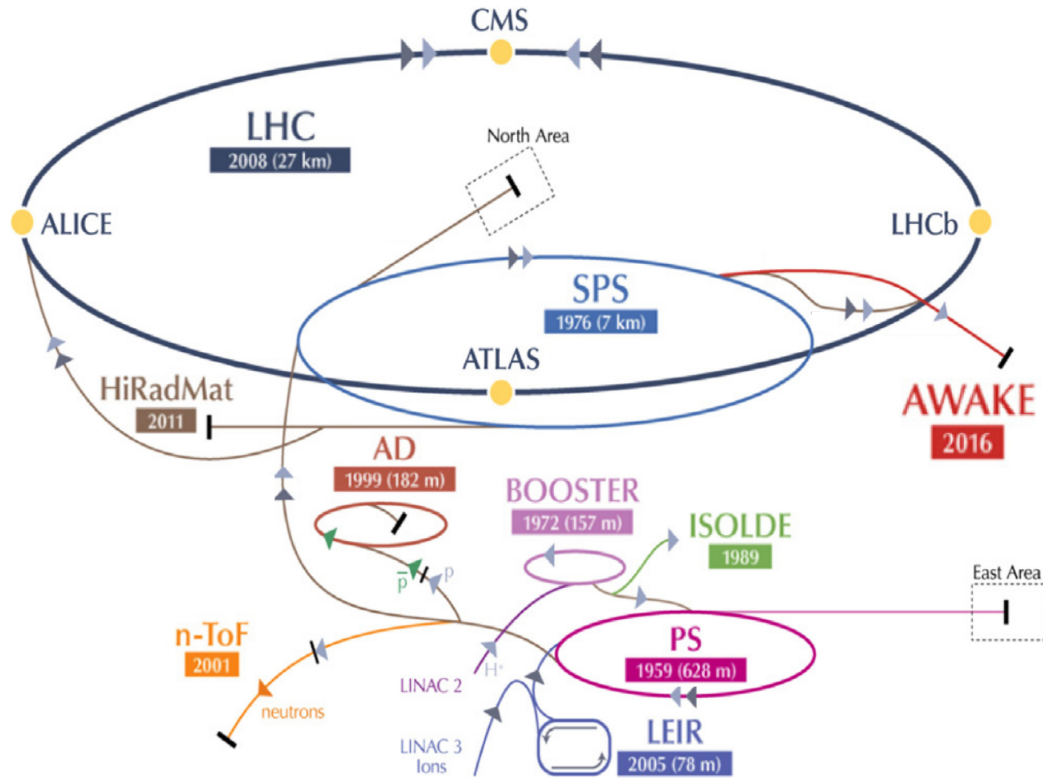

Figure 2.6: The CERN accelerator complex with the Super Proton Synchrotron (SPS) in light blue and the AWAKE experiment location in red. Other accelerator rings and experiments are also depicted with their respective year of construction. Figure taken from [Gschwendtner et al., 2016].

The SMI selectively focuses or defocuses different parts of the beam, caused by an amplification of the rippling of the proton beam resulting in a plasma wave train. When leaving the chamber, the previously large proton bunch is split into hundrets of micro-bunches seperated by exactly one plasma wavelength to drive the high amplitude wake. This process is very energy inefficient but cost-effective and easy to handle. Hence, it is a very well suited solution for many PWFAs. A main restriction for the SMI is that these micro-bunches have to interact constructively, meaning that the plasma in which the SMI happens has to be highly uniform [Lotov et al., 2013c][Lotov et al., 2013a]. The error of the relative plasma density has to be in the range of [Assmann et al., 2014]

$$\frac{\delta n_{\mathrm{e}}}{n_{\mathrm{e}}} \approx \frac{\lambda_{\mathrm{p}}}{2\pi\sigma_{\mathrm{zb}}}. \tag{2.18}$$

With this boundary conditions for the SMI, the variation of the plasma density has to be below $0.5\,\%$ over a distance of several meters [Öz, 2014]. Different studies have shown that the SMI is less sensitive to plasma density inhomogeneity than the accelerated particles. If the plasma density fluctuates, the drive bunch freely passes through regions of increased plasma density and interacts with regions of reduced plasma density, which corresponds to the spacing of the micro-bunches [Lotov et al., 2013c][Lotov et al., 2013b]. Up to now, the best way up to now to achieve the required axial homogeneity is to use an alkali metal vapor filled chamber and to ionize the neutral gas with a high power laser pulse which is shorter than λ_{pl} [Turner et al., 2016]. The reasons to use alkali vapor the low ionization potential in the range of a few eV and the large ion masses, which makes them less sensitive to electroc field forces [Vieira et al., 2012b][Vieira et al., 2012a]. If additionally the laser propagates parallel to the motion of the proton beam, the fast creation of plasma inside the bunch seeds the SMI [Assmann et al., 2014].

After the first chamber the self-modulated proton bunch enters a second plasma cell where it drives the plasma wakefield. One major reason to split the PWFA into two parts, besides the plasma uniformity challenge for the SMI, is the avoidance of the phase velocity problem if the witness bunch would be coexisting with the SMI and consequently to growing wakefields. Over the first meters in the first plasma cell the SMI grows. In this region the effective wakefield phase velocity is slower than the drive bunch phase velocity [Lotov, 2015][Schroeder et al., 2011]. The slow wave is as problematic for accelerated particles as the plasma uniformity, i.e., the defocusing phase of the wave scatters the particles. For protons

parameter	value
proton beam	
beam momentum	$400\,\mathrm{GeV/c}$
number of protons per bunch	$3 \cdot 10^{11}$
bunch length (σ)	$0.4\,\mathrm{ns}\,|\,12\,\mathrm{cm}$
bunch size at entrance ($\sigma_{x,y}$)	$200\,\mathrm{\mu m}$
laser beam	
laser type	fibre titanium:sapphire
wavelength	$780\,\mathrm{nm}$
pulse length	$100 - 120\,\mathrm{fs}$
laser power	$4.5\,\mathrm{TW}$
focussed laser size ($\sigma_{x,y}$)	$1\,\mathrm{mm}$
repetition rate	$10\,\mathrm{Hz}$
plasma source	
plasma type	laser ionized rubudium vapor
plasma density	$7 \cdot 10^{20}\mathrm{m}^{-3}$
length of plasma chamber	$10\,\mathrm{m}$
plasma radius	$> 1\,\mathrm{mm}$
skin depth	$0.2\,\mathrm{mm}$
electron beam	
beam energy	$16\,\mathrm{MeV}$
energy spread	$0.5\,\%$
bunch length (σ)	$0.5\,\mathrm{ps}$
bunch size at focus ($\sigma_{x,y}$)	$250\,\mathrm{\mu m}$
charge per bunch	$0.2\,\mathrm{nC}$

Table 2.3: Specifications of the AWAKE accelerator setup, taken from [Gschwendtner et al., 2016].

this is not a severe problem due to the fact that the growth of the SMI relies also on the defocusing feature. To prevent the phase velocity problem for electrons, an additional accelerated electron beam with energies of $E_e = 16\,\mathrm{MeV}$ is injected and merged to the proton beam line of the second cell for acceleration purposes at the stage of fully developed SMI [Pukhov et al., 2011]. The electron beam is produced via laser induced photo-emission from a cathode and is additionally boosted. In the second cell, a more than $10\,\mathrm{m}$ long and homogeneous, high-density plasma discharge is required to create high electric fields of $\mathrm{GV/m}$ in which the electrons are accelerated. To create the high electric fields, a plasma discharge with plasma density of $n_e = 7 \cdot 10^{20}\,\mathrm{m}^{-3}$ has to be provided with a variation in plasma density of under one percent [Caldwell et al., 2009]. Axial plasma density changes would lead to varying frequencies of the plasma oscillations and cause phase differences between the driving proton bunch and the plasma wave, and also between the accelerated particles and the wakefields. If the plasma density increases, the plasma wavelength shortens and the electrons will be scattered transversely by the defocusing phase of the wave. On the contrary, if the plasma density decreases the plasma wavelength gets longer and the electrons will be decelerated by the phase difference [Caldwell et al., 2016].

These two possibilities are leading to a deceleration and broadening of the electron bunch. The high and homogeneous plasma density has to be maintained for a few microseconds. In this time window the relativistic protons are moving through the several meters long plasma discharge and accelerate the injected electrons. Another requirement is that the peak plasma density has to be achieved in the center of the discharge where the proton bunch is moving through. This area has to be, depending on the proton source, a few mm wide. One possibility to achieve such a high plasma density with the given constraints is the use of an alkali metal vapor filled plasma chamber, ionized with lasers, as done in the first plasma chamber. Plasma densities in the order of $n_e \approx 10^{22}\,\mathrm{m}^{-3}$ can easily be reached in the center of the cell. But the possible use of the option is uncertain, due to the limited available laser power and the difficult up-scaling to a length of $l = 100\,\mathrm{m}$ or even $l = 10\,\mathrm{m}$ for the AWAKE experiment [Assmann et al., 2014]. Figure 2.7 shows the experimental setup. A possible solution for such a long plasma discharge would be a helicon plasma discharge [Buttenschön et al., 2013][Buttenschön et al., 2014] as described in section 3.3. The next chapters address the question if the requirements in specific plasma parameters required to realize the particle accelerators within the AWAKE project
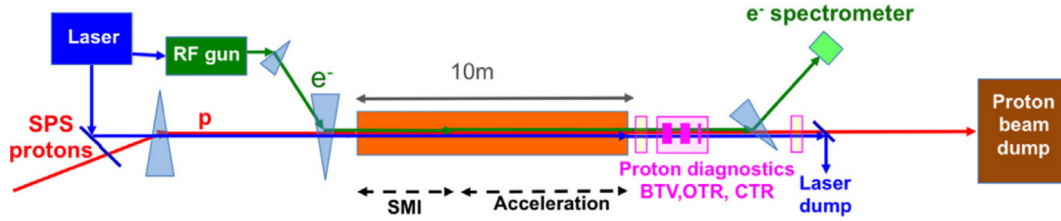
Figure 2.7: Baseline design of the AWAKE experiment, taken from [Gschwendtner et al., 2016].

are achievable. The experimental setup of the helicon plasma cell PROMETHEUS-A, the laser-diagnostics and the numerical methods are described in chapter 5. In chapter 6 the experimental results are shown and design relevant questions are answered, e.g., if the goal plasma density, measured with a laser interferometer, can be achieved and how large the width of the peak plasma density is. A brief summary on this subject was recently published [Buttenschön et al., 2018]. Other important aspects as the centrally peaked plasma profile and the similarity and reproducability of the plasma density evolution over the whole plasma profile are discussed. It is investigated how the change of experimental parameters influences the plasma density and some limitations are shown. To characterize the plasma, the electron temperature is calculated and compared to the plasma density evolution with the help of a rate reaction model, described in chapter 4. This all is done for different experimental parameters. To describe the neutral gas and single ionized atom evolution, laser induced fluorescence measurements are shown. These results of metastable atoms and of the rate reaction model are taken into account to scale down to the groundstates of argon and the relation to the plasma density and temperature is discussed.

Chapter 3

Radio-frequency discharges

Radio-frequency (RF) discharges are driven by alternating, time-dependent current and voltage sources. They are working in a low pressure neutral gas regime. The angular driver frequency ω_{RF} is in a range where the ions are not able to follow the alternating electric field, i.e.

$$\omega_{\mathrm{pi}} < \omega_{\mathrm{RF}} < \omega_{\mathrm{pe}}, \tag{3.1}$$

where ω_{pi} and ω_{pe} are the ion or electron angular plasma frequency, respectively. A typical RF-frequency is $f_{\mathrm{RF}} = 13.56\,\mathrm{MHz}$ with its first harmonic $f_{\mathrm{RF}}^{(2)} = 27.12\,\mathrm{MHz}$. As described in section 5.1.1 the heating source of the experimental discharge are three helical antennas. The mechanism that couples the heating power into the plasma depends on the input power level. Three different modes of discharges are distinguished with increasing heating power: the capacitive, the inductive, and the helicon discharge. The capacitive and the inductive plasma discharges are widely used in industry, are well known and already deeply investigated [Conrads and Schmidt, 2000][Braithwaite, 2000]. The helicon discharge mechanism is mostly used in research and is still under investigation since several physical processes are not yet well characterized and are under intensive discussion [Chen, 2015]. This chapter gives a short overview of capacitively and inductively coupled discharges and discribes the helicon discharge mechanism [Lichtenberg, 2005] in more detail, mainly because the discharge mode is used in the present thesis work.

3.1 Capacitively coupled discharge

The basic experimental setup scheme of a capacitively coupled plasma discharge consists of two parallel mounted metal plates. Between these plates a RF-signal is applied. In front of the plates a sheath is formed. Over the period of the RF-signal the thickness of the sheath varies and induces an oscillation in the plasma potential at the frequency of the applied signal. In the sheath high electric fields develop and accelerate the existing ions in the plasma. At moderate to high neutral gas pressures, the power coupling is determined by inelastic collisions of electrons with the neutral background gas. Due to the acceleration of ions at the plasma edge (resulting in ion-wall collisions) high energy losses are generated and rather low plasma densities of $n_e \leq 1 \cdot 10^{17}\,\mathrm{m}^{-3}$ are achievable [Lichtenberg, 2005]. Because of the accelerating fields and the dynamics in the sheath in front of the plates, the capacitive discharge mode is used in many surface processing devices [Wegner, 2010].

3.2 Inductively coupled discharge

The simplest experimental setup for an inductively coupled plasma discharge consists of a current-carrying coil wound round a cylindrical dielectric vacuum chamber. The oscillating electric fields have two effects: (1) At both ends of the coil a voltage drop exists leading to an alternating electric field, as in the case of the capacitively coupled plasma discharge. (2) The other heating mechanism is based on an additional electric field induced into the plasma by the alternating magnetic field of the antenna. The resulting electron current heats and ionizes the plasma via collisions. The most efficient inductively coupled discharges requires that the induced electron currents distribute over the whole plasma volume. This is the case if the penetration depth of the alternating magnetic field, defined by the skin depth $\delta = c/\omega_p$, is equal to the plasma radius [Lichtenberg, 2005]. The drop of the voltage at the sheath is essentially lower than in the case of the capacitive discharges. Therefore higher plasma densities of typically up to $n_e \leq 1 \cdot 10^{18}\,\mathrm{m}^{-3}$ are achieved.

3.3 Helicon discharge

A helicon discharge is an efficient plasma production mechanism, creating plasmas of high density and low temperatures. They produce routinely plasma densities around $n_e \approx 10^{19}\,\mathrm{m^{-3}}$ at moderate RF-heating powers. Another advantage is that a helicon discharge deposits the main heating power in the center of the discharge, different from capacitive or inductive plasma discharges. In contrast to an electron-cyclotron-resonance heated (ECRH) plasma, a helicon wave heated plasma is a non-resonant heating mechanism. This specific type of heating is effective in plasmas with a high collisionality, leading to a high ionization rate and low electron temperatures in a non-LTE plasma, with

$$T_e \gg T_i \geq T_g, \tag{3.2}$$

with T_e as electron temperature, T_i as ion temperature and T_g as neutral gas temperature. Helicon waves are the bounded version of whistler waves, that are right-handed circular polarized electro-magnetic waves. The dispersion relation of a helicon wave is [Chen, 1984]

$$\frac{c^2 k^2}{\omega_{RF}^2} = 1 - \frac{\omega_p^2/\omega_{RF}^2}{1 - (\omega_c/\omega_{RF})}, \tag{3.3}$$

with k as wave number and ω_c as cut-off frequency. If a long wavelength whistler wave propagates in a cylindrical chamber, eigenmode structures are formed with different dissipation and polarization characteristics. The eigenmodes are characterized by a mode number m that is also retrieved in the design of the antenna [Light, 1995]. The helicon dispersion relation can than be simplified to [Chen, 1997]

$$\omega_{RF} = k\frac{\beta B}{\mu_0 n_e e}, \quad \text{where} \quad \beta = \frac{k_\omega^2}{k} \tag{3.4}$$

with μ_0 as vacuum permeability and k_ω as the wave number of low-frequency whistler waves for which $k^2 = k_\perp^2 + k_\parallel^2$ applies. The parallel wave number $k_\parallel$ is basically given by the geometry of the antenna, whereas the perpendicular wave number $k_\perp$ depends on the radial expansion of the plasma [Franck, 2003]. This is especially well-founded for low-density plasmas. As seen in (3.4), the plasma density scales linearly with the magnetic induction in the helicon dispersion relation; theoretically there is no plasma density cut-off. But the dispersion relation

(3.4) is only valid in the limit

$$\omega_{ci} < \omega_{RF} < \omega_{ce}, \tag{3.5}$$

with ω_{ci} as ion cyclotron frequency and ω_{ce} as electron cyclotron frequency. At magnetic induction and plasma frequency combinations where the RF-frequency is close to the lower hybrid frequency, the linear scaling of (3.4) stops and the plasma density even decreases. The lower hybrid frequency is an oscillation of ions and electrons in a magnetized plasma with a hybrid frequency of ion, electron cyclotron and plasma frequency and is written as

$$\omega_{LH} = \sqrt{\frac{\omega_{ce}\omega_{ci}\omega_p^2}{\omega_{ce}\omega_{ci} + \omega_p^2}} = \sqrt{\frac{B^2 e^2 Z}{m_e(B^2 e_0 Z + n_e m_i)}}. \tag{3.6}$$

The lower hybrid frequency is dependent on plasma density and the magnetic induction. Experimental results have shown that the plasma density and the collisionality of the plasma particles are maximized close to the lower hybrid frequency (figures 3.1 and 3.2), what is discussed as a major reason for the efficient ionization of the plasma [Kwak et al., 2000],[Buttenschön et al., 2018]. The specific mechanism of power absorption in helicon discharges is still under debate. The collision frequency of coulomb collisions in this regime is too low and no dominating factor in power absorption. There are three different approaches to explain the plasma-power coupling:

1. One ansatz takes the electron population into account. The thermal velocity of the electrons has to be comparable to the phase velocity of the helicon wave and the energy of the wave is collisionlessly dissipated by Landau-damping [Molvik et al., 1997].

2. It is supposed that a second wave-type exists, the Trivelpiece-Gould mode, which is driven by the helicon wave. The energy of a Trivelpiece-Gould wave is efficiently dissipated by the plasma via collisions [Shamrai, 1996].

3. The third approach proceeds on the assumption that some resonance close to the lower hybrid frequency leads to an efficient absorption [Boswell, 1984].

The RF heating power is coupled into the plasma via external helical antennas. This principle brings another benefit into play. One can distribute the total power
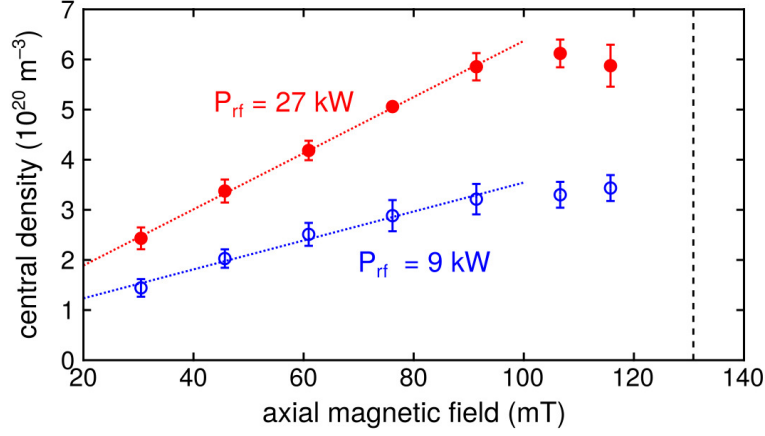
Figure 3.1: Scaling of the central plasma density with magnetic field induction for two different RF power levels. The black dotted line indicates the magnetic induction $B = 130.8\,\mathrm{mT}$ at which the lower hybrid frequency matches the RF frequency of $13.56\,\mathrm{MHz}$ at an plasma density $n_\mathrm{e} \leq 6 \cdot 10^{20}\,\mathrm{m}^{-3}$. Data are taken at $p_0 = 5\,\mathrm{Pa}$ and $B = 116\,\mathrm{mT}$, taken from [Buttenschön et al., 2018].
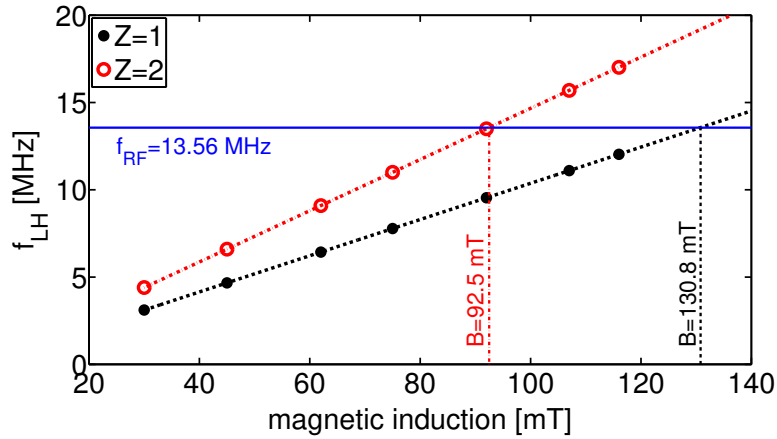

Figure 3.2: Scaling of the lower hybrid frequency with magnetic field induction (3.6) for two different ionization levels. Data points for plasma density and magnetic induction taken from figure 3.1 (high power case). The blue horizontal line indicates the RF driving frequency of $13.56\,\mathrm{MHz}$ and the vertical lines the matching magnetic inductions for different ionization level where $f_\mathrm{LH} = f_\mathrm{RF}$.
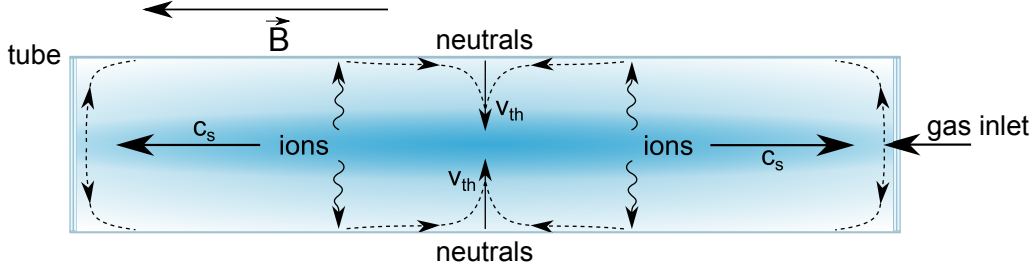
Figure 3.3: Scheme of neutral pumping. Axially outwards the ions are moving with c_s. Argon ions are also moving radially outward and recombinate at the outer wall to neutral argon. These neutrals are moving with thermal velocity inwards. Comparing both quantities an imbalance gets visible and a depletion of neutrals in the center of the discharge.

over a number of individual antennas and couple it to a set of RF sources. That makes it possible to scale a helicon wave heated discharge to an arbitrary length. The plasma density limit is commonly ascribed to neutral pumping, the depletion of neutral gas density in the center of the discharge. To keep the pressure balance and to ensure that the ionization process is not decelerating, the flux of argon neutrals and argon ions have to be equal, see figure 3.3. Axially the ions are moving with the sound speed c_s. A fraction of argon ions is also moving radially outward and recombinates at the outer wall to neutral argon. The neutrals at the wall are moving with thermal velocity v_th inwards. If we compare both quantities we see that

$$c_\mathrm{s} = \sqrt{\frac{\gamma Z k_\mathrm{B} T_\mathrm{e}}{m_\mathrm{i}}} \approx 2500\,\mathrm{m/s} \gg v_\mathrm{th} = \sqrt{\frac{k_\mathrm{B} T_\mathrm{g}}{m_\mathrm{g}}} \approx 300\,\mathrm{m/s}, \qquad (3.7)$$

where Z is the atomic number, k_B the Boltzmann constant, m_i the ion mass and m_g the mass of a neutral gas particle. The ionization mean-free path at these high plasma densities is

$$\lambda = \frac{1}{\sqrt{2} n_\mathrm{e} \sigma} = \frac{1}{\sqrt{2} \cdot 1 \cdot 10^{15}\,\mathrm{cm^{-3}} \cdot 7 \cdot 10^{-16}\,\mathrm{cm^2}} \approx 0.4\,\mathrm{cm}, \qquad (3.8)$$

with σ being the cross section for ionization by electron collisions (see chapter 4). This results in an average ionization of neutrals before they even reach the center of the discharge, leading to an imbalance of fluxes and depletion of neutrals in the center of the discharge, limiting the maximum plasma density. For this type of discharge, power balance calculations have shown that high plasma densities are achievable with relatively low RF power at low electron temperatures (figure 3.4) [Wegner, 2010][Buttenschön et al., 2018]. These power balance calculations

are an estimation of the required power to maintain a plasma discharge of a given plasma density considering a constant neutral gas density of the discharge and general power sources and losses, like ionization, excitation, recombination, coulomb collisions between ions and electrons and particle losses to the wall.
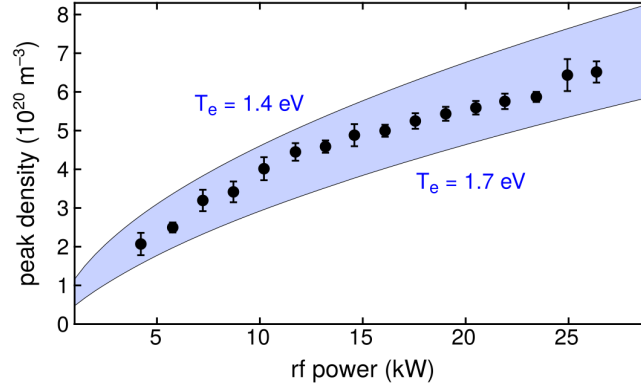

Figure 3.4: Scaling of the central plasma density with total RF power. The shaded area indicates the plasma density region the power balance predicts for an filling gas pressure of $p_0 = 5\,\mathrm{Pa}$ and a flat-top plasma density profile with $10\,\mathrm{mm}$ radius within the boundary of the electron temperature values shown, taken from [Buttenschön et al., 2018].

Chapter 4

Modeling of high-density argon discharges

4.1   Reaction rate model

This chapter introduces into a zero dimensional reaction rate model (0DRRM). The model allows one to study the main generation reactions of ions and metastable states in a low-pressure, high-density argon plasma, which is quantitatively related to the experimental results obtained with laser-induced fluorescence (LIF) measurements in the PROMETHEUS-A helicon device, c.f. chapter 5. The input parameters for the model are chosen to match the experimental conditions with a neutral gas pressure of $p_0 = 2 - 8\,\mathrm{Pa}$ and RF powers of $P_{\mathrm{RF}} = 0.3 - 27\,\mathrm{kW}$ in total coupled via three helical antennas. The plasma reactions are described by a set of first-order differential equations, that are solved self-consistently to yield the densities of the respective species. To verify experimental results, many different theoretical models were developed over the last decades. They often vary by several orders of magnitude due to the use of more or less exact rate coefficients [Schmidt et al., 2015]. Although nowadays more quantitative information on rate coefficients is available, in many cases one has to rely heavily on approximate methods. The semi-empirical formula of Lotz [1968], which uses a classical scaling law, is still widely used [Baeva et al., 2012] [Peerenboom et al., 2010] [Heiermann, 2002]. Another often used formula to take excited states into account is given by Hoffert et al. [1967]. They promote an analytical formulation

for forward ionization and recombination of argon. Electron impact ionization occurs when the energy of the electron exceeds the ionization threshold energy of the atom, which is $E_{iz} = 15.76\,\text{eV}$ for argon. Another possibility to ionize an atom is to generate an excited state first and ionize it afterwards. In the excited state, the required energy for ionization is lowered due to the higher energetic state of the atom. Argon has up to 75 excited states [Vlcek, 1986]. Most of these states decay to the ground state via spontaneous radiative transitions and have a short life time. Some of them are populated long enough to be ionized by electron collisions. This leads to a process of ionization by excitation and a subsequent ionization of the excited atom. The process of stepwise ionization is not negligible for electron temperatures $T_e > 1\,\text{eV}$ [Fridman, 2011] and is implemented in the respective reaction rate model.

There are three kinds of collisions between electrons and neutrals:

1. elastic collisions, with an exchange of momentum but the total kinetic energy of the colliding particles remains constant,

2. inelastic collisions, in which part of the kinetic energy of one particle is converted into internal energy of the other particle (most common in rare gas plasmas is excitation and ionization),

3. superelastic collisions, in which internal energy of one particle is changing the kinetic energy of the other particle [Raju, 2004]

For ionization by electron collisions, which is considered in the model, only the inelastic collisions are taken into account.

In the development of a reaction rate model, specifically designed for the comparison with our experimental measurements, different models have been investigated and evaluated. One of the oldest models for the calculation of ionization cross sections is the model of Thomson [1912]. It is based on the principles of electrodynamics and does not correctly reflect the processes of impact ionization. Nonetheless the model forms the basis for various advanced models, such as the ones from Drawin [1961] or Vriens [1973]. One of the successors of Thomson's model is the model of Drawin [1961][1963]. It contains an empirical correction of Thomson's formula for the calculation of collision cross-sections. This model shows good agreement with experimental results from Smith [1930] and Asundi [1963b]. Although Drawin has not calculated any rate coefficients in his work, the cross

sections have been used by other authors, e.g. Annaloro et al. [2012]. The model of Hoffert [1967] is an advanced model which aims at developing a simple but realistic representation of coupled atomic processes in argon, in particular atom-atom and atom-electron impacts s well as three-body recombination. It consists of a set of equations governing a quasi one-dimensional flow of an argon plasma and was confirmed by Maxwell [1974] for a temperature range of $0.25\,\mathrm{eV} < T_\mathrm{e} < 2\,\mathrm{eV}$ in an expansion experiment of partially ionized argon. Another model developed in the 1960's is the semi-empirical model of Lotz [1967b][1968]. Almost all experimental results can be approximated with the formulas given in that model, but multiple ionization that lowers the ionization potential and the collision limit is not taken into account. Another step was taken by Lennon et al. [1988b] by calculating Maxwellian rate coefficients over a wide temperature range through an evaluation of cross sections for each species based on the classical scaling laws. A model for treating multistep ionization and recombination was developed by Simpson [1990]. The formulae are based on experimental data and theoretical calculations, where he uses data of Wetzel et al. [1987] to describe ionization from the ground state, data from Bretagne et al. [1986] and Tachibana [1986b] for the excitation of atoms and data of Vriens [1973] to calculate the ionization of excited states. This model is very useful for plasmas in which radiation effects are negligible. One of the currently developed models is from Annaloro et al. [2012], in which global rate coefficients for ionization and recombination over a wide electron temperature range of $0.25\,\mathrm{eV} < T_\mathrm{e} < 2\,\mathrm{eV}$ are obtained. A zero-dimensional (time-dependent) code is used to investigate the behavior of excited states, which are considered as independent species. As described in the next sections, formulae, cross-section and rate coefficient data were taken from several of these models to formulate a specific reaction rate model.

4.1.1 Principle and energy levels

The 0DRRM provides calculations of fundamental plasma properties like plasma density and temperature. Since there are no plasma profile effects directly taken into account, the model gives no information about the spatial distribution of the respective plasma species. Furthermore the model assumes a Maxwellian electron energy distribution function (MEEDF [1990b]), justified by the high collisionality in the low electron temperature and high plasma density argon discharges of PROMETHEUS-A ($T_e = 1 - 2 \, \text{eV}$ and $n_e \leq 7 \cdot 10^{20} \, \text{m}^{-3}$). The energy distribution of electrons has a strong influence, due to the fact that collisional ionization has a certain threshold energy in the order of some electron volts.

The argon plasma discharge contains a number of species created by different reactions, which are all described by specific rate coefficients. The reaction rate model contains in total 14 energy levels and between them several reaction channels. In the pressure regime under consideration three-body collisions are of little importance, but they are included in the model to cover the full set of reaction channels. Reactions requiring high energetic electrons or ions with energies of $E > 50 \, \text{eV}$ are neglected and the changing coupling efficiency between RF power and plasma is not integrated in the calculations. In 0DRRM only inelastic reactions are taken into account. Included are: the argon ground state, single and double ionized states, the six metastable states (for laser-induced fluorescence measurements of neutrals and ions), dimer and trimer states that depend on the single ionized and the neutral metastable states.

For an overview, all considered atomic argon states and transitions are marked by arrows in figure 4.1. The specific atomic reaction equations are given in table 4.2. The reaction rate model yields all plasma quantities that are shown in table 4.1. All tabulated quantities are a function of gas pressure and electron temperature. Before starting a calculation run, the initial neutral argon ground state density n_{Ar} is calculated from the experimental neutral (ideal) gas pressure.

$$n_{\text{Ar}} = \frac{p_{\text{Ar}}}{k_B T_g}. \tag{4.1}$$

The global density evolution is balanced by sources and sinks. The estimation of the plasma parameters within the plasma volume is provided by the particle balance equation:

$$\frac{\mathrm{d}n_x}{\mathrm{d}t} V = G_{\text{source}} V - G_{\text{loss}} V - \Gamma_x S, \tag{4.2}$$

34

Figure 4.1: The reaction rate model contains 14 energy levels in total and several reaction channels between. Included are the argon ground state, single and double ionized state, the six metastable states for the neutral and ion laser-induced fluorescence measurements and dimer and trimer states. The additional reaction product, representing the special reaction type, is marked on the respective arrow. All reactions concerning dimers and trimers are not marked for clarity. For the specific reaction equations see table 4.2.

atomic state density	label	description
	n_{e}	electrons
	n_{Ar}	neutral argon ground state
$n_{\mathrm{Ar}(^2\mathrm{P}^0_{3/2}4\mathrm{s})}$	$n_{\mathrm{Ar^i}}$	initial neutral argon metastable state
$n_{\mathrm{Ar}(^2\mathrm{P}^0_{1/2}4\mathrm{p})}$	$n_{\mathrm{Ar^e}}$	excited neutral argon metastable state
$n_{\mathrm{Ar}(^2\mathrm{P}^0_{1/2}4\mathrm{s})}$	$n_{\mathrm{Ar^f}}$	final neutral argon metastable state
$n_{\mathrm{Ar_2}(^2\mathrm{P}^0_{3/2}4\mathrm{s})}$	$n_{\mathrm{Ar_2^i}}$	initial neutral argon dimer
$n_{\mathrm{Ar_2}(^2\mathrm{P}^0_{1/2}4\mathrm{p})}$	$n_{\mathrm{Ar_2^e}}$	excited neutral argon dimer
$n_{\mathrm{Ar_2}(^2\mathrm{P}^0_{1/2}4\mathrm{s})}$	$n_{\mathrm{Ar_2^f}}$	final neutral argon dimer
	$n_{\mathrm{Ar^+}}$	single ionized argon ground state
$n_{\mathrm{Ar^+}(^4\mathrm{F}_{7/2}3\mathrm{d})}$	$n_{\mathrm{Ar^{i+}}}$	initial single ionized argon metastable state
$n_{\mathrm{Ar^+}(^4\mathrm{D}^0_{5/2}4\mathrm{p})}$	$n_{\mathrm{Ar^{e+}}}$	excited single ionized argon metastable state
$n_{\mathrm{Ar^+}(^4\mathrm{P}_{3/2}4\mathrm{s})}$	$n_{\mathrm{Ar^{f+}}}$	final single ionized argon metastable state
	$n_{\mathrm{Ar^+_2}}$	single ionized argon dimer
	$n_{\mathrm{Ar^+_3}}$	single ionized argon trimer
	$n_{\mathrm{Ar^{2+}}}$	double ionized argon ground state

Table 4.1: Yielded plasma quantities in the reaction rate model.

where the parameter V is the volume of the plasma vessel, S the surface area of the plasma, Γ_x the average particle flux normal to the surface and G_{source} and G_{loss} the source and loss terms. They are determined by the product of the reaction rate coefficients k_{xy} and the respective densities n_x and n_y of the plasma species involved in a reaction with two reagents for example:

$$G = k_{xy} n_x(t) n_y(t). \tag{4.3}$$

In a general form, the generation of ion-electron pairs by collision of electrons and neutral argon particles is described by Scheubert [2001] as

$$G = n_{\text{Ar}} \int_{E=E_{iz}}^{\infty} \sigma(E) \sqrt{\frac{2E}{m_e}} f(E) \mathrm{d}E. \tag{4.4}$$

Here E denotes the energy, $\sigma(E)$ the energy dependent ionization cross section, E_{iz} the minimum kinetic energy an electron needs to ionize via collisions and $f(E)$ the electron energy distribution function.

The electron energy distribution decreases exponentially with increasing energy as given by the Maxwellian electron energy distribution function (MEEDF)

$$f(E) = 2\sqrt{\frac{E}{\pi}} \left(\frac{1}{k_B T_e} \right)^{\frac{3}{2}} \exp\left(-\frac{E}{k_B T_e} \right), \tag{4.5}$$

and the ion generation by electron impact dominates in the energy region close to the ionization threshold energy E_{iz}. A simplification to avoid the integration over the whole energy dependent ionization cross section is the use of a simple step function for the cross section:

$$\sigma = \begin{cases} 0 & E < E_{\text{iz}}, \\ \sigma_T & E \geq E_{\text{iz}}. \end{cases} \tag{4.6}$$

Now the integration over a MEEDF can be carried out analytically and the ionization rate G is then given by

$$G = n_e n_{\text{Ar}} \sigma_T \sqrt{\frac{8}{\pi}} \sqrt{\frac{k_B T_e}{m_e}} \left(1 + \frac{E_{\text{iz}}}{k_B T_e} \right) \exp\left(-\frac{E_{\text{iz}}}{k_B T_e} \right). \tag{4.7}$$

Another simplification given by Meyyappan [1990b] is to neglect the temperature dependence of $E_{\text{iz}}/(k_B T_e)$ and to modify σ_T. But this assumption was not taken

into account in our reaction rate model.

In figure 4.2 different ionization rates are displayed, using data given by the different authors listed above. For an argon plasma with a neutral filling gas pressure of $p_0 = 1\,\text{Pa}$ and a neutral gas temperature of $T_\text{g} = 300\,\text{K}$, ionization rates were determined for an electron temperature range of $T_\text{e} = 1\cdot10^4 - 1\cdot10^5\,\text{K} \approx 1-10\,\text{eV}$. In figure 4.2 the full line shows the obtained ionization rate by integrating over a Maxwellian distribution and using an energy dependent ionization cross section as carried out by Lennon et al. [1988b]. The dashed line is an approximation which corresponds to the calculations done by Meyyappan [1990b], but with an ionization cross section of $\sigma_T = 3.0 \cdot 10^{-20}\,\text{m}^2$ worked out by Stewart et al. [1994]. The dot-dashed line is based on (4.7), with an ionization cross section $\sigma_T = 2.0 \cdot 10^{-20}\,\text{m}^2$ as used in the work of Meyyappan [1990b] and the dotted line is based on the data of Passchier [1993].

Figure 4.3 shows the ionization rate for the same parameters, using the rate same reaction model and taking (4.7) into account, showing a high agreement to the curves in figure 4.2. In general, the plots in figures 4.2 and 4.3 show a steep increase in regions of low electron temperatures ($T_\text{e} < 40000\,\text{K} \approx 3.5\,\text{eV}$) over several orders of magnitude. This region is of high interest since many low pressure plasmas operate in that electron temperature range, especially helicon discharges which are investigated in the preent work. At higher electron temperatures ($T_\text{e} > 60000\,\text{K} \approx 5.2\,\text{eV}$) the ionization rates tend to saturate and the differences between the various approximations vanish. Already in 1924 it was pointed out by Schottky [1924b] that the ambipolar diffusion coefficient of a low pressure discharge and the geometry determine the ionization rate. Schottkys calculations were done on a simple diffusion model, neglecting ion momentum and assuming that the particle density vanishes at the chamber wall.

The simulation results from Stewart et al. [1994], Meyyappan [1990b] and Lennon et al. [1988b] are all comparable. Only the approach by Passchier [1993] differs significantly. This is due to the fact that a minimum mean electron energy of $5.3\,\text{eV}$ is required to start any ionization processes by electron impact. This assumption is not used in our model.
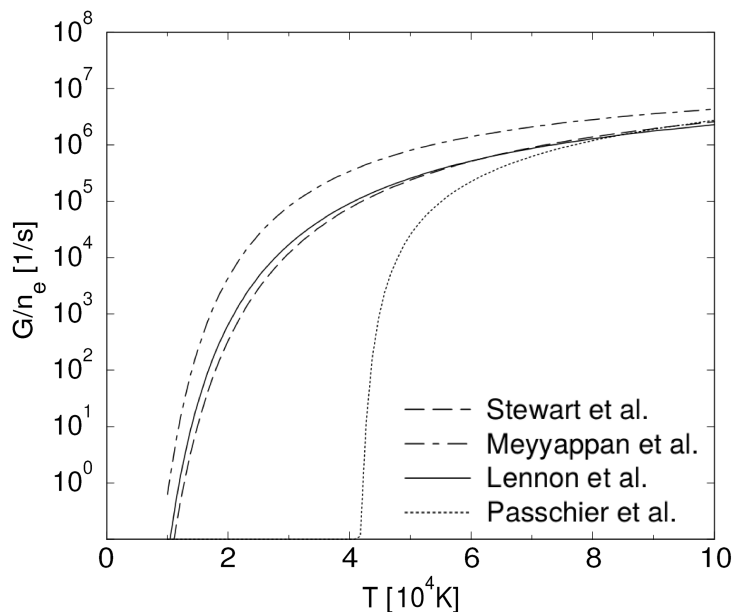
Figure 4.2: Ionization rates for argon. Calculations done in dependence on the electron temperature T_e at $p_0 = 1$Pa and $T_g = 300$K, taken from Scheubert [2001].
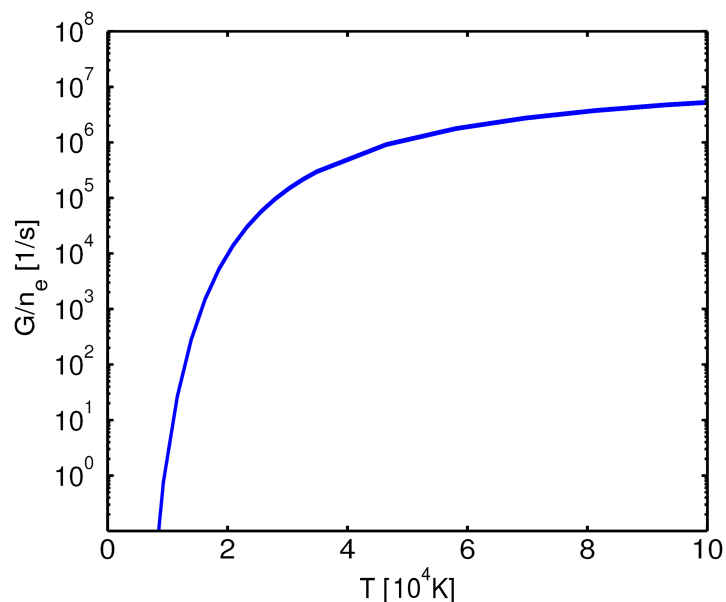

Figure 4.3: Ionization rates for argon. Calculations based on (4.7) and done in dependence on the electron temperature T_e at $p_0 = 1$Pa and $T_g = 300$K, using the cross-sections as in the implemented reaction rate model and done in dependence on the electron temperature T_e at $p_0 = 1$Pa and $T_g = 300$K.

4.1.2 Wall loss term

The modeling of the plasma in PROMETHEUS-A is based on the assumption that the electrons are described by a MEEDF and $T_e \gg T_i$. Since no radial profiles are directly considered in the model, the behavior of the charged particles at the sheath edge is described by a wall loss term.

The interaction of the plasma with an absorbing wall can be described as follows [Riemann, 1991]: The highly mobile electrons charge the wall negatively with respect to the surrounding plasma. Due to the repulsion of electrons, a positive space charge region ('sheath') with a typical extension of a few Debye lengths λ_D forms, which shields the neutral plasma from the negative wall. A stable sheath formation requires that the ions enter the sheath region with ion sound speed to render the shielding, as formulated in the Bohm criterion (see below). The early works of Langmuir [1929] uncovered basic features of plasma-sheath transitions. The kinetic analysis of a low-pressure plasma column of Tonks [1929b] already used an implicit form of the Bohm criterion. However, the explicit formulation and definite interpretation of the sheath condition was done by Bohm [1949b]. The Tonks-Langmuir problem was solved analytically by Harrison [1959]. They found a kinetic formulation of Bohm's criterion:

$$c_{is} \geq \sqrt{\frac{k_B T_e}{m_i}} = v_B, \tag{4.8}$$

where v_B is the Bohm-velocity and c_{is} the ion sound velocity. Since the plasma in PROMETHEUS-A is magnetized, the main loss channels are parallel to the ambient magnetic field. The wall loss term is parameterized as

$$W = A \left(\frac{2 S_{\parallel}}{V} \right) n_e \sqrt{\frac{k_B T_e}{m_i}}, \tag{4.9}$$

where A is an arbitrary scaling factor, $2S_{\parallel}$ is the surface area limiting the plasma parallel to the magnetic field to both sides and $n_e \sqrt{\frac{k_B T_e}{m_i}}$ is the Bohm flux $\Gamma_B = n_e v_B$.

The particles of the plasma are not only subject to parallel but also radial losses. Although latter are much smaller than the former due to the radial magnetic confinement in the helicon discharge, they may contribute to the total wall losses because its much larger effective surface.

To take it into account an arbitrary scaling factor A is introduced in (4.9), to

consider the diffusion of particles to the wall. If there are no losses of electrons and ions, the factor will set to $A = 0$. If only parallel losses are present, $A = 1$. A factor $A > 1$ includes also radial losses parametrically. Figure 4.4 shows a
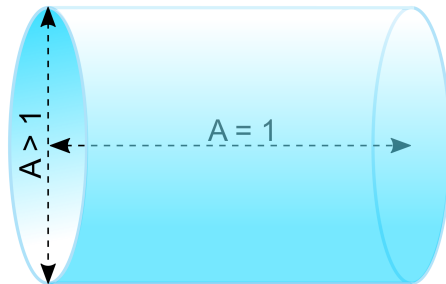

Figure 4.4: Schematic of possible wall losses. If $A = 1$ only losses along the magnetic field, if $A > 1$ radial losses are also included.

schematic depiction of the wall losses for charged particles.

Neutral metastable argon atoms also experience radial losses to the wall where they deexcite to the neutral argon ground state. It is described by the wall loss coefficient

$$k_{\mathrm{w(met)}} = \frac{1}{4}\gamma_{\mathrm{met}}\bar{v}_{\mathrm{met}}(S/V). \tag{4.10}$$

The factor $1/4$ results from the use of an isotropic Maxwellian energy distribution. The mean thermal velocity of the metastable argon particles is

$$\bar{v}_{\mathrm{met}} = \sqrt{\frac{8k_{\mathrm{B}}T_{\mathrm{g}}}{\pi m_{\mathrm{met}}}}, \tag{4.11}$$

where m_{met} is the metastable particle mass and T_{g} is the neutral gas temperature $T_{\mathrm{g}} = 400 - 800\,\mathrm{K}$ [Lee, 1995][Gudmundsson, 2001][Wainman et al., 1995], which is slightly higher than the wall temperature due to the high collisionality between electrons and neutrals. (Recent reports indicate T_{g} to be significantly higher than room temperature [Lee et al., 2017]). The factor γ_{met} is the sticking probability, which is constant for small energies. The vessel of PROMETHEUS-A is made out of glass, what results in a sticking probability of $\gamma_{\mathrm{met}} = 0.007$.

4.1.3   Overview of reactions

For the 14 energy levels, included in the 8 types of species, over 160 reactions are considered. All reactions and rate reaction labels with neutral argon or reactions related to the processes with singly ionized argon, argon dimers and argon trimers are compiled in table 4.2. A full overview of all reactions and their respective rate coefficient equations, values and sources for the different types of reactions are compiled in the tables 8.1-8.3 (appendix).

In the reaction rate model argon-electron, argon-argon and also three body collisions are included. Three body collisions only play a significant role in discharges with high neutral gas pressures $p > 100\,\mathrm{Pa}$. The helicon discharge investigated here is a collision dominated discharge and three body reactions are not generally neglected. Due to the low temperatures, reactions that require particle energies exceeding $50\,\mathrm{eV}$ are neglected.

Reactions included in the model are: ionization, excitation, recombination, metastable pooling, quenching, spontaneous emission, three body collision, dimer and trimer formation, dissociation and wall loss processes.

reactions with neutral argon			
	reaction	sort of atom	label
ionization	$\mathrm{Ar} + e \;\rightarrow\; \mathrm{Ar}^+ + e + e$		k_1
	$\mathrm{Ar}^\mathrm{i} + e \;\rightarrow\; \mathrm{Ar}^+ + e + e$		k_2
	$\mathrm{Ar}^\mathrm{e} + e \;\rightarrow\; \mathrm{Ar}^+ + e + e$		k_3
	$\mathrm{Ar}^\mathrm{f} + e \;\rightarrow\; \mathrm{Ar}^+ + e + e$		k_4
	$\mathrm{Ar}^\mathrm{i} + e \;\rightarrow\; \mathrm{Ar}^{+\mathrm{f}} + e + e$		k_5
	$\mathrm{Ar}^\mathrm{f} + e \;\rightarrow\; \mathrm{Ar}^{+\mathrm{f}} + e + e$		k_6
el. coll. excitation	$\mathrm{Ar} + e \;\rightarrow\; \mathrm{Ar}^\mathrm{i} + e$		k_7
	$\mathrm{Ar} + e \;\rightarrow\; \mathrm{Ar}^\mathrm{e} + e$		k_8
	$\mathrm{Ar} + e \;\rightarrow\; \mathrm{Ar}^\mathrm{f} + e$		k_9
recombination	$\mathrm{Ar}^+ + e \;\rightarrow\; \mathrm{Ar}$		k_{10}
metastable pooling	$\mathrm{Ar}^\mathrm{x} + \mathrm{Ar}^\mathrm{y} \;\rightarrow\; \mathrm{Ar}^+ + \mathrm{Ar} + e$	x = i,e,f,x = y	k_{11}
	$\mathrm{Ar}^\mathrm{x} + \mathrm{Ar}^\mathrm{x} \;\rightarrow\; \mathrm{Ar} + \mathrm{Ar}^\mathrm{x}$	x = i,e,f	k_{12}
	$\mathrm{Ar}^\mathrm{x} + \mathrm{Ar} \;\rightarrow\; \mathrm{Ar} + \mathrm{Ar}$	x = i,e,f	k_{13}
electron quenching	$\mathrm{Ar}^\mathrm{x} + e \;\rightarrow\; \mathrm{Ar} + e$	x = i,e,f	k_{14}
spontaneous emission	$\mathrm{Ar}^\mathrm{e} \;\rightarrow\; h\nu + \mathrm{Ar}^\mathrm{i}$		k_{15}
	$\mathrm{Ar}^\mathrm{e} \;\rightarrow\; h\nu + \mathrm{Ar}^\mathrm{f}$		k_{16}
	$\mathrm{Ar}^\mathrm{i} \;\rightarrow\; h\nu + \mathrm{Ar}$		k_{17}
	$\mathrm{Ar}^\mathrm{f} \;\rightarrow\; h\nu + \mathrm{Ar}$		k_{18}
penning ionization	$\mathrm{Ar}^\mathrm{x} + \mathrm{Ar}^\mathrm{y} \;\rightarrow\; \mathrm{Ar}^+ + \mathrm{Ar} + e$	x = i,e,f, $x \neq y$	k_{19}

	reaction	sort of atom	label
excited state kinetics	$\mathrm{Ar^e + Ar \rightarrow Ar^f + Ar}$		k_{19}
three body collisions	$\mathrm{Ar^+ + 2e \rightarrow Ar + e}$		k_{20}
	$\mathrm{Ar^x + Ar + Ar \rightarrow Ar + Ar + Ar}$	x = i,e,f	k_{21}
	$\mathrm{Ar^+ + e + Ar^x \rightarrow Ar + Ar^x}$	x = g,i,e,f	k_{22}
	$\mathrm{Ar^+ + e + e \rightarrow Ar^i + e}$		k_{23}
	$\mathrm{Ar^+ + e + e \rightarrow Ar^f + e}$		k_{24}
wall interaction	$\mathrm{Ar^x + wall \rightarrow Ar}$	x = i,e,f	k_{w1}

reactions with singly ionized argon

	reaction	sort of atom	label
ionization	$\mathrm{Ar^+ + e \rightarrow Ar^{++} + e + e}$		k_{25}
	$\mathrm{Ar^{+i} + e \rightarrow Ar^{++} + e + e}$		k_{26}
	$\mathrm{Ar^{+e} + e \rightarrow Ar^{++} + e + e}$		k_{27}
	$\mathrm{Ar^{+f} + e \rightarrow Ar^{++} + e + e}$		k_{28}
el. coll. excitation	$\mathrm{Ar^+ + e \rightarrow Ar^{+i} + e}$		k_{29}
	$\mathrm{Ar^+ + e \rightarrow Ar^{+e} + e}$		k_{30}
	$\mathrm{Ar^+ + e \rightarrow Ar^{+f} + e}$		k_{31}
	$\mathrm{Ar^{+i} + e \rightarrow Ar^{+e} + e}$		k_{32}
penning ionization	$\mathrm{Ar^{++} + Ar \rightarrow Ar^{++} + Ar^+ + e}$		k_{33}
	$\mathrm{Ar^{+x} + Ar^x \rightarrow Ar^{++} + Ar + e}$	x = i,e,f	k_{34}
metastable pooling	$\mathrm{Ar^{++} + Ar \rightarrow Ar^+ + Ar^+}$		k_{35}
	$\mathrm{Ar^{++} + Ar \rightarrow Ar^{+i} + Ar^+}$		k_{36}
	$\mathrm{Ar^{++} + Ar \rightarrow Ar^{+e} + Ar^+}$		k_{37}
	$\mathrm{Ar^{++} + Ar \rightarrow Ar^{+f} + Ar^+}$		k_{38}
	$\mathrm{Ar^{++} + Ar^x \rightarrow Ar^{+x} + Ar^+}$	x = i,e,f	k_{39}
recombination	$\mathrm{Ar^{+x} + e \rightarrow Ar}$	x = i,e,f	k_{40}
	$\mathrm{Ar^{++} + e \rightarrow Ar^+}$		k_{41}
spontaneous emission	$\mathrm{Ar^{+e} \rightarrow h\nu + Ar^{+f}}$		k_{42}
	$\mathrm{Ar^{+e} \rightarrow h\nu + Ar^{+i}}$		k_{43}
	$\mathrm{Ar^{+e} \rightarrow h\nu + Ar^+}$		k_{44}
	$\mathrm{Ar^{+f} \rightarrow h\nu + Ar^+}$		k_{45}
excited state kinetics	$\mathrm{Ar^{+x} + Ar \rightarrow Ar^+ + Ar}$	x = i,e,f	k_{46}
wall interaction	$\mathrm{Ar^{+x} + wall \rightarrow Ar}$	x = g,i,e,f	k_{w2}
	$\mathrm{Ar^{++} + wall \rightarrow Ar}$		k_{w3}

reactions with argon dimers and trimers

	reaction	sort of atom	label
dimer and trimer formation	$\mathrm{Ar^+ + Ar + Ar \rightarrow Ar_2^+ + Ar}$		k_{47}
	$\mathrm{Ar^x + Ar \rightarrow Ar_2^+ + e}$	x = i,e,f	k_{48}
	$\mathrm{Ar_2^+ + Ar + Ar \rightarrow Ar_3^+ + Ar}$		k_{49}
	$\mathrm{Ar^e + Ar + Ar \rightarrow Ar_2^e + Ar}$		k_{50}
	$\mathrm{Ar^i + Ar + Ar \rightarrow Ar_2^i + Ar}$		k_{51}
	$\mathrm{Ar^f + Ar + Ar \rightarrow Ar_2^f + Ar}$		k_{52}
ionization	$\mathrm{Ar_2^e + e \rightarrow Ar_2^+ + e + e}$		k_{53}
	$\mathrm{Ar_2^x + e \rightarrow Ar_2^+ + e + e}$	x = i,f	k_{54}

	reaction	sort of atom	label
recombination	$Ar_2^+ + e + e \rightarrow Ar_2^x + e$	x = i,f	k_{55}
collisional	$Ar_3^+ + e \rightarrow Ar^e + Ar + Ar$		k_{56}
dissociation	$Ar_3^+ 0 + e \rightarrow Ar^x + Ar + Ar$	x = i,f	k_{57}
	$Ar_3^+ + Ar \rightarrow Ar_2^+ + Ar + Ar$		k_{58}
	$Ar_2^+ + e \rightarrow Ar^e + Ar$		k_{59}
	$Ar_2^x + e \rightarrow Ar + Ar + e$	x = i,f	k_{60}
	$Ar_2^i + e \rightarrow Ar^i + Ar + e$		k_{61}
	$Ar_2^f + e \rightarrow Ar^f + Ar + e$		k_{62}
	$Ar_2^+ + Ar \rightarrow Ar^+ + Ar + Ar$		k_{63}
	$Ar_2^e + Ar \rightarrow Ar^x + Ar + Ar$	x = i,f	k_{64}
	$Ar_2^x + Ar_2^x \rightarrow Ar_2^x + Ar + Ar$	x = i,e,f	k_{65}
	$Ar_2^x + Ar_2^x \rightarrow Ar + Ar + Ar + Ar$	x = i,e,f	k_{66}
	$Ar_2^x + Ar_2^x \rightarrow Ar_3 + Ar$	x = i,e,f	k_{67}
spontaneous	$Ar_2^+ \rightarrow Ar + Ar^+$		k_{68}
dissociation	$Ar_2^e \rightarrow h\nu + Ar + Ar$		k_{69}
	$Ar_2^x \rightarrow h\nu + Ar + Ar$	x = i,f	k_{70}
el. coll. excitation	$Ar_2^x + e \rightarrow Ar_2^e + e$	x = i,f	k_{71}
penning ionization	$Ar_2^x + Ar_2^x \rightarrow Ar_2^+ + Ar + Ar + e$	x = i,e,f	k_{72}
	$Ar^x + Ar^x \rightarrow Ar_2^+ + e$	x = i,e,f	k_{73}
	$Ar_2^x + Ar^x \rightarrow Ar_2^+ + Ar + e$	x = i,e,f	k_{74}
wall interaction	$Ar_2^x + wall \rightarrow Ar + Ar$	x = i,e,f	k_{w4}
	$Ar_2^+ + wall \rightarrow Ar + Ar$		k_{w5}
	$Ar_3^+ + wall \rightarrow Ar + Ar + Ar$		k_{w6}

Table 4.2: Overview of reactions with neutral, ionized argon or argon dimers and trimers.

4.1.4   Rate equations

The particle balance equations for the charged particles, shown here for the single ionized argon ground state $\mathrm{Ar^+}$ are given by

$$\frac{\mathrm{d}n_{\mathrm{Ar^+}}}{\mathrm{d}t} = G_{\text{source}}^{\mathrm{Ar^+}} - G_{\text{loss}}^{\mathrm{Ar^+}} - W^{\mathrm{Ar^+}}, \tag{4.12}$$

where $W^{\mathrm{Ar^+}} = A\left(\frac{2S}{V}\right)\Gamma_{\mathrm{Ar^+}}$ is the wall loss term derived in (4.9). The source and loss terms for this specific state read to be

$$
\begin{aligned}
G_{\text{source}}^{\mathrm{Ar^+}} = {} & k_1 n_{\mathrm{Ar}} n_{\mathrm{e}} + k_2 n_{\mathrm{Ar^i}} n_{\mathrm{e}} + k_3 n_{\mathrm{Ar^e}} n_{\mathrm{e}} + k_4 n_{\mathrm{Ar^f}} n_{\mathrm{e}} + k_{11} n_{\mathrm{Ar^i}} n_{\mathrm{Ar^i}} \\
& + k_{11} n_{\mathrm{Ar^e}} n_{\mathrm{Ar^e}} + k_{11} n_{\mathrm{Ar^f}} n_{\mathrm{Ar^f}} + k_{19} n_{\mathrm{Ar^i}} n_{\mathrm{Ar^f}} + k_{19} n_{\mathrm{Ar^i}} n_{\mathrm{Ar^e}} + k_{19} n_{\mathrm{Ar^e}} n_{\mathrm{Ar^f}} \\
& + k_{46} n_{\mathrm{Ar^{i+}}} n_{\mathrm{Ar}} + k_{46} n_{\mathrm{Ar^{e+}}} n_{\mathrm{Ar}} + k_{46} n_{\mathrm{Ar^{f+}}} n_{\mathrm{Ar}} + k_{41} n_{\mathrm{Ar^{2+}}} n_e \\
& + 2 k_{35} n_{\mathrm{Ar^{2+}}} n_{\mathrm{Ar}} + 3 k_{39} n_{\mathrm{Ar^{2+}}} n_{\mathrm{Ar^i}} + 3 k_{39} n_{\mathrm{Ar^{2+}}} n_{\mathrm{Ar^e}} + 3 k_{39} n_{\mathrm{Ar^{2+}}} n_{\mathrm{Ar^f}} \\
& + k_{36} n_{\mathrm{Ar^{2+}}} n_{\mathrm{Ar}} + k_{37} n_{\mathrm{Ar^{2+}}} n_{\mathrm{Ar}} + k_{38} n_{\mathrm{Ar^{2+}}} n_{\mathrm{Ar}} + k_{33} n_{\mathrm{Ar^{2+}}} n_{\mathrm{Ar}} \\
& + k_{45} n_{\mathrm{Ar^{f+}}} + k_{44} n_{\mathrm{Ar^{e+}}} + k_{68} n_{\mathrm{Ar_2^+}} + k_{63} n_{\mathrm{Ar_2^+}} n_{\mathrm{Ar}}
\end{aligned}
$$

$$
\begin{aligned}
G_{\text{loss}}^{\mathrm{Ar^+}} = {} & k_{10} n_{\mathrm{Ar^+}} n_{\mathrm{e}} + k_{20} n_{\mathrm{Ar^+}} n_{\mathrm{e}} n_{\mathrm{e}} + k_{22} n_{\mathrm{Ar^+}} n_{\mathrm{e}} n_{\mathrm{Ar^i}} + k_{22} n_{\mathrm{Ar^+}} n_{\mathrm{e}} n_{\mathrm{Ar^e}} \\
& + k_{22} n_{\mathrm{Ar^+}} n_{\mathrm{e}} n_{\mathrm{Ar^f}} + k_{22} n_{\mathrm{Ar^+}} n_{\mathrm{e}} n_{\mathrm{Ar}} + k_{23} n_{\mathrm{Ar^+}} n_{\mathrm{e}} n_{\mathrm{e}} + k_{24} n_{\mathrm{Ar^+}} n_{\mathrm{e}} n_{\mathrm{e}} \\
& + k_{29} n_{\mathrm{Ar^+}} n_{\mathrm{e}} + k_{30} n_{\mathrm{Ar^+}} n_{\mathrm{e}} + k_{31} n_{\mathrm{Ar^+}} n_{\mathrm{e}} + k_{25} n_{\mathrm{Ar^+}} n_{\mathrm{e}} + k_{47} n_{\mathrm{Ar^+}} n_{\mathrm{Ar}} n_{\mathrm{Ar}}
\end{aligned}
$$

and are inserted into (4.12) to yield a differential equation for the single ionized argon ground state $\mathrm{Ar^+}$. For all other atomic states from the model the equations are derived analogously and represent in total a full set of differential equations which needs to be solved self-consistently. The sum of particles over all atomic states is kept constant during the complete run.

4.2   Results of the model calculations

4.2.1   Primal results

A cylindrical argon plasma is modelled by the 0DRRM, with a typical neutral gas filling pressure in the range of $p_0 = 1 - 30\,\mathrm{Pa}$. For a predefined temperature range of $T_\mathrm{e} = 0.5 - 4.0\,\mathrm{eV}$ solutions of the reaction rate calculations yield the respective densities n_e, n_Ar, $n_{\mathrm{Ar}^\mathrm{i}}$, $n_{\mathrm{Ar}^\mathrm{e}}$, $n_{\mathrm{Ar}^\mathrm{f}}$, $n_{\mathrm{Ar}_2^\mathrm{i}}$, $n_{\mathrm{Ar}_2^\mathrm{e}}$, $n_{\mathrm{Ar}_2^\mathrm{f}}$, n_{Ar^+}, $n_{\mathrm{Ar}^{\mathrm{i}+}}$, $n_{\mathrm{Ar}^{\mathrm{e}+}}$, $n_{\mathrm{Ar}^{\mathrm{f}+}}$, $n_{\mathrm{Ar}^+_2}$, $n_{\mathrm{Ar}^+_3}$ and $n_{\mathrm{Ar}^{2+}}$. The densities of all species included in the reaction rate model establish an equilibrium during the calculation run. The steady state condition for all included species is typically achieved after approximately $t = 1\,\mathrm{ms}$.

Figure 4.5 depicts the temporal evolution of neutral argon, ionized argon and the two initial metastable argon states for neutral and singly ionized argon for an electron temperature of $T_\mathrm{e} = 1.4\,\mathrm{eV}$, an neutral filling gas pressure of $p_0 = 6\,\mathrm{Pa}$, what corresponds to a neutral argon density of $n_\mathrm{Ar} = 1.45 \cdot 10^{21}\,\mathrm{m}^{-3}$, and a wall loss factor of $A = 0.001$. Starting from the initial densities of $n_\mathrm{Ar} = 1.45 \cdot 10^{21}\,\mathrm{m}^{-3}$, $n_{\mathrm{Ar}^+} = n_{\mathrm{Ar}^\mathrm{e}} = 1 \cdot 10^8\,\mathrm{m}^{-3}$ and $n_{\mathrm{Ar}^\mathrm{i}} = n_{\mathrm{Ar}^\mathrm{e}} = n_{\mathrm{Ar}^\mathrm{f}} = n_{\mathrm{Ar}_2^\mathrm{i}} = n_{\mathrm{Ar}_2^\mathrm{e}} = n_{\mathrm{Ar}_2^\mathrm{f}} = n_{\mathrm{Ar}^{\mathrm{i}+}} = n_{\mathrm{Ar}^{\mathrm{e}+}} = n_{\mathrm{Ar}^{\mathrm{f}+}} = n_{\mathrm{Ar}^+_2} = n_{\mathrm{Ar}^+_3} = n_{\mathrm{Ar}^{2+}} = 0$ the corresponding species undergo reactions defined by the reactions rate constants. Since the calculations in this example are done for a high plasma density regime in the centrally localized helicon plasma, only axial wall losses are included. The neutral argon is not kept constant due to the small collisional ionization mean free path for the neutrals moving inwards.

It results in a decrease of n_Ar and in an increase of all other particle densities during the calculation run, resulting in an equilibrium state with $n_\mathrm{Ar} = 1.03 \cdot 10^{21}\,\mathrm{m}^{-3}$, $n_\mathrm{e} = 4.19 \cdot 10^{20}\,\mathrm{m}^{-3}$, $n_{\mathrm{Ar}^\mathrm{i}} = 2.51 \cdot 10^{15}\,\mathrm{m}^{-3}$, $n_{\mathrm{Ar}^{\mathrm{i}+}} = 5.30 \cdot 10^{14}\,\mathrm{m}^{-3}$. The time evolution of the respective densities is depicted in figure 4.5. Since the electron temperature is the most important parameter determining the density of the different states, figure 4.6 shows the results of the model calculation in the range $T_\mathrm{e} = 0 - 10\,\mathrm{eV}$ together with a comparison to independent model calculations in figure 4.7. As shown in figure 4.7 the neutral argon density (black line) starts to decline at around $T_\mathrm{e} = 1\,\mathrm{eV}$ due to the beginning of the ionization processes visible in the increasing Ar^+ density (red line). With higher electron temperature, sufficient electron energy gets available to ionize the argon plasma further to Ar^{2+} (blue line). The Ar^{2+} density of starts to increase at around $T_\mathrm{e} = 2.5\,\mathrm{eV}$ resulting in a decrease of n_{Ar^+}. The temperature dependent behavior is expected and rep-
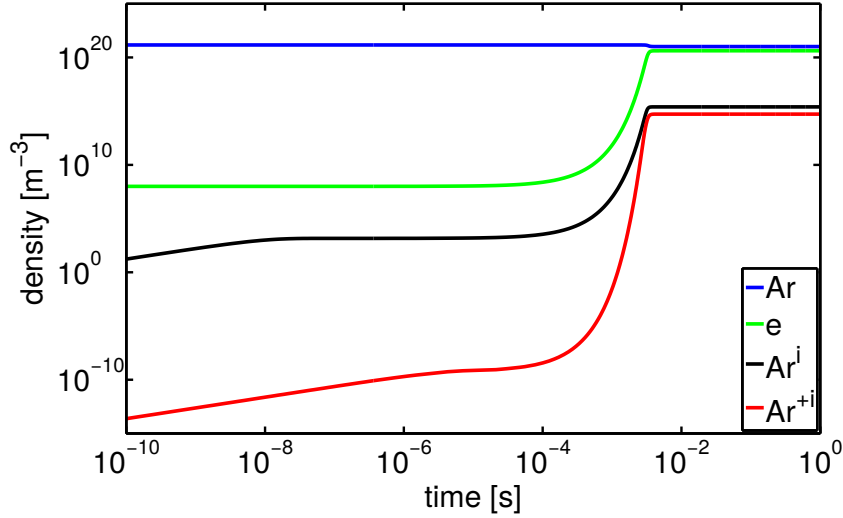
Figure 4.5: Evolution of density of different states during the calculation run.

resents qualitatively an argon plasma discharge system, with the exception that at temperatures at $T_e = 5\,\mathrm{eV}$ the neutral gas is almost completely ionized. This condition is generally not reached in gas discharges due to the lack of heating power.

Compared to other calculations as shown in figure 4.6 the here implemented reaction rate model shows on the one hand a good agreement in the temperature dependent density evolution where on the other hand the maximum fractional abundance is different for $n_{\mathrm{Ar+}}$ and $n_{\mathrm{Ar^{2+}}}$. In the first case of $n_{\mathrm{Ar+}}$, the difference is explained by the fact that in the present model the second ionization level starts to be occupied higher electron temperatures compared to the one descibed by Loch et al. [2007]. The difference in the density maximum is just explained by the boundary condition that no further ionization is taken into account and Ar^{2+} can rise up to a fraction of 100%.

To validate the reaction rate model over a wide variation range of parameters, calculation runs were performed for $0.5\,\mathrm{eV} < T_e < 4\,\mathrm{eV}$ and $1\,\mathrm{Pa} < p_0 < 30\,\mathrm{Pa}$ with the same intitial densities as in the case shown in figure 4.5, excluding n_{Ar} as variable parameter. The resulting neutral argon ground state density n_{Ar} and plasma density n_e are shown in figures 4.8 and 4.9, respectively. The resulting densities show the same behavior as already shown in figure 4.7, but just scaled up to higher initial densities. The first rise in plasma density in figure 4.9 is due to the first ionization step and the second rise in plasma density around $T_e = 2.5\,\mathrm{eV}$ constitutes the starting phase of the ionization process to Ar^{2+}. The neutral density in figure 4.8 consequently shows the inverse behavior to the plasma density.
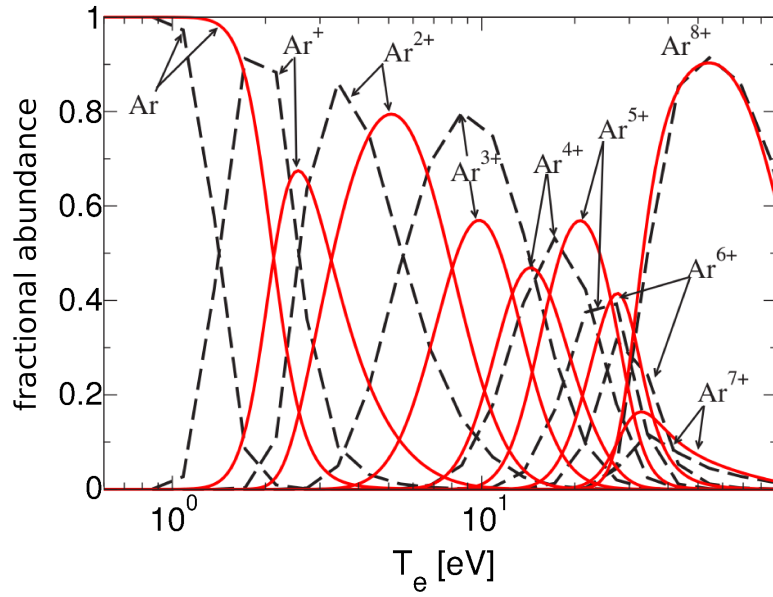
Figure 4.6: Comparison of the occupation of ionization levels. Equilibrium ion-stage balance for $Ar - Ar^{+8}$. Solid line, distorted-wave atomic data; dashed line, older atomic data. Figure taken from [2007]
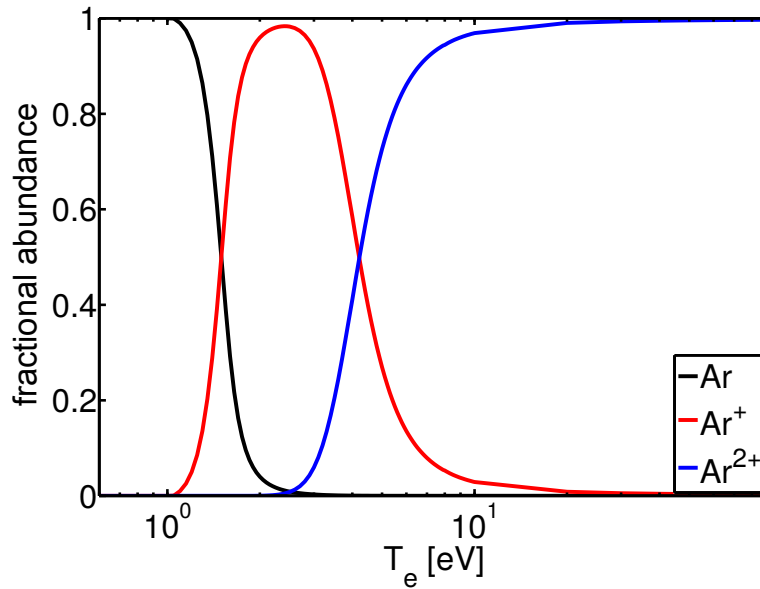
Figure 4.7: Population of the two different ionization stages. Neutral argon density (black line) starts to decline at the beginning of the ionization process and the density of Ar^+ (red line) increases. With higher electron temperature the argon plasma gets further ionized to Ar^{2+} (blue line).
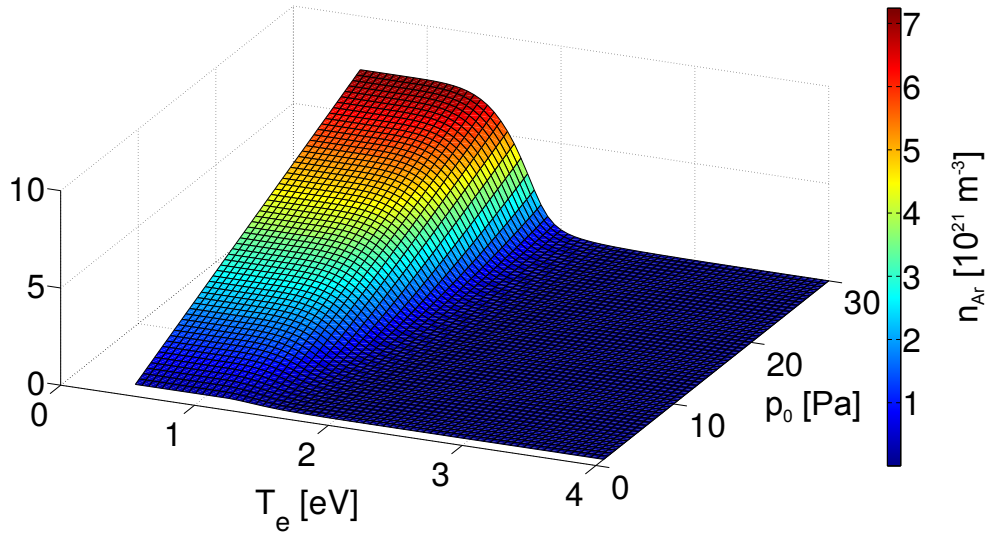
Figure 4.8: Density of neutral argon for increasing temperature and filling gas pressure.
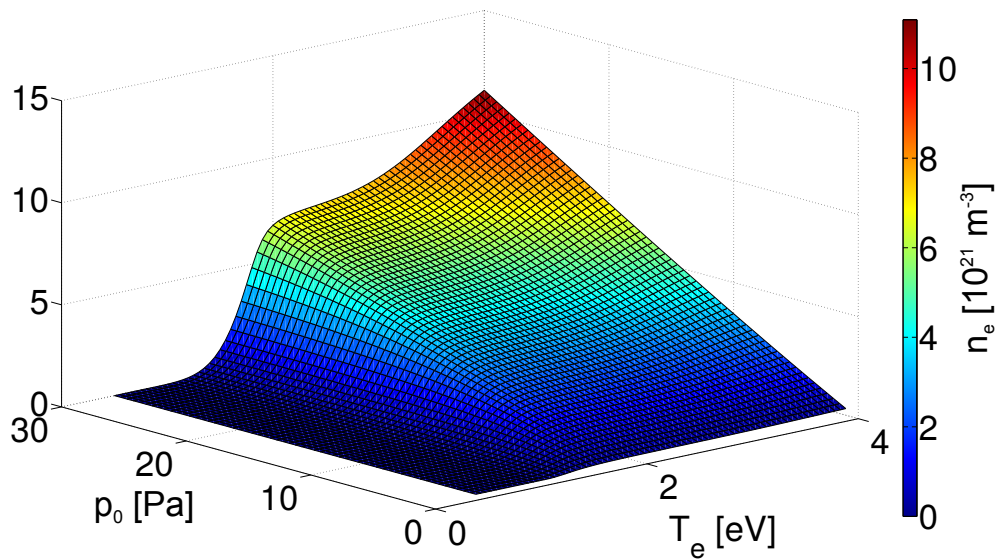
Figure 4.9: Plasma density for increasing temperature and filling gas pressure.

The dependence is valid over the whole scanned pressure range.

To understand in detail the global behavior, linked to the variation of electron temperature and filling gas pressure, these dependences have been split into single reaction rate channels for sources and sinks for n_{Ar} and n_e. The main sources and sinks for the argon ground state at constant gas pressure of $p_0 = 6\,Pa$ are displayed in figure 4.10a and 4.10b, respectively. Since the reaction rates of the respective metastable LIF states are very similar, only the one for Ar^i is shown. The process of electron quenching (blue line) and spontaneous emission (green line) of the metastable states are the most important sources for Ar. As depicted in figure 4.10b collisional ionization (blue line) and excitation by electrons (green line) are the main loss channels for this state. For the electron production channels, shown in figure 4.10c, the most important reactions are collisional ionization by electrons with neutrals (blue line) and metastable states (green line). The reactions with the highest influence on the loss of electrons (figure 4.10d) are both three body recombinations, the first one to the argon ground state (green line) and the second one with two electrons as additional reagents to a metastable state (cyan line).
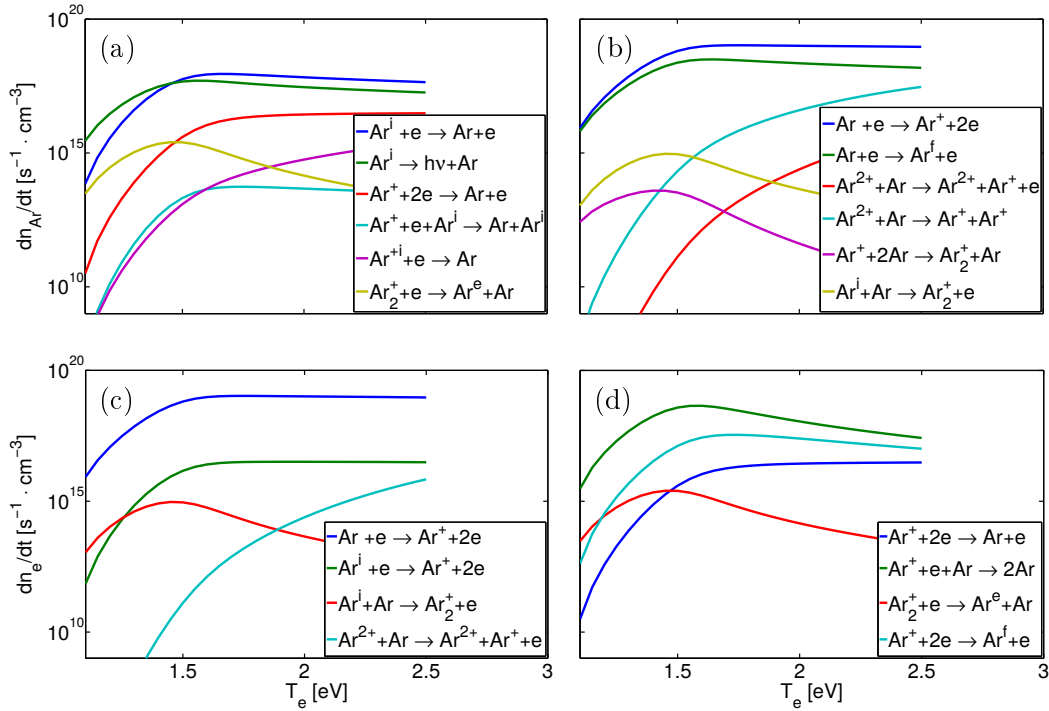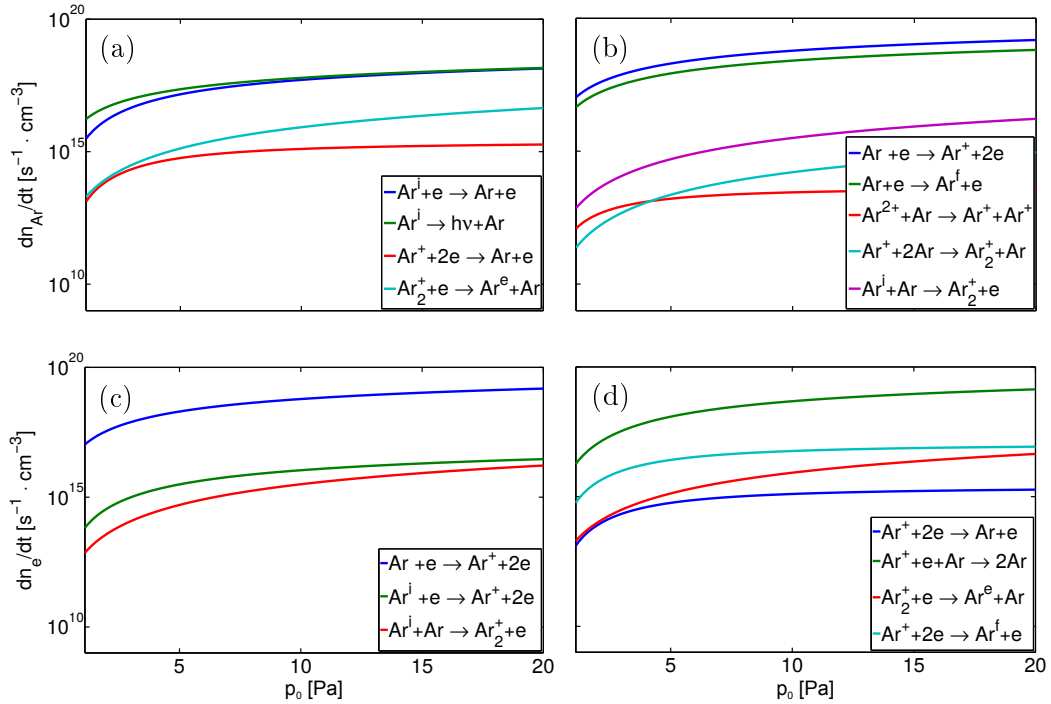

Figure 4.10: Main source and loss channels for argon ground state density n_{Ar}, (a) and (b) and plasma density n_e, (c) and (d) calculated by the reaction rate model at a neutral filling gas pressure of $p_0 = 6\,Pa$.

The same procedure was done for a constant electron temperature of $T_e = 1.4\,\text{eV}$ and a variable neutral gas pressure, varying over $p_0 \leq 20\,\text{Pa}$. The resulting rate reactions are shown in figure 4.11. Compared to the reaction rates with varying electron temperature, cf. figure 4.10, the main source and sink reactions are the same as for constant filling gas pressure and varying electron temperature. As shown in figure 4.11a the source reaction for neutral argon of electron quenching (blue line) becomes dominant at high pressures of around $p_0 = 15 - 20\,\text{Pa}$ in the low electron temperature regime under consideration. Compared to the quenching mechanism dependence shown in figure 4.10a, the quenching rate is not as sensitive to pressure variation as it is to temperature variation. It holds true for many of various reaction rate channels.

Figure 4.11: Main source and loss channels for argon ground state density n_{Ar}, (a) and (b) and plasma density n_e, (c) and (d) calculated by the reaction rate model at a constant electron temperature of $T_e = 1.4\text{eV}$.

4.2.2 Dependence of metastable densities

The metastable argon states $\mathrm{Ar^i}$,$\mathrm{Ar^e}$,$\mathrm{Ar^f}$,$\mathrm{Ar^{i+}}$,$\mathrm{Ar^{e+}}$ and $\mathrm{Ar^{f+}}$ (see section 4.1.1 for details) are included in our model to represent the required atomic states for the laser induced fluorescence measurements.

The dependence of $n_{\mathrm{Ar^i}}$ in a range of $0.5\,\mathrm{eV} < T_e < 4\,\mathrm{eV}$ and $1\,\mathrm{Pa} < p_0 < 30\,\mathrm{Pa}$ is shown in figure 4.12. The density of the metastable state behaves differently than the ground state densities shown in figures 4.8 and 4.9. Starting at an electron temperature of $T_e = 1\,\mathrm{eV}$, the density starts to increase to a maximum at around $T_e = 1.6\,\mathrm{eV}$. After this point, the metastable density decreases and converges to a low-level density for higher electron temperatures. To explain that behaviour, it is necessary to take a closer look into the different source and sink channels for this state, which are compiled in figures 4.14 and 4.15 for a constant gas pressure of $p_0 = 6\,\mathrm{Pa}$ and electron temperature of $T_e = 1.4\,\mathrm{eV}$, respectively.

The main sources in both cases are electron collision excitation (blue lines) and recombination from argon ions (red lines), see figures 4.14a and 4.15a. The equivalent rates start to rise after $T_e = 1\,\mathrm{eV}$ and saturate at $T_e \approx 1.5\,\mathrm{eV}$. That is the point where in the loss channels (see figure 4.14b) the electron quenching rate (green line) gets larger than the spontaneous emission (red line). The decrease of the metastable density happens due to the crossing and the continuing steep increase of the charge exchange reaction (cyan line, figure 4.14b), which has the highest rate at $T_e > 2.3\,\mathrm{eV}$.

The initial metastable ion density is not showing this behavior at all and has no clear turning point in the considered temperature regime. It shows a saturation of the density at $T_e \approx 4\,\mathrm{eV}$ and a slight indication of a starting decline, but not in the temperature regime of our helicon discharge. The most important source channels for $\mathrm{Ar^{i+}}$, depicted in figures 4.14c and 4.15c, are the electron collision excitation (blue line) and spontaneous emission from the metastable excited state of the argon ion (green line). These sources are just opposed by losses which are several orders of magnitude lower throughout the whole intervall of temperature and pressure variation. The most relevant sinks (see figures 4.14d and 4.15d) are the quenching by collisions with neutral argon particles (blue line) and the ionization by electron collisions (red line). The difference in magnitude results in the continuous increasing of metastable ion density over the full parameter space.
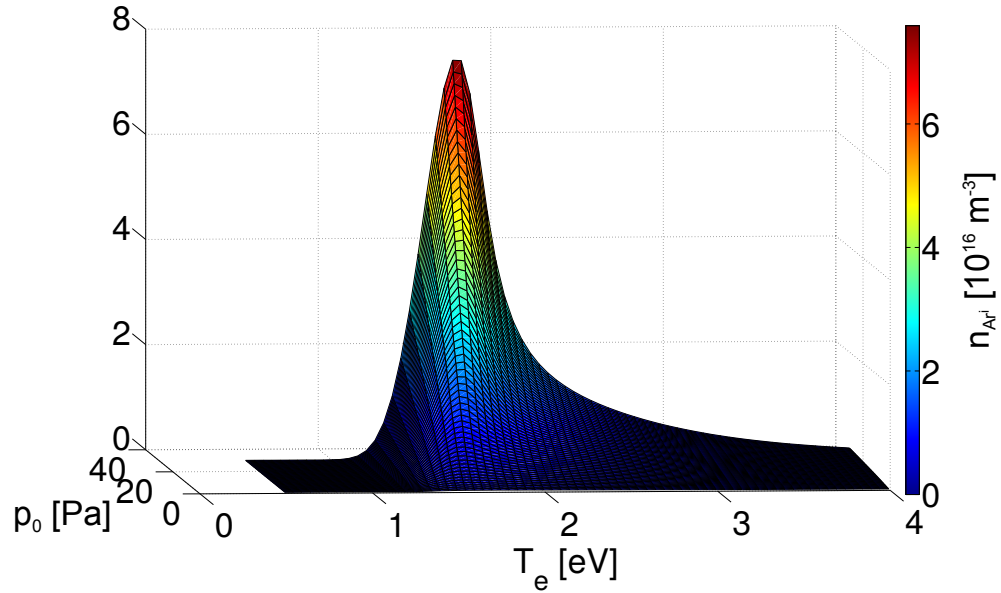
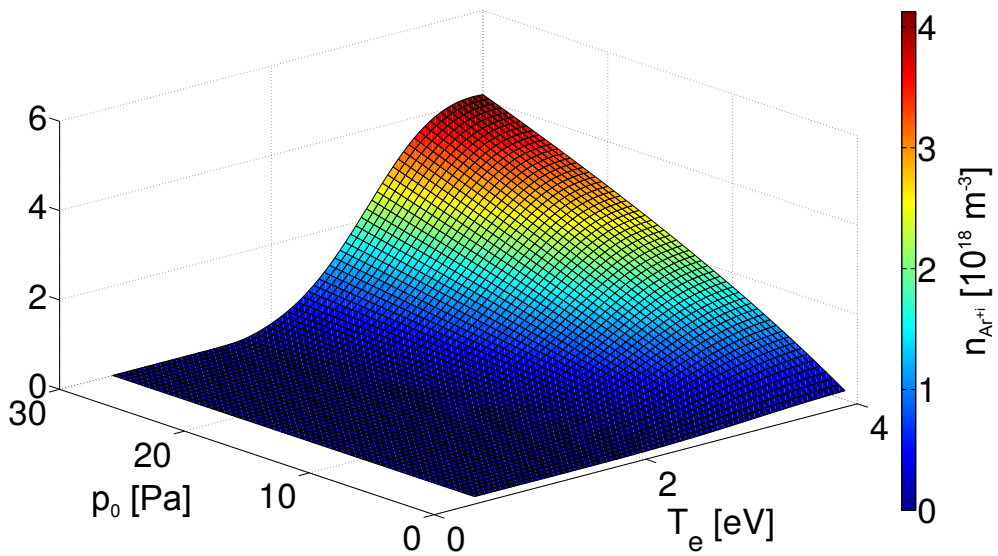Figure 4.12: Neutral argon metastable (Ar^i) density for increasing temperature and filling gas pressure.

Figure 4.13: Ion argon metastable (Ar^{i+}) density for increasing temperature and filling gas pressure.
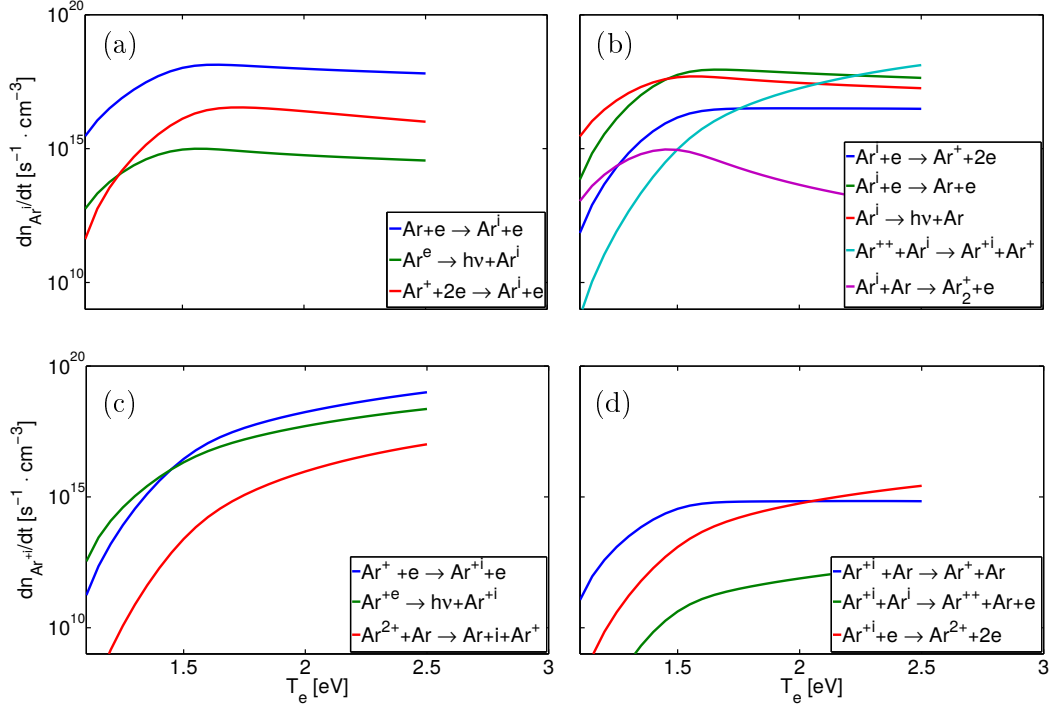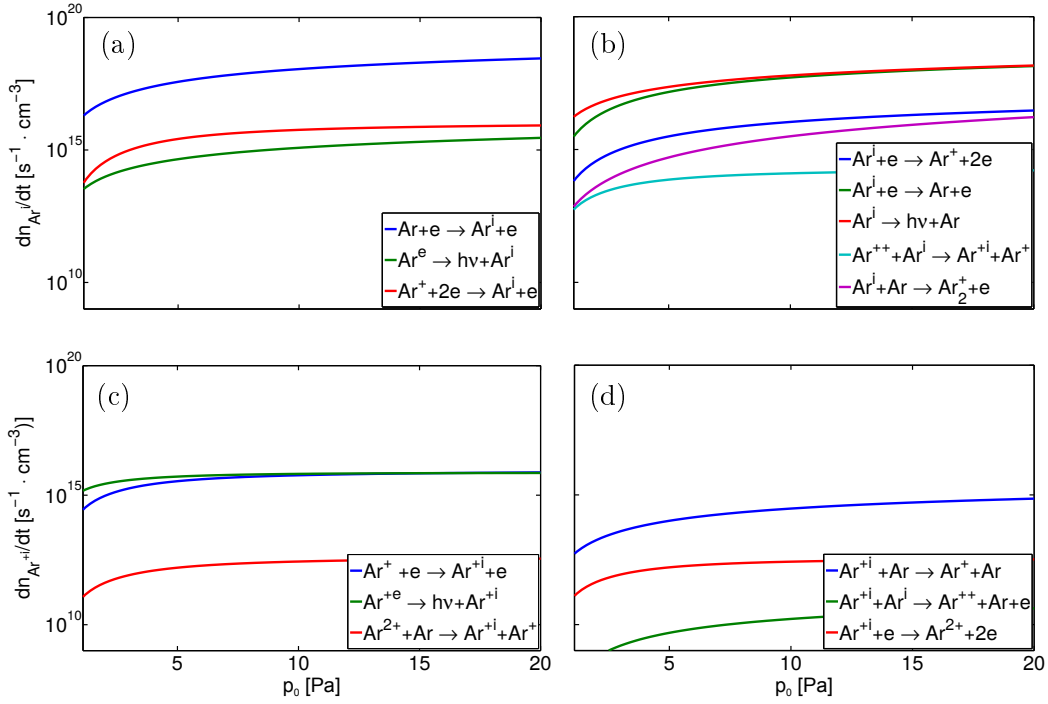
Figure 4.14: Main source and loss channels for initial neutral metastable density $n_{\mathrm{Ar^i}}$, (a) and (b) and single ionized argon metastable density $n_{\mathrm{Ar^{+i}}}$, (c) and (d) calculated by the reaction rate model at a neutral filling gas pressure of $p_0 = 6\,\mathrm{Pa}$.

Figure 4.15: Main source and loss channels for neutral argon metastable density $n_{\mathrm{Ar^i}}$, (a) and (b) and single ionized argon metastable density $n_{\mathrm{Ar^{+i}}}$, (c) and (d) calculated by the reaction rate model at a constant electron temperature of $T_e = 1.4\,\mathrm{eV}$.

Chapter 5

Experimental set-up, diagnostics and numerical methods

5.1 PROMETHEUS-A

As outlined in section 2.2, a high-density plasma discharge is required to build up electric fields in the order of GV/m to accelerate electrons to energies in the TeV range with proton driving bunches. Up to now, the highest accelerating fields generated are around $100\,\mathrm{GV/m}$ on a centimeter-scale [Hogan et al., 2005]. But to design a future PWFA like it is done in the AWAKE project ([Gschwendtner et al., 2016], see section 2.2.2) plasma sources are needed that are able to maintain discharges with plasma densities of $n_\mathrm{e} \geq 7 \cdot 10^{20}\,\mathrm{m^{-3}}$ over distances of tens or hundreds of meters. Helicon plasma discharges are a promising concept to create plasma densities relevant for PWFAs (3.3). In the present work, such a plasma is created and characterized in the PROMETHEUS-A device, the **Pro**totype **M**odule for **E**xperiments on High Power **He**licons as **U**niform Plasma **S**ource for **A**WAKE.

5.1.1 Experimental set-up

The experimental set-up is schematically shown in figure 5.1, complemented with a photo shown in figure 5.2. The PROMETHEUS-A consists of a one meter long glass tube with an inner diameter of $d = 44\,\mathrm{mm}$ and three radial ports with an
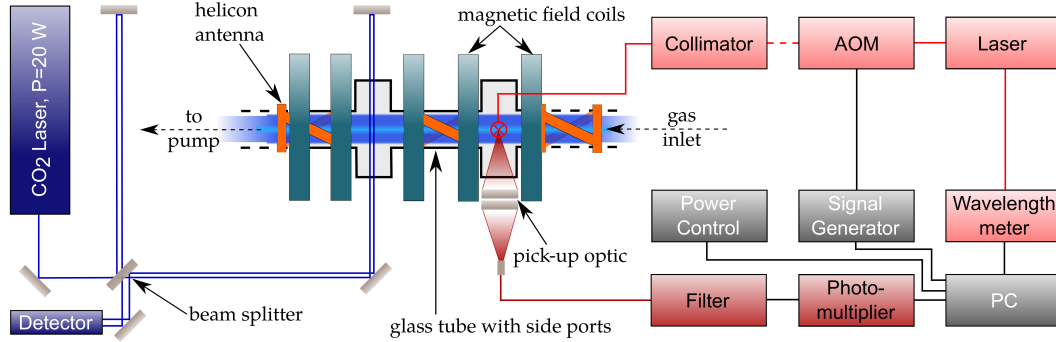
Figure 5.1: Schematic drawing of the experimental setup of PROMETHEUS-A. Neutral gas inside of the glass tube, with three ports in total for diagnostics, is heated by deposited power over three helical antennas. The magnetic field is provided by five water-cooled copper coils. At the right end gas is continuously injected and at the opposite site pumped out. A laser interferometer (left) and a laser-induced fluorescence diagnostic (right) are mounted at two different radial ports.

axial distance of 230 mm for diagnostic purposes. The axial magnetic field is provided by four water-cooled copper coils. Coil currents of $I_{\text{coil}} \leq 370$ A create a magnetic field induction up to $B \leq 116$ mT. The axial magnetic field coil placement was calculated to achieve a homogeneous magnetic field by simultaneously providing access to the radial ports.

At one axial end the working gas (here argon) is continuously injected into the tube and pumped at the opposite side. Before starting the discharge, the gas flow is manually adjusted for a constant filling pressure of neutral gas in the interval of $p_0 = 3 - 15$ Pa. No gas flow or pump control are integrated.

For plasma heating three identical half-turn helical copper antennas are equidistantly placed along the glass tube. Each antenna is powered by a RF-generator and manually matched over a capacitive matching unit. Every single RF-generator is able to supply up to $P_{\text{RF}} = 12$ kW. The limiting factor for the maximum total power is the arcing. Without arcing it was possible to couple up to $P_{\text{RF}} \leq 27$ kW into the plasma. To reduce the heat load on the glass tube and helicon antennas, the discharge was operated in a pulsed mode with $f = 10$ Hz with a 10 % duty cycle. This operation mode generates fast ramp-ups in the microsecond scale and is opening the possibility to reproduce the plasma discharge in a short time scale. Two laser diagnostic tools are mounted at two different radial ports of the plasma cell: A 2-pass CO_2 laser interferometer and a laser-induced fluorescence (LIF)

diagnostic. Both diagnostics are described in more detail in section 5.2. The complete plasma cell is mounted on four electric lifting cylinders. That makes it possible to move the plasma cell vertically with respect to both laser diagnostic and radial profiles can be measured. To achieve a preferably homogeneous mag-
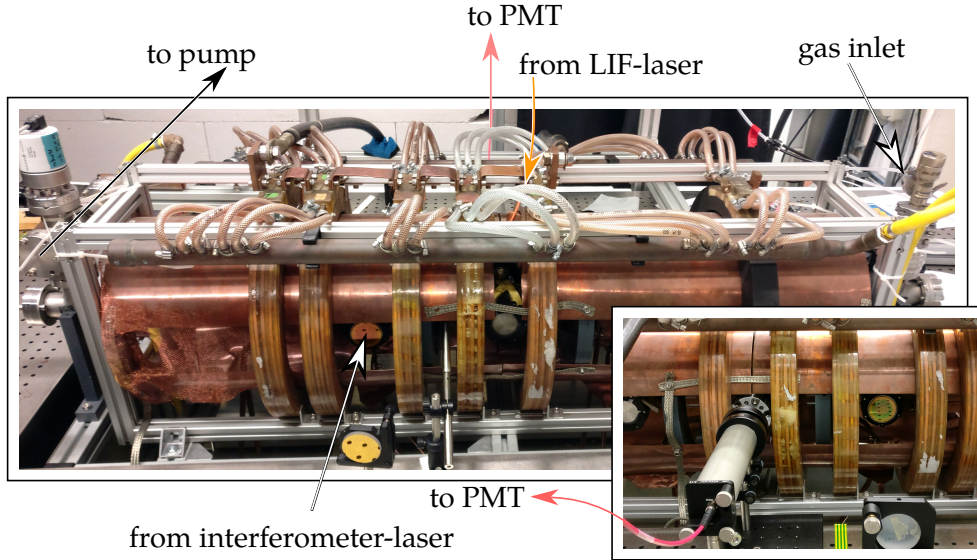

Figure 5.2: The experimental setup of PROMETHEUS-A. At the right end gas is continuously injected and at the opposite site pumped out. A laser interferometer and a laser-induced fluorescence diagnostic are mounted at two different radial ports. The small buttom figure shows the other side of the setup with the mounted pick-up optics for the LIF diagnostic and the mirror at the port of the interferometer to reflect the CO_2 laser.

netic field the optimal axial magnetic field coil placement was calculated. Figure 5.3 shows the axial magnetic induction in the center of the discharge at a maximum coil current of $I_{coil} = 370\,\mathrm{A}$. To illustrate the placement and expansion of PROMETHEUS-A the experimental setup is positioned below the graph. At the radial port for the laser interferometer a magnetic induction up to $B \leq 116\,\mathrm{mT}$ can be reached. At the spot of the LIF diagnostic a magnetic induction up to $B \leq 105\,\mathrm{mT}$ are achievable. All described characteristics are summarized in table 5.1 and important plasma parameters like plasma density n_e and electron temperature T_e are added to give a full overview of PROMETHEUS-A.
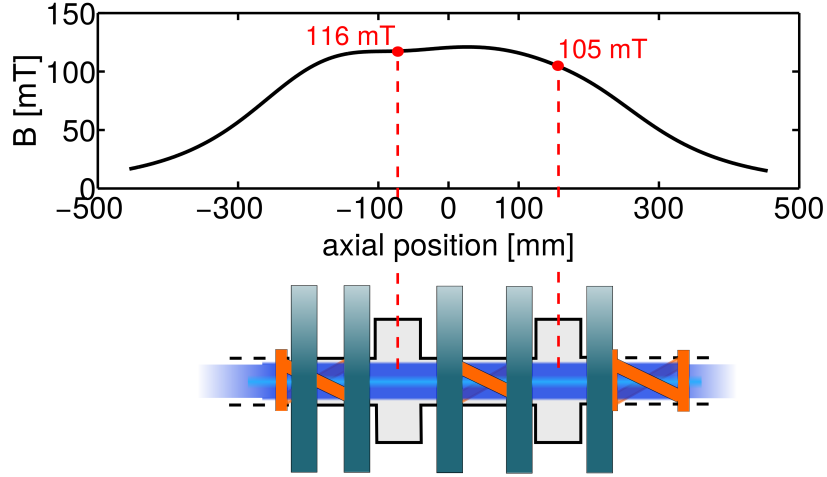
Figure 5.3: Calculations of the axial magnetic field induction in the center of the glass tube for the maximum coil current. Measured values at two ports are shown as red dots. The schematic drawing of the experimental setup is shown below to illustrate the placement and expansion in comparison to the magnetic field induction.

parameter	value
working gas	argon
tube length	$l = 1\,\mathrm{m}$
tube radius	$r = 22\,\mathrm{mm}$
RF power	$P_{\mathrm{RF}} \leq 27\,\mathrm{kW}$
magnetic field induction	$B \leq 116\,\mathrm{mT}$
neutral gas pressure	$p_0 = 3 - 15\,\mathrm{Pa}$
plasma density	$n_{\mathrm{e}} \leq 7 \cdot 10^{20}\,\mathrm{m^{-3}}$
electron temperature	$1.3\,\mathrm{eV} \leq T_{\mathrm{e}} \leq 1.9\,\mathrm{eV}$
diagnostic	LIF with diode laser, $P_{\mathrm{dl}} \leq 0.5\,\mathrm{W}$
	interferometer with CO_2 laser, $P_{\mathrm{CO_2}} \leq 20\,\mathrm{W}$

Table 5.1: Characteristics and parameters of PROMETHEUS-A.

5.2 Plasma diagnostics and numerical methods

Two laser diagnostics are mounted at two different radial ports of the plasma cell as described in section 5.1.1 and schematically shown in figure 5.1. A 2-pass CO_2 laser interferometer and a laser-induced fluorescence (LIF) diagnostic [Freegarde, 1997][Severn et al., 1998] are used to measure radial profiles of plasma parameters, like neutral atom or ion temperatures, drift velocities or the plasma density [Hardin et al., 2004]. In this section, the diagnostics are described in more detail and the data evaluation is described. In addition, the principle line ratio measurement is described to calculate the electron temperature with the help of the reaction rate model (see chapter 4.1).

5.2.1 Laser interferometer
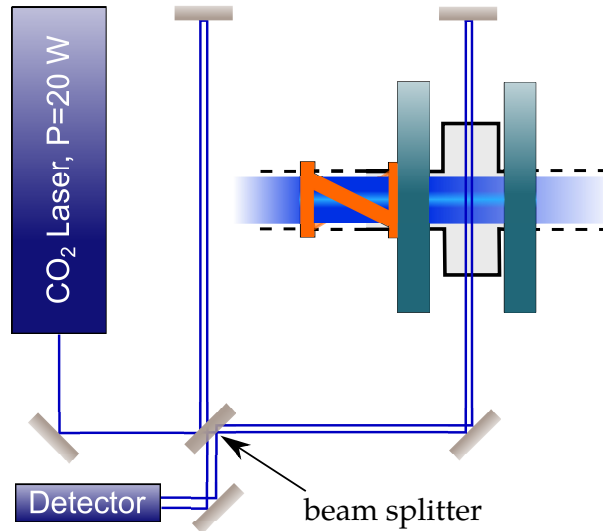
Figure 5.4: Schematic setup of the laser interferometer at PROMETHEUS-A. The beam of the CO_2 laser is splitted into two legs. One outside of the experiment and one through the plasma. Both are reflected back and superimposed at the beam splitter, resulting in an interference pattern with a varying intensity depending on the plasma density measured with a laser power meter.

One main diagnostic tool is a 2-pass CO_2 laser interferometer with a wavelength of $\lambda = 10.6\,\mu m$. The interferometer measures the line-integrated plasma density at one axial location in between two helicon antennas. By moving the cell up and down (see section 5.1.1) and assuming a cylindrical symmetry of the discharge,
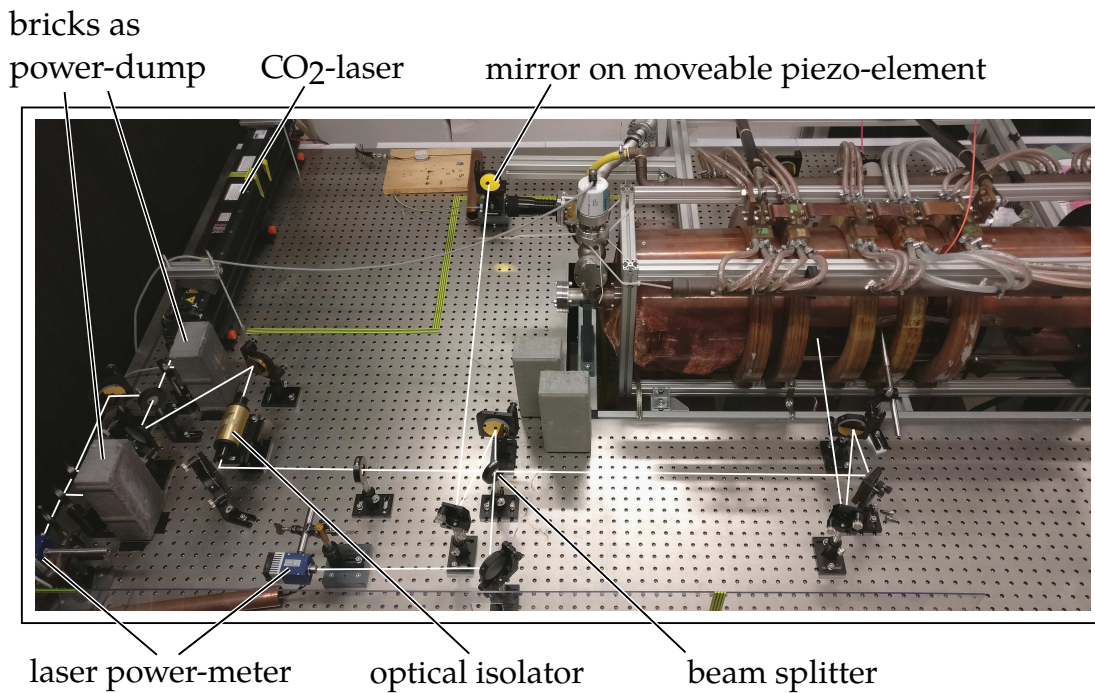
bricks as
power-dump   CO$_2$-laser   mirror on moveable piezo-element

laser power-meter   optical isolator   beam splitter

Figure 5.5: Experimental setup of the laser interferometer with beam paths shown in white. The beam power of the CO$_2$ laser is first reduced by dumping a fraction of it into beam dumps (bricks) and measured by a power meter. The diagnostic leg of the beam is transferred through an optical isolator to prevent the coupling of back scattered light into the laser system. The beam is then splitted into two legs, one reference beam outside of the experiment and one beam through the plasma. Both are reflected back and superimposed at the beam splitter, resulting in an interference pattern with a varying intensity depending on the plasma density measured with a laser power meter.

one derives the radial local plasma density distribution at the location of the interferometer measurement via inversion techniques. The schematic setup is depicted in figure 5.4 and a picture of the experimental setup is shown in figure 5.5. The single incoming laser beam of coherent light from the CO_2 laser is split into two identical beams by a beam splitter. Each of these beams travels a different path, either outside of the plasma cell or inside the plasma cell by going through a diagnostic port. Both are reflected back the same path and superimposed by the beam splitter before arriving at the detector. Depending on the respective medium, electromagnetic waves are refracted and spread with different velocities. The phase velocity v_{ph} in a medium correlates to the speed of light c. The relation of both quantities gives the refractive index

$$N = \frac{c}{v_{ph}} = \frac{kc}{\omega}. \tag{5.1}$$

The dielectric properties of the plasma define the refractive index that is dependent on plasma frequency $f_p = \sqrt{(e^2 n_e / \epsilon_0 m_e)}/2\pi$ and thus on plasma density n_e as [Hartfuss et al., 1997]

$$N = \sqrt{1 - \frac{f_p^2}{f^2}} = \sqrt{1 - \frac{n_e}{n_c}}, \tag{5.2}$$

where f is the laser frequency and $n_c = 4\pi^2 f_p^2 m_e \epsilon_0 / e^2$ is the cut-off density, defining the frequency where an incoming wave oscillates with the plasma frequency and is unable to propagate in the plasma and gets fully reflected. In PROMETHEUS-A the plasma densities are $n_e \leq 7 \cdot 10^{20}\,\mathrm{m^{-3}}$ (5.1). This corresponds to plasma frequencies of $f_p \leq 250\,\mathrm{GHz}$. The CO_2 laser has a frequency of $f = 30\,\mathrm{THz}$ which is much higher than the expected plasma frequencies. By travelling through the active plasma discharge over a length of l the laser beam experiences a phase shift of

$$\Delta\varphi = \frac{2\pi}{\lambda} \int_0^l 1 - \sqrt{1 - \frac{n_e(z)}{n_c}} \mathrm{d}z \tag{5.3}$$

in the plasma leg of the interferometer. Since the laser frequency is much bigger than the plasma frequency, respectively the plasma density is far below the critical density, the square root in (5.3) can be expanded and the integral is simplified to

a direct proportionality of the phase shift and the integral of the plasma density

$$\Delta\varphi \approx \frac{\pi}{\lambda n_{\mathrm{c}}} \int_0^l n_{\mathrm{e}}(z)\mathrm{d}z. \tag{5.4}$$

Depending on the plasma density the refractive index of the plasma changes and consequently the phase shift changes from low to high plasma densities. The phase difference creates an intensity variation when the two beams are superimposed: two beams with equal amplitude and frequency, one unaffected, $S_1 = A \cdot \sin(\omega t)$, and the other one phase shifted, $S_2 = A \cdot \sin(\omega t + \varphi)$, result in

$$\begin{aligned} S &= S_1 + S_2 \\ &= A \cdot \sin(\omega t) + A \cdot \sin(\omega t + \varphi) \\ &= 2A \cdot \cos\left(\frac{\varphi}{2}\right)\sin\left(\omega t + \frac{\varphi}{2}\right). \end{aligned} \tag{5.5}$$

It is measured by the intensity variation of the laser beam at the end with an optical detector. The plasma density can be evaluated by using (5.4).

5.2.1.1 Abel inversion

As outlined above the CO_2 laser interferometer measures the line-integrated plasma density. By measuring the full radial plasma density profile, one can calculate the radial profile of the plasma density distribution for comparison with model calculations and LIF measurements. The assumption that the shape of the radial plasma density profile is not varying over a wide range of operational parameters is used in the approach. A parabolic or Gaussian-like shape is assumed for various heating RF powers and magnetic inductions. With this assumption the measured line-integrated plasma densities are inverted in order to obtain radial plasma density profiles. It is done using Abel-inversion of the line-integrated plasma densities [Abel, 1826]. The measured intensity $I(x)$ is described by the Abel transform, as also described by Smith et al. [1988c] or Pretzler et al. [1992]

$$I(x) = 2 \int_x^\infty \frac{r\epsilon(r)}{\sqrt{r^2 - x^2}}\mathrm{d}r, \tag{5.6}$$

with $\epsilon(r)$ as emission coefficients, x as the displacement of the plasma density profile and r as the radial distance to the source. $\epsilon(r)$ can also be defined as a radial slice of the two-dimensional circular symmetric function on which the

measured one-dimensional intensity $I(x)$ is projected. The inverse Abel transform is then given by

$$\epsilon(r) = -\frac{1}{\pi} \int_r^\infty \frac{\mathrm{d}I/\mathrm{d}x}{\sqrt{x^2 - r^2}} \mathrm{d}x. \tag{5.7}$$

A complication in the application of the method is owing to the enhancement of noise in the data by the derivative of the projection. The intensity is usually not obtained as a continuous function but as discrete points. To handle these problems several numerical approaches have been made in the last decades for example by Nestor [1960] or Bockasten [1961b] by a prior smoothing of the data. Current numerical approaches done by Singh et al. [2010] or De Micheli [2017] compute Legendre coefficients of the inverse Abel transform employing a Fourier transform. Thus, the algorithm is also applicable for the inversion of Abel integral data of noisy measurements.

5.2.2 Laser-induced fluorescence

The second laser diagnostic used in the experiment is the laser-induced fluorescence (LIF) method. It is a non-invasive tool for local measurements of metastable particle densities, drifts and temperatures [Chakraborty et al., 2012] [Scime et al., 1998].

The diode laser system, described in more detail in section 5.2.2.1, produces wavelength-stable laser light with a linewidth of $\sigma_\lambda < 1 \cdot 10^{-6}$ nm over a tuning range of more than $\Delta\lambda = 60$ pm with tuning steps of $\delta\lambda = 0.1$ pm. It opens the possibility to choose different wavelengths, to measure not only the neutral argon metastable fluorescence signal with an exciting laser wavelength of $\lambda_{\mathrm{ArI}} = 667.91$ nm [Boivin, 2003], but also the metastable fluorescence signal of the single ion argon atoms with a laser wavelength of $\lambda_{\mathrm{ArII}} = 668.43$ nm [Stark et al., 2006][Scime et al., 2005], see also figure 5.6. The energy in one photon at these wavelengths equals precisely the energy gap between the lower (initial) and upper (excited) atomic state. The laser light from the continuous wave (cw) diode laser system is chopped by an acousto-optic modulator (AOM) with $f_{\mathrm{AOM}} = 500$ kHz to discriminate the background noise from the fluorescence signal. This sets also a principal technical limit for the highest reachable time resolution. The chopped laser light is transferred via an optical fiber to the PROMETHEUS-A experiment (see figure 5.2), coupled into the glass tube, focussed to a spot of $1 - 2$ mm diameter and absorbed by the metastable argon
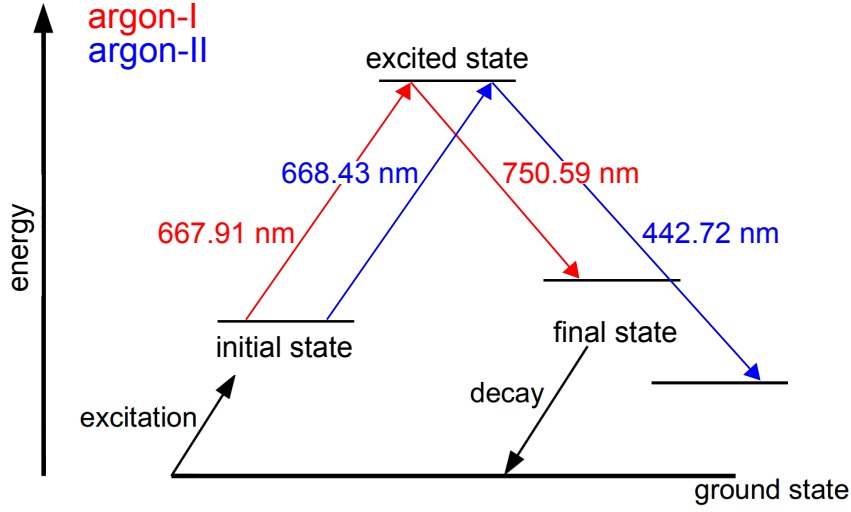
Figure 5.6: Atomic states of argon used for the LIF measurements. The initial metastable states (see table 5.2 for details) are populated by collisions with electrons or background gas and subsequently stimulated to the excited state by incoming laser radiation. By emitting radiation of a specific wavelength, the fluorescence signal, the excited state is immediately decaying to a final state and further to the ground state. The shown scheme is divided into neutral argon LIF (red) and ion argon LIF (blue) with labeling of the respective wavelengths.

atoms at the spot. By absorbing the laser light, the metastable state of argon is excited to a higher energetic atomic quasi-metastable state. The mean half-life period of quasi-metastable states is in the order of ns, which means that they nearly instantaneously decay to a lower, more advantageous energetic state by emitting fluorescent light with a wavelength inversely proportional to the energy gap between these two atomic energy levels. The line shape of the fluorescent light is measured by scanning the laser over a narrow frequency band that covers the absorption line and measuring the intensity of the emitted fluorescent light. Several broadening mechanisms determine the line shape of these fluorescence lines [Sobel'man et al., 1995]. One is the natural line broadening by transitions between bound atomic states. The broadening comes from the uncertainty principle of the transitioning electrons and results in a Lorentzian line shape. Other mechanisms are the Van-der-Waals broadening by collisions with neutrals, resonance broadening and Stark broadening due to splitting of atomic states in a prevalent electric field which is especially important in highly ionized high density plasmas [Goeckner, 1989][Roston, 2012]. All these mechanisms are neglectable in our plasma environment. For neutral/ion temperatures greater than $T_\mathrm{i} = 0.02\,\mathrm{eV}$

and a magnetic induction less than $B = 120\,\mathrm{mT}$ the effect of Doppler broadening dominates the line shape [Keesee et al., 2004][Keesee, 2007]. The frequency of light, emitted from the moving neutrals or ions, is seen shifted by an observer. The frequency shift with respect to the natural line frequency is proportional to the velocity of the emitting atom, $\Delta f = f \cdot v/c$. This allows a direct correlation between the shape of the fluorescent light signal from the laser scan and the neutral/ion velocity distribution function. But additionally the magnetic induction
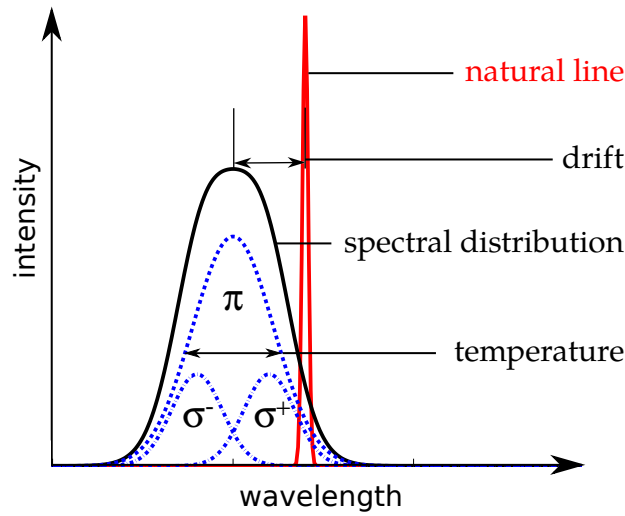
Figure 5.7: Schematic drawing of the measured spectral distribution (black), broadened by different mechanisms, compared to the natural spectral line (red). The distributions plotted with the blue dotted line are the Zeeman splitted components of the measured distribution. They consist of one spectral π-line and two σ-lines with opposing polarizations. The temperature of the measured metastable states are calculated over the width of the spectral lines, the metastable density over the integral of the spectral distribution and the drift by the offset of the peak of the distribution to the peak of the natural line.

in the order of $B = 100\,\mathrm{mT}$ causes a non-neglectable energetic Zeeman splitting of the atomic states into different energetic states. More precisely, the magnetic field couples with the momentum of the atomic states and causes a splitting of spectral lines [Haken, 1987]. These splitted states are populated and pumped by the laser (see figure 5.7 for details). The energy difference of two levels of

transition is given by [Stark, 2006]

$$\Delta E = \frac{eh}{4\pi m_{\mathrm{e}}} B_0 \Delta(g_{1,2} M_{1,2}), \tag{5.8}$$

with $g_{1,2}$ as the Landé factors and $M_{1,2}$ as the magnetic quantum numbers of the respective upper or lower level. The Landé factor is different for each energy level and, according to the selection rules, $\Delta M_{1,2}$ can have values 0 or ± 1. Transitions with $\Delta M_{1,2} = 0$ are the so-called π components and those with $\Delta M_{1,2} = \pm 1$ are σ components. The two σ-lines are polarized perpendicular to the magnetic field and the π-line is polarized parallel to the magnetic field. Transitions between the splitted energy levels lead in superposition to an effective Zeeman broadening. That broadening mechanism has also been taken into account in our model.
Due to the polarization of the distinct spectral lines, measurements parallel to the magnetic field lead to an observation of only the two σ-lines (see figure 5.8a) and with an excitation perpendicular to the magnetic field the π-line and σ-lines are visible (see figure 5.8b). The atomic metastable states of argon to measure char-
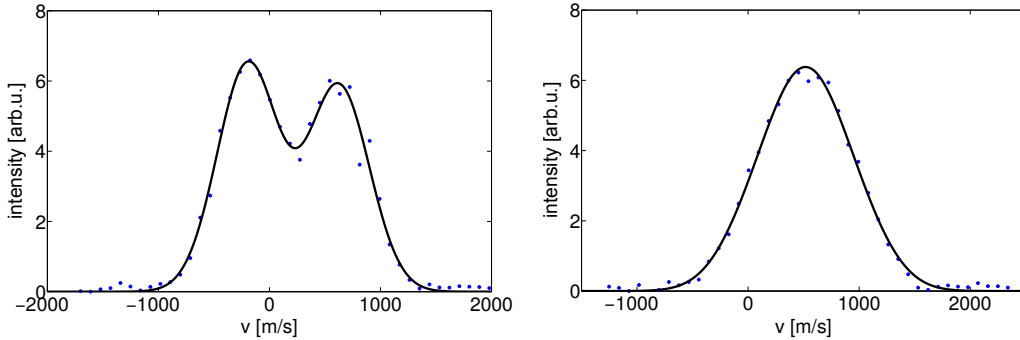
(a) Neutral LIF velocity distribution parallel to the magnetic field at $B = 50\,\mathrm{mT}$ and $P_{\mathrm{RF}} = 0.9\,\mathrm{kW}$. Measured points in blue and fit with two Gaussians in black.

(b) Neutral LIF velocity distribution perpendicular to the magnetic field at $B = 50\,\mathrm{mT}$ and $P_{\mathrm{RF}} = 3\,\mathrm{kW}$. Measured points in blue and fit with three Gaussians in black.

Figure 5.8: Comparison of typical measured neutral LIF velocity distributions parallel (a) and perpendicular (b) to the magnetic field. Due to different experimental parameters both measurements are not comparable in intensity and mean velocity.

	configuration	term	J	energy [eV]
neutral metastables				
initial state	$3s^2 3p^5(^2\mathrm{P}^0_{3/2})4s$	$^2[3/2]^0$	1	11.624
excited state	$3s^2 3p^5(^2\mathrm{P}^0_{1/2})4p$	$^2[1/2]$	0	13.480
final state	$3s^2 3p^5(^2\mathrm{P}^0_{1/2})4s$	$^2[1/2]^0$	1	11.828
ion metastables				
initial state	$3s^2 3p^4(^3\mathrm{P})3d$	$^4\mathrm{F}$	7/2	33.455
excited state	$3s^2 3p^4(^3\mathrm{P})4p$	$^4\mathrm{D}_0$	5/2	35.309
final state	$3s^2 3p^4(^3\mathrm{P})4s$	$^4\mathrm{P}$	3/2	32.509

Table 5.2: Characteristics of the atomic states used for the neutral and ion LIF in PROMETHEUS-A.

acteristics of metastable neutrals or ions in the experimental setup are compiled in table 5.2 and depicted in figure 5.6. The population of these metastable states is mostly dependent on neutral gas pressure, electron temperature and plasma density.

Another issue in using laser-induced fluorescence as a plasma diagnostic is the saturation broadening. Ideally, the Doppler-broadened line shape represents the ion velocity distribution function. But at high laser powers, the saturation of the optical transition leads to an additional line broadening [Goeckner, 1989] [Goeckner et al., 1993]. To exclude this broadening mechanism, measurements of the intensity of the fluorescence signal for increasing laser power were performed (see figure 5.9) to compare theory and experimental data. Since the measurements show a linear dependence and no saturation of the fluorescence signal, one can conclude that the present laser power does not lead to broadening effects. The fluorescent light with wavelengths of $\lambda_{\mathrm{f,ArI}} = 750.59\,\mathrm{nm}$ or $\lambda_{\mathrm{f,ArII}} = 442.72\,\mathrm{nm}$ for the neutral or ion LIF measurements, respectively, is collimated into a multimode fiber and converted into an electrical signal by optical narrow 1 nm bandpass filters, centered at the desired fluorescence line, photo multiplier tubes (PMT) and current-to-voltage converters (figure 5.1).

The biggest challenge in LIF measurements is to collect the LIF signal from high photon noise background resulting from spontaneous emissions. For that a lock-in amplifier is used. This technique generates the amplitude of the LIF signal directly and is routinely used for metastable temperature measurements. But to achieve LIF measurements with high time resolution [Palomares et al., 2013] [Stark et al., 2006] and to have the raw PMT signals for the line intensity ratio calculations (section 5.2.5), a digitizer board is used to sample the PMT sig-
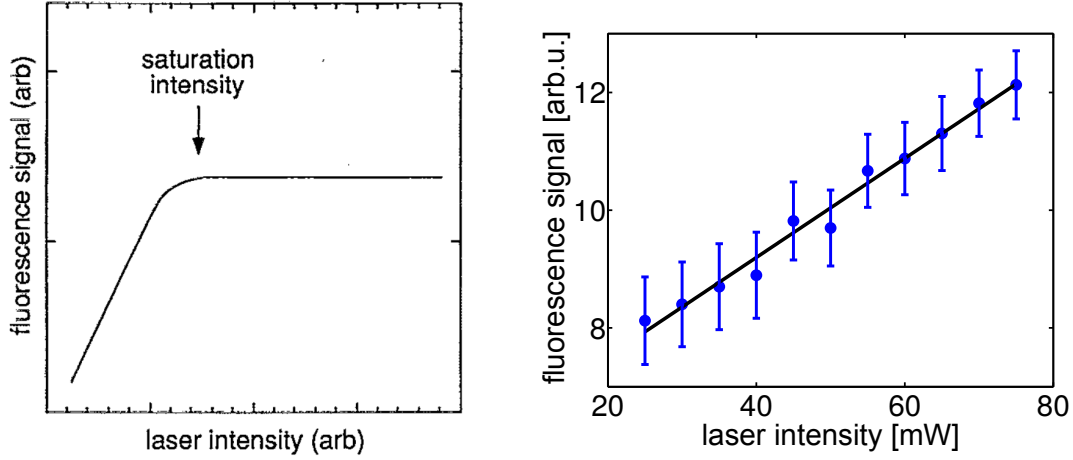
(a) Strength of the fluorescence signal as a function of laser intensity. The sketch (for a single laser frequency) illustrates how LIF is a non-linear process at high intensities. Figure taken from [Goeckner et al., 1993].

(b) Measured fluorescence intensity of neutral argon as a function of laser intensity for a single laser frequency done at $p_0 = 5\,\text{Pa}$, $B = 60\,\text{mT}$ and $P_{\text{RF}} = 3.3\,\text{kW}$.

Figure 5.9: Comparison of a typical saturation broadening dependency and experimental data from neutral LIF in PROMETHEUS-A.

nal output with a sampling frequency of $f_\text{s} = 5\,\text{MHz}$. The disadvantage of the method is that a large amount of data has to be stored and the off-line spectral analysis to extract the LIF signal is very time consuming. After processing the raw data from the PMTs (see section 5.2.3) a spectral (velocity) distribution is obtained as shown in figure 5.7. Due to Zeeman-splitting and Doppler broadening the velocity distribution function is a superposition of three Gaussians and is fitted accordingly.

From these fitting results characteristics of the measured neutral argon or argon ion metastable states are calculated. The temperature is calculated from the width of a spectral component of the Zeeman splitted distribution as

$$T_\text{g} = \frac{\delta_D^2 m_{\text{Ar}} c^2}{2k_\text{B}}, \tag{5.9}$$

with δ_D as width of the spectral distribution

$$I_\text{D}(\lambda) = \mathrm{e}^{-\left(\frac{\Delta\lambda}{\delta_\text{D}}\right)^2}. \tag{5.10}$$

The particle drift is calculated from the Doppler shift between the location of the natural line and the measured peak in the center of the spectral distribution as

$$v_{\mathrm{drift}} = c \left(\frac{\lambda_{\mathrm{peak}} - \lambda_{\mathrm{nat}}}{\lambda_{\mathrm{nat}}} \right),$$ (5.11)

with λ_{peak} representing the wavelength where the peak of the spectral distribution is located and λ_{nat} as the wavelength of the natural fluorescence line. The relative density of the respective metastable states are determined by the integral over the total measured spectral distribution

$$n_{\mathrm{Ar}} = \int_{-\infty}^{\infty} I_{\mathrm{D}}(\lambda) \mathrm{d}\lambda.$$ (5.12)

5.2.2.1   The Diode laser system

The diode laser system is a modular setup well suited for the laboratory as well as for industrial measurement applications: the LION external cavity semiconductor laser system manufactured by Sacher Lasertechnik GmbH. It is a tapered amplifier system build to amplify tunable cw light sources. It consists of electronic control units connected to the external laser head to precisely regulate the laser current, the optical output power and the temperature of the laser diode to reach a maximum mechanical and optical stability at a laser output power of more than $500\,\mathrm{mW}$.
Figure 5.10 shows the interior of the master-slave configuration, consisting of a tunable external cavity in Littman configuration (upper right) and the tapered amplifier system (lower left). The master diode produces a relatively broad spectrum around the desired wavelength. It is a commercial laser diode where one facet is antireflection coated to suppress the reflectivity below 10^{-4} and to maximize the output power. The beam of the master diode passes a diffraction grating to select the desired wavelength. Gratings make use of the wave properties of light by making sections of a wavefront travel extra distances as it is reflected off a non-uniform surface. The wavefront propagating from one groove and the wavefront propagating from another groove will only constructively interfere if the difference in the lengths of the light paths is an integer number of the lights wavelength.

optical isolator   master diode

reflecting mesh   fiber coupler

amplifier diode   beam splitter

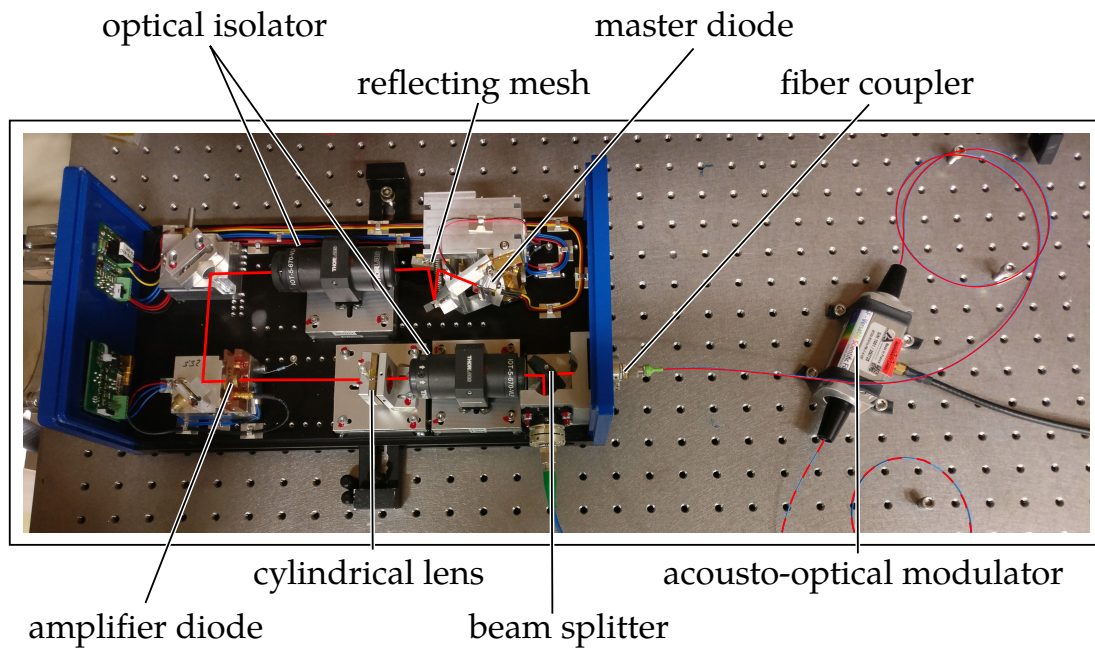cylindrical lens   acousto-optical modulator

Figure 5.10:   Diode laser system for laser-induced fluorescence measurements on PROMETHEUS-A. The light of the master diode hits a diffraction grating to select the desired wavelength. After passing an optical isolator, to prevent damages by high power reflections, the spectral narrow light is coupled via two mirrors into the amplifier system to boost the laser power with up to a factor of 100. The cylindrical lens refracts the beam into a more Gaussian-like shape. Past another optical isolator the beam is now splitted for wavelength detection purposes and the high power beam is coupled into a fiber, transferred through an AOM and finally coupled into the experiment.

In general the so-called grating equation, defining the dependence of the reflected wavelength and the angle of diffraction, can be written as

$$n\lambda = d(\sin\theta + \sin\theta'), \qquad\qquad (5.13)$$

where n is the order of diffraction, λ is the diffracted wavelength, d is the grating constant (the distance between grooves), θ is the angle of incidence measured from the grating normal, and θ' is the angle of diffraction measured from the grating normal (figure 5.11). The first diffraction order of the incident master diode beam
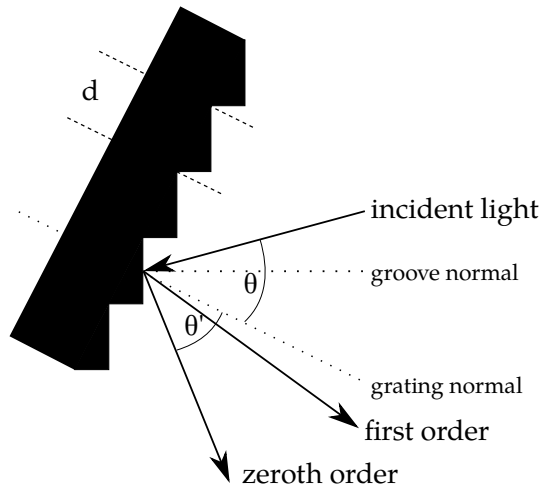
Figure 5.11: Schematic drawing of a diffraction grating with grating constant d, angle of incidence θ and angle of diffraction θ' both measured from the grating normal.

is reflected back into the diode via a reflection prism. Only a small fraction of the beam power is coupled out via the 0th diffraction order of the grating and exits the cavity. The back reflection forces the master laser to oscillate in one single longitudinal mode at a defined wavelength. By simultaneously translating and rotating the grating the wavelength can be tuned. This is done with the help of a piezo actuator mounted at the grating arm. The spectrally narrow light of the master laser diode is coupled via two mirrors into the amplifier system. The optical isolator in front of the first mirror prevents reflections back into the master laser to avoid damages to the master diode. For an optimal operation of the system, both laser beams, before and after the two mirrors, must be aligned in a collinear way. To achieve this, the two mirrors can be tilted in two dimensions by two micrometer screws each. Hereafter the beam enters the amplifying diode. The amplifier diode is a high power laser diode where both facets are coated with antireflection material. By stimulated emission of the diode and trapping of the

coherent light in an optical resonator (an arrangement of mirrors that forms a standing wave cavity resonator) the laser beam gets amplified by a faktor of up to 100. Past amplification, the beam passes a cylindrical lens to bring the beam into a more Gaussian-like shape. After another optical isolator, the beam is splitted with a fraction of $1 : 50$ for wavelength detection purposes and the high power beam is coupled into a polarization maintaining single-mode fiber, transferred through the AOM and finally coupled into the experiment.

5.2.2.2   The acousto-optic modulator

The acousto-optic modulator (AOM) is a device to control the power, frequency or spatial direction of an incident laser beam with the help of an electrical drive signal. AOMs have a large variety in possible applications [Gooch, 2018] [Vivek, 1999]. They are for example used for Q-switching of solid-state lasers, where the AOM serves to block the laser resonator before the pulse is generated. AOMs are also used for cavity dumping of solid-state lasers, to generate either nanosecond or ultrashort pulses, as a pulse picker to reduce the pulse repetition rate of a pulse train or in laser printers for modulating the power of a laser beam [RP-Photonics GmbH, 2018]. The functionality of an AOM is based on the acousto-optic effect, i.e. the modification of the refractive index by the oscillating mechanical pressure of a travelling sound wave.

Thus, the key element of an AOM is a transparent crystal (or a piece of glass) through which the incident light propagates. When a light beam passes a transparent material in which traveling acoustic waves are present (figure 5.13), the acousto-optic effect occurs. By treating the modulation as a photon-phonon scattering process the main features can be described by the energy-momentum relations [Donley et al., 2005]

$$k_\mathrm{d} = k_\mathrm{i} + \kappa \ \ \mathrm{and} \ \ \omega_\mathrm{d} = \omega_\mathrm{i} + \Omega, \tag{5.14}$$

with k_d and k_i as diffracted or incident photon wave vector, respectively, κ as phonon wave vector in the respective optical or acoustic field, ω as incident light frequency and Ω as the RF modulation frequency. If photons and phonons are part of a scattering process this will result in the absorption of acoustic phonons. Figure 5.12 underlines the mechanism as a momentum conservation diagram that
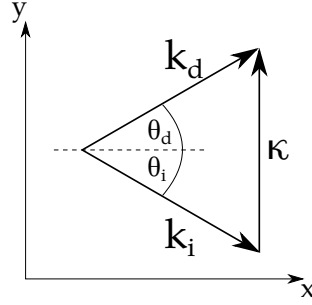
Figure 5.12: Momentum conservation diagrams for the absorption of a phonon. The case represents a configuration for the incident and diffracted light beams where the conditions are Bragg matched for a given orientation of the phonon momentum. For clarity: κ, and thus θ_i and θ_d, are made large. Normally the Bragg angle is $< 1°$ and the phonon momentum is roughly two orders of magnitude smaller than the photon momentum.

describes the scattering event and Bragg's law is visible as

$$\sin\theta_B = \frac{\kappa}{2 \cdot k_i},\tag{5.15}$$

where θ_B is the Bragg angle, and $\theta_i = \theta_d = \theta_B$. The acoustic waves are generated by a piezoelectric transducer attached to the material and driven by a RF signal with a frequency in the range of $f_{RF} = 200\,\text{MHz}$ (table 5.3) and yield periodic density variations. The compressions and rarefactions of the acoustic wave, traveling at sound speed v_s with the frequency f_{RF}, result in changes in the index of refraction in the medium. The refractive index is thus modulated with a wavelength of $\Lambda = 2\pi \cdot v_s/f_{RF}$ (figure 5.13). With (5.15), the latter equation and $k = \omega_L/v_L$ and $\kappa = \Omega/v_s$ with v_L as speed of light and v_s as the speed of sound in the medium one obtains the known and familiar Bragg's law as

$$\sin\theta_B = \frac{\lambda_L}{2 \cdot \Lambda},\tag{5.16}$$

which is also schematically shown in figure 5.13. Light is Bragg diffracted by the traveling periodic refractive index modulation (AOMs are also called Bragg cells). The frequency of the scattered outgoing beam is increased or decreased by the frequency of the sound wave and is scattered in a slightly different direction, due to the fact that the wavenumber of the sound wave is small compared to that of the light beam. The shift of the frequency depends on the propagation direction of the beam relative to the acoustic wave. The frequency of the sound wave controls the frequency shift and the direction of the scattered beam, whereas the
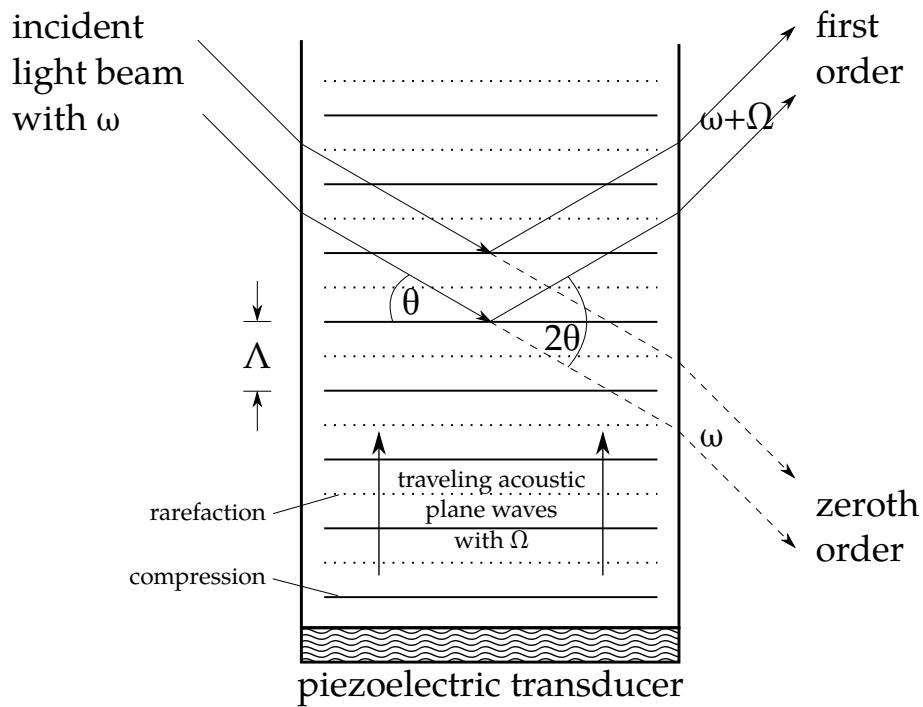
Figure 5.13: Schematic drawing of an aligned AOM. The AOM-mode is shown where the light is diffracted into the +first order and the laser frequency is up-shifted by the RF modulation frequency Ω. Phonons are absorbed in this configuration, and thus, momentum is transferred to the laser beam as shown in figure 5.12. The AOM crystal can also be aligned for the -first diffraction order, but that case is not shown here. In that case, corresponding to a phonon emission process, the diffracted laser frequency would be down-shifted by Ω. The refraction of light at the air-glass boundary is also shown. Note that the external Bragg angle is larger than the internal Bragg angle due to the refraction process at the crystal surface.

parameter	value
driving frequency	$f_{RF} = 200\,MHz$
material	TeO_2
speed of sound	$v_s = 4200\,m/s$
refraction index	$n_{TeO_2} = 2.26@633\,nm$
optical power handling	$P_{max} = 400\,mW\,cw$
rise and fall time	$\tau = < 3\,ns$
extinction ratio	$P_{on}/P_{off} > 50\,dB$
insertion loss	$< 3\,dB$
modulation control	analog or TTL

Table 5.3: Characteristics and parameters of the AOM by AA Opto-Electronics (Model MT200-R18-Fio-PM-J1-A-VSF).

optical power can be adjusted by the acoustic power.

Most of the incident light on the acousto-optic modulator can be diffracted by acoustic waves. Under optimal conditions, diffraction efficiencies of nearly $85 - 90\,\%$ can be achieved. By switching the acoustic driver on and off, the acousto-optic modulator acts as a rapid light deflector, as used in this work. The switching of the incident light beam to the first order diffracted beam can occur in a short period of time as shown in table 5.3.

5.2.3 Signal processing

The PMT data gathered from the LIF measurements need careful data analysis to select the desired information from the noise background. The problem of noise in these measurements is widely known and so well established data processing techniques are available. On the one hand side one can use a lock-in amplifier for detection. This technique generates the amplitude of the LIF signal directly and is routinely used for metastable temperature measurements. In this work the lock-in amplifier is used to check if the LIF signal is detectable beforehand. To achieve a high time-resolved LIF measurements, another technique is applied: Two signals are taken into account, one containing the measured data and the other one a periodic reference signal from the AOM. The first contains the amplitude information, the second is used to calculate the phase between both signals at the frequency of the reference signal. How this technique works in detail is explained in the following section.

5.2.3.1 Cross power spectral density

The power distribution over different frequencies is an important quantity of fluctuating signals. A widely used method is the concept of the power spectral density (PSD) estimation [Vaseghi, 2000]. One obtains the power distribution of a signal over a certain frequency range. The PSD of a signal $x(t)$ is defined in Parseval's theoreme as the Fourier transform of the autocorrelation function $r_{xx}(\tau)$

$$P_{xx}(\omega) = \int_{-\infty}^{\infty} r_{xx}(\tau)\mathrm{e}^{-i\omega\tau}\mathrm{d}\tau = F_x(\omega)F_x^*(\omega), \qquad (5.17)$$

where P_{xx} is the PSD, $F_x(\omega)$ is the Fourier transform of the signal's time series and $F_x^*(\omega)$ its complex-conjugate. The PSD is calculated from the PMT output signal, which yields the LIF amplitude as the spectral intensity at the chosen chopper frequency. In the case of a non-stationary LIF signal, time resolution can be realized by the use of a short time Fourier transform (STFT) [Vaseghi, 2000], but on the expense of statistical confidence.

For time resolved LIF data we define the cross spectral density (CSD) similar to the PSD but now with two signals $x(t)$ and $y(t)$ as

$$P_{xy}(\omega) = F_x(\omega)F_y^*(\omega). \qquad (5.18)$$

Here, $F(\omega)$ and $F^*(\omega)$ are the Fourier transforms and their complex-conjugate of $x(t)$ and $y(t)$ respectively. The CSD is a complex valued quantity. From $P_{xy}(\omega)$ the amplitude $A(\omega)$ and the phase spectrum $\Theta(\omega)$ is obtained as [Stark, 2006]

$$A(\omega) = |P_{xy}(\omega)| \quad \text{and} \quad \Theta(\omega) = \arctan\frac{\mathrm{Im}P_{xy}(\omega)}{\mathrm{Re}P_{xy}(\omega)}. \qquad (5.19)$$

The CSD is used for time-resolved LIF measurements (see section 5.2.3.2) with the raw PMT data and the reference signal from the AOM. The method reduces the needed integration time in comparison to the PSD and enables to decrease the minimum time resolution compared to lock-In measurements.

5.2.3.2 Time resolved calculations

For time averaged measurements takes both signals over the full time interval into account and calculate directly the CSD. For time-resolved measurements, windows with a defined width in time are specified for both signals and the CSD is calculated for each time window. The starting point in time of the first window can be set and the CSD is computed. The next step uses the second window with the same width but moved in time with the predefined window step. This procedure is continued until the end of the data stream is reached and for each window the CSD is calculated. An overlap of sequential windows is possible but not required. An illustration of the difference in the time averaged and time-resolved calculation scheme is shown in figure 5.14 for a periodic reference signal.
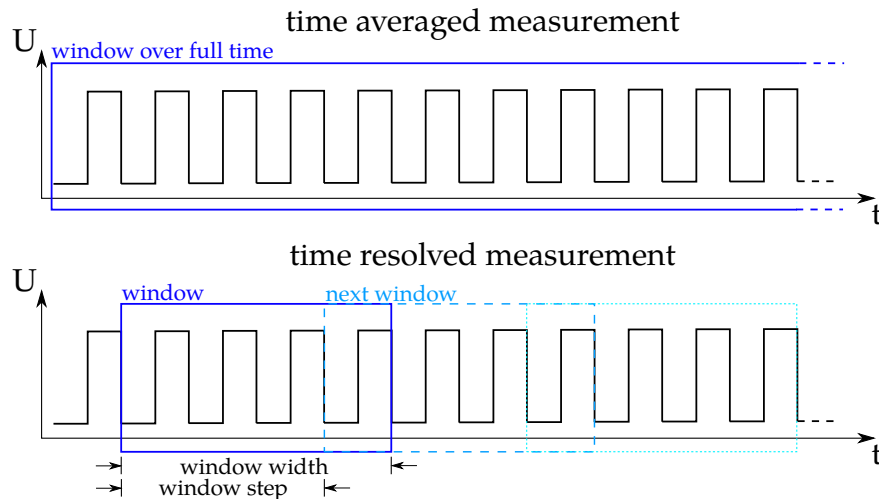
Figure 5.14: Illustration of the difference in the time averaged and time-resolved calculation scheme just for the reference signal. For time averaged measurements the signal over the full time interval is taken to calculate the CSD. For time-resolved measurements windows with a defined width are specified. The starting point of the first window can be set and the CSD is computed. The second window with the same width is now moved in time with the predefined window step. An overlap of sequential windows is possible in this calculations, but not required. This procedure is continued until the end of the data stream is reached and for each window the CSD is calculated.

Since in the LIF measurements the integration time is just a few seconds to get a high signal-to-noise ratio, time averaged measurements can be done quite fast with a few repetitions of the discharge for each wavelength. This is different

for time-resolved measurements. The higher the required time resolution, the smaller the window width and the more repetitions of the discharge have to be recorded. For time resolutions of $\Delta t < 100\,\mu s$, over 100 repetitions of the discharge ($t = 3\,s$) have to be performed, including 15 times a 5 ms discharge. It results in a time consumption of $1 - 2\,h$ for a total time-resolved spectral distribution measurement at just one radial position. It was found that a time resolution of $\Delta t = 200\,\mu s$ is sufficient for the desired LIF measurements, as a compromise between time resolution, signal strength and integration time. Two examples are shown in figure 5.15 for a neutral LIF measurement performed at a filling gas pressure of $p_0 = 5\,Pa$, a magnetic induction of $B = 55\,mT$ and heating powers of $P_{RF} = 1.5\,kW$ for time resolutions of $\Delta t = 250\,\mu s$ (a) and $\Delta t = 50\,\mu s$ (b). Both show a similar evolution of the neutral argon metastable density, but to accomplish a resolution that describes appropriately the time-dependent density also for different experimental parameters, an intermediate time resolution at $\Delta t = 200\,\mu s$ is chosen.
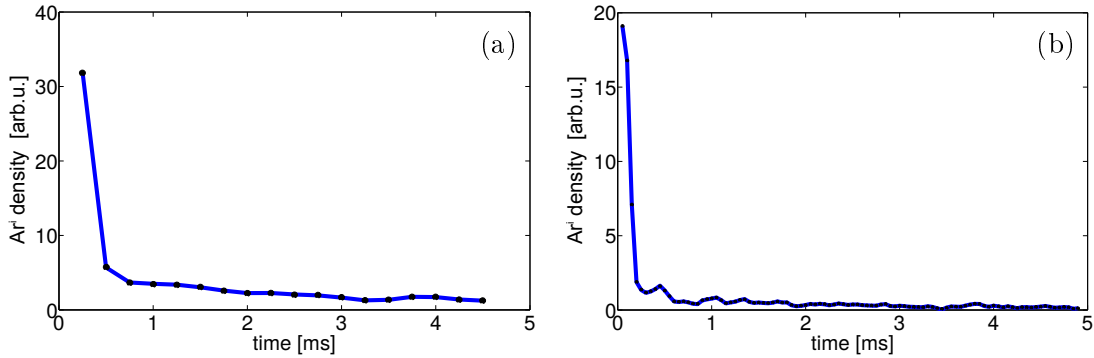
Figure 5.15: Evolution of neutral metastable density for a measurement at a filling gas pressure of $p_0 = 5\,Pa$, a magnetic induction of $B = 55\,mT$ and heating powers of $P_{RF} = 1.5\,kW$ for time resolutions of $\Delta t = 250\,\mu s$ (a) and $\Delta t = 50\,\mu s$ (b). Both show a similar evolution of the neutral argon metastable density, but to accomplish a resolution that describes appropriately the time-dependent density also for different experimental parameters an intermediate time resolution is chosen.

5.2.4 Profile correction function

The complete plasma cell is mounted on four electric lifting cylinders to move the cell vertically with respect to the diagnostics. This possibility was not integrated into the experimental setup when the LIF diagnostic was set up, aligned and adjusted at the optical table. Thus, the chosen lenses for the pick-up optic have the same size as the vacuum flange mounted at the plasma cell (figure 5.2), to maximize the solid angle and the gathered fluorescence signal for the static measurement in the center. After the electric lifting cylinders were installed it became clear that the collected LIF signal depends on the cylinders lift position. Instead of installing a fluorescence signal collector with a much smaller solid angle for all profile measurements, a correction function is introduced. A smaller solid angle would inevitably lead to a reduced signal strength and would therefore increase the needed measurement time by a factor of up to five. The profile correction function is calculated at different radii of the helicon plasma cell. At the port at the opposite site of the pick-up optic a piece of a millimeter scale paper is attached and the output of the diode laser system is guided through the pick-up optics so that the scale is illuminated. The illuminated area represents the scaled spot size at the center of the discharge tube. For each position a picture was taken. Examples for different positions are shown in figure 5.16. To get a comparable correction function between all measured radii the ratio of the number of pixels of the illuminated area and an area of $A = 1\,\mathrm{cm}^2$ of the scaled paper is calculated with a graphic programm. Normalizing these ratios to the value of the central ratio yields a position-dependent function $\Omega(h)$ for profile LIF measurements. For all measured positions the values for the number of pixels, the calculated ratios and correction factors are compiled in table 5.4. Taking the calculated profile correction factors into account, a fit is computed in dependence of the position of the plasma cell. The profile correction function is then

$$\Omega(h[mm]) = 0.0059 \cdot h^2 - 2.2204 \cdot 10^{-16} \cdot h + 1.0185. \tag{5.20}$$

The correction function has to be taken into account for the LIF profile measurements in addition to transmission factors and quantum efficiencies of the neutral and ion fluorescence lines, as calculated in the next section, to have comparable metastable densities. For line ratio measurements the correction function $\Omega(h)$ is obsolet since for both fluorescence signals the correction function has the same value and cancels out.

(a) $h = 14.1\,\mathrm{mm}$ (b) $h = 9.9\,\mathrm{mm}$

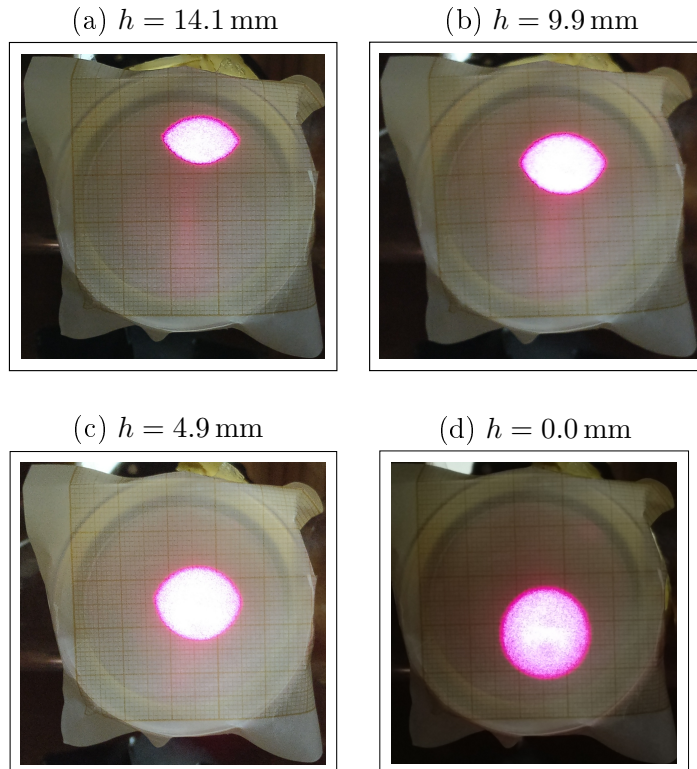(c) $h = 4.9\,\mathrm{mm}$ (d) $h = 0.0\,\mathrm{mm}$

Figure 5.16: Pictures of the spotsize represented by luminescent millimeter scaled paper for some example heights. At the port at the opposite site of the pick-up optic a piece of a millimeter scaled paper is attached and the output of the diode laser system is guided through the pick-up optics. The illuminated area represents the scaled spot size at the center of the discharge tube. To get a comparable correction function between all measured heights the ratio of the number of pixels of the illuminated area and an area of $A = 1\,\mathrm{cm}^2$ of the scaled paper is calculated with a graphic programm. Normalizing these ratios to the value of the central ratio yields the height-dependent function $\Omega(h)$ for profile LIF measurements.

height [mm]	#pixel$_{spot}$	#pixel$_{cm^2}$	ratio	profile correction factor Ω
14.1	34001	28728	0.8449	2.2124
12.9	36543	27888	0.7632	1.9984
11.9	40094	27885	0.6955	1.8212
10.9	43706	28728	0.6573	1.7211
9.9	48785	29237	0.5993	1.5693
8.9	50234	28044	0.5583	1.4619
7.9	55568	29925	0.5385	1.4101
6.9	58582	30798	0.5257	1.3765
5.9	60250	28896	0.4796	1.2558
4.9	71762	32037	0.4464	1.1689
3.9	68201	29237	0.4287	1.0964
3.0	68387	28050	0.4102	1.0741
2.1	73085	28718	0.3929	1.0288
1.0	76504	28900	0.3778	0.9893
0.0	525566	200700	0.3819	1.0000

Table 5.4: Measured heights with corresponding values for the number of pixels of the spot and of $A = 1 \, \mathrm{cm}^2$ of the scaled paper, the calculated ratios and the profile correction factors. The values of Ω were taken to fit a quadratic equation to them (5.20).

5.2.5 Line intensity ratio measurements

Due to the high plasma density of up to $n_e \leq 7 \cdot 10^{20}$ m^{-3} and a variety of energetic states of the argon atom in the helicon plasma discharge, one needs a collisional, radiative model to calculate the quantitative population of the different metastable states and the dependencies of the fluorescence lines on temperature and plasma density [Zhang et al., 2011] (4.1). The radiative model for the metastable states to compare with the experimental LIF measurements can also be used the other way around. With given plasma density and fluorescence signals of the metastable states used for LIF the needed electron temperature [Kano et al., 2000] is calculated. The plasma density is experimentally determined by independent measurements with the 2-pass CO_2 laser interferometer (section 5.2.1) and the fluorescence signals are experimentally quantified with the LIF setup described in section 5.2.2. Since the reaction rate model provides the population and reaction rates of the relevant atomic states, it is sufficient to just gather the raw PMT data to calculate the natural fluorescence intensity. The light emitted by the plasma at specific wavelengths is collected by the PMT through a fiber optics interface as described in figure 5.1. The plasma emissivity

$\lambda[nm]$	$T(\lambda)$ of flange windows	$T(\lambda)$ of fiber	$T(\lambda)$ of lenses	$T(\lambda)$ of filter	$\eta(\lambda)$ of PMT
750.59 (neutral)	99.78	99.5	92.2	70	0.04
442.72 (ion)	73	99	91.63	55	23

Table 5.5: Values for the transmission factors and quantum efficiency of the neutral and ion fluorescence lines as taken for LIF measurements in PROMETHEUS-A taken from product characteristics.

at a defined wavelength λ_{ji} from a transition from level j to level i can be written as [Wiese et al., 1966]:

$$\epsilon_{ji} = (4\pi)^{-1} h\nu_{ji} N_j A_{ji}, \qquad (5.21)$$

where $h\nu_{ji}$ is the energy of the emitted photon of the transition, N_j is the population of the upper, emitting energetic level and A_{ji} is the Einstein coefficient for the transition. Assuming a uniform plasma, the measured photon count rate is given by

$$I_{\mathrm{p}}(\lambda_{ji}) = (4\pi)^{-1} N_j A_{ji} V \Omega T(\lambda_{ji}) \eta(\lambda_{ji}), \qquad (5.22)$$

with V as the plasma volume used for the fluorescence measurements, Ω as solid angle subtended by the pick-up optics, $T(\lambda_{j,i})$ as transmission factor of the detection system and $\eta(\lambda_{j,i})$ as the quantum efficiency of the PMT at the wavelength $\lambda_{j,i}$. Thus, the ratio of two different photonic count rates is

$$\frac{I_{\mathrm{p}}(\lambda_{ji})}{I_p(\lambda_{kl})} = \frac{N_j A_{ji} T(\lambda_{ji}) \eta(\lambda_{ji})}{N_k A_{kl} T(\lambda_{kl}) \eta(\lambda_{kl})} = \frac{1}{F_{\mathrm{R}}} \frac{N_j A_{ji}}{N_k A_{kl}}, \qquad (5.23)$$

with F_{R} as relative calibration factor for known atomic transitions and wavelenths. Since a suitable light source to directly measure the transmissivity of the optical system was not available the relative calibration factor was theoretically calculated. In table 5.5 all values for the transmission factor and quantum efficiency of the neutral and ion fluorescence lines are compiled. In total the relative calibration function is calculated to be

$$\frac{1}{F_{\mathrm{R}}} = \frac{T(\lambda_{\mathrm{ion}}) \eta(\lambda_{\mathrm{ion}})}{T(\lambda_{\mathrm{neutral}}) \eta(\lambda_{\mathrm{neutral}})} = \frac{13.0280}{4231.7300} \approx 0.0031. \qquad (5.24)$$

The principle of line ratio calculations makes it irrelevant to know the exact measured plasma volume and solid angel and due to the fact that the fluorescence measurements yield a qualitative intensity. It is anyway necessary anyway to measure the nearly independent neutral and ion fluorescence lines to obtain a

line intensity ratio. In total several conditions have to be fulfilled to use a line ratio measurement [Boivin et al., 2001]:

- ionization process by electron collisions, partially balanced by three-body recombination

- excitation of atomic states by electron collisions

- dependence of line ratio as much as possible on electron temperature and as little as possible on plasma density

- radiation mainly emitted by spontaneous emission

- plasma optically thin for emitted radiation

The first requirements for the ionization, recombination and excitation processes are described in section 4.2 and depicted from figure 4.10 to 4.15. For varying temperature and filling gas pressure, the ionization and excitation process of atomic states are primarily influenced by electron collisions and the main recombination channel is the three-body recombination. Figure 5.17 shows the line ratio of the metastable states for increasing electron temperature and filling gas pressure (number of particles). It is seen that the ratio depends more on electron
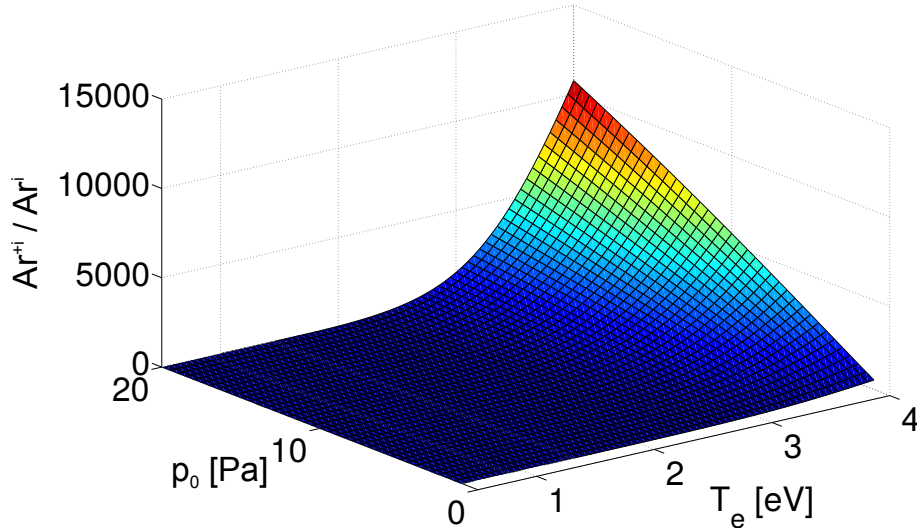
Figure 5.17: Line ratio of the investigated fluorescence lines of metastable states for increasing electron temperature and filling gas pressure (number of particles). The ratio depends more on electron temperature than on plasma density.

temperature than on plasma density, what is in line with the described premises. The qualification that radiation is just emitted by spontaneous emission is possessed by the results of the reaction rate model, showing a main loss channel as spontaneous emission (figure 4.14) .

To proof that a transmission line is optically thin and that the plasma does not affect the transmission, one must examine if both the stimulated emission and absortion are negligible compared to the spontaneous emission. If that is the case, the line intensity can be described with (5.21) and the principle of line ratio calculations can be used. There are two important quantities describing the opacity of a plasma, the mean optical depth (MOD) τ_0 and the optical escape factor (OEF) $\Lambda(\tau_0)$. The MOD is the exponential absorption coefficent for a given transition ($I = I_0 \mathrm{e}^{-\tau_0}$) and the OEF corresponds to the fraction of light able to escape the plasma. For an OEF close to unity the plasma is optically thin. In connection with the discussion in section 5.2.2, the dominant broadening mechanism is the Doppler broadening. Taking that into account, the mean optical depth τ_0 and the optical escape factor $\Lambda(\tau_0)$ are given by [Boivin et al., 2001]

$$\tau_0 = \tau(\nu_0) = \frac{n_i g_j A_{ji} \lambda_0^3 r}{8 g_i \pi^{3/2} v_{\mathrm{th}}}, \tag{5.25}$$

$$\Lambda(\tau_0) = 1 - \sum_{i=1}^{n} \frac{(-1)^{i+1} \tau_0^i}{\sqrt{i+1} i!}, \tag{5.26}$$

where n_i is the population density of the lower level, g_i and g_j are the statistical weights of the lower and upper levels, respectively and λ_0 is the central wavelength associated with the transition.

Due to the fact that plasmas are increasingly opaque as the plasma density increases only one example for high plasma densities is shown. Considering the high power helicon plasma in PROMETHEUS-A with a filling gas pressure of $p_0 = 5\,\mathrm{Pa}$, a plasma density of $n_e = 6.5 \cdot 10^{20}\,\mathrm{m}^{-3}$, an electron temperature of $T_e = 1.5\,\mathrm{eV}$, a column radius of $r = 1.5\,\mathrm{cm}$ and a thermal velocity (from LIF measurements) of $v_{\mathrm{th}} = 600\,\mathrm{m/s}$ one can determine the metastable densities with the help of the collisional radiative model (section 4.1). The calculated populations are $n_{in} = 2.9 \cdot 10^{15}\,\mathrm{m}^{-3}$ for neutrals and $n_{ii} = 1.74 \cdot 10^{15}\,\mathrm{m}^{-3}$ for the final ionic metastable state.

transition ($j \rightarrow i$)	λ_0 [nm]	$A_{ji}[10^8\,\mathrm{s}^{-1}]$	g_i	g_j	$n_i[m^{-3}]$
$(^2\mathrm{P}^0_{1/2})4p \rightarrow (^2\mathrm{P}^0_{1/2})4s$	750.59 (neutral)	0.445	1.102	1.380	$2.9 \cdot 10^{15}$
$(^3\mathrm{P})4p \rightarrow (^3\mathrm{P})4s$	442.72 (ion)	0.817	1.722	1.722	$1.74 \cdot 10^{15}$

Table 5.6: Quantities of the measured transitions for neutral argon and argon ions. Considering a high power helicon plasma with a filling gas pressure of $p_0 = 5\,\mathrm{Pa}$, a plasma density of $n_e = 6.5 \cdot 10^{20}\,\mathrm{m}^{-3}$, an electron temperature of $T_e = 1.5\,\mathrm{eV}$, a column radius of $r = 1.5\,\mathrm{cm}$ and a thermal velocity (from LIF measurements) of $v_{\mathrm{th}} = 600\,\mathrm{m/s}$ the metastable densities n_i were calculated with the help of the collisional radiative model.

Taking these computed and other values shown in table 5.6 into account, combined with (5.26) the optical escape factor yields

$$\Lambda(750.59\,\mathrm{nm}) = 0.9735 \tag{5.27}$$

for the specific transition in neutral argon and

$$\Lambda(442.72\,\mathrm{nm}) = 0.9962 \tag{5.28}$$

for the described transition between argon ions. With these evaluated values one can say that the investigated argon plasma is optically thin for the relevant atomic transitions and all conditions are fulfilled to use such a line ratio measurement.

As described before the plasma density is measured with the 2-pass CO_2 laser interferometer and the PMT signals of the characterized fluorescence lines (see table 5.2) are measured with the laser-induced fluorescence diagnostic setup without the use of the exciting laser. Taking both PMT signals, the neutral and ion metastable fluorescence line into account and calculating the ratio $Q = 1/F_R \cdot I_{\mathrm{Ar}^+}/I_{\mathrm{Ar}}$ with the calibration function $1/F_R$ (5.24) to get the line ratio inside of the plasma, the electron temperature is calculated using the collisional radiative model. An illustration is shown in figure 5.18. WIth the collisional radiative model the theoretical dependencies of $n_e(p_0,T_e)$ and $Q(p_0,T_e)$ are calculated. Knowing the lower and upper limits of the measured quantities at each given time, trajectories in the pressure-temperature space can be found. For illustration an plasma density of $n_e = 2.0 \pm 0.1 \cdot 10^{20}\,\mathrm{m}^{-3}$ and a line ratio $Q = 3.75 \pm 0.05 \cdot 10^{-3}$ are shown. The plasma densities are shown in red and the line ratios in blue. In the next step the points of intersection of $n_e(\mathrm{low})|Q(\mathrm{low})$ and $n_e(\mathrm{high})|Q(\mathrm{high})$ are calculated, yielding the respective lower and upper limits of the gas pressure p_0 and electron
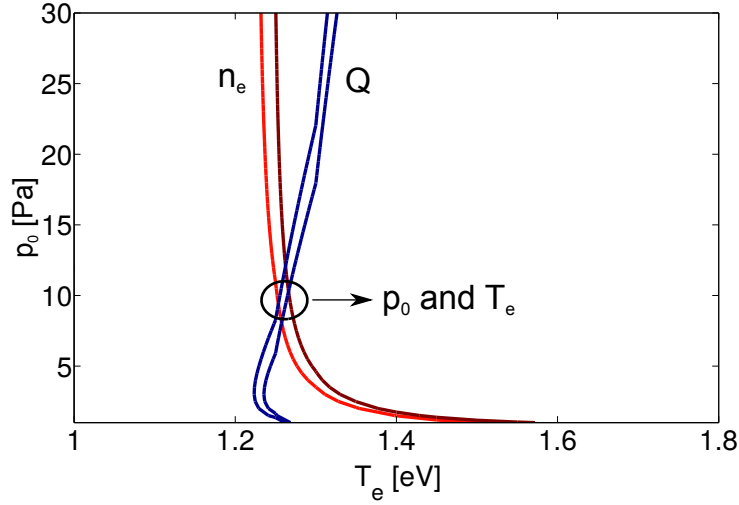
Figure 5.18: Calculation of the pressure and electron temperature with the help of the collisional radiative model. Trajectories in the pressure-temperature space can be found with known lower and upper limits of the measured quantities of plasma density (red, brown) and line ratio (blue, black). Here $n_e = 2.0 \pm 0.1 \cdot 10^{20} \, \mathrm{m}^{-3}$ and $Q = 3.75 \pm 0.05 \cdot 10^{-3}$ are shown. The intersections of $n_e(\mathrm{low})|Q(\mathrm{low})$ and $n_e(\mathrm{high})|Q(\mathrm{high})$ yield the respective lower and upper limits for the gas pressure p_0 and electron temperature T_e. Here a pressure of $p_0 = 9 \pm 1 \, \mathrm{Pa}$ and an electron temperature of $T_e = 1.28 \pm 0.01 \, \mathrm{eV}$ are calculated.

temperature T_e. By entering the measured error into the scheme as described, the calculation of the error of pressure and temperature is implemented by default. The example results in an electron temperature of $T_e = 1.28 \pm 0.01 \, \mathrm{eV}$ and a pressure of $p_0 = 9 \pm 1 \, \mathrm{Pa}$.

Chapter 6

Experimental results

This chapter addresses the question if the plasma parameter requirements as defined by the AWAKE project are achievable (see chapter 2). The experimental setup of the helicon plasma cell PROMETHEUS-A, the laser-diagnostic setups and the numerical methods have been described in chapter 5. Subsequently, the experimental results are shown and discussed, e.g., the goal plasma density and the width and time of the peak plasma density. A summary on this subject was also recently published [Buttenschön et al., 2018]. Another important aspect is if the radial plasma density profile is centrally peaked and if the time evolution of the plasma density is similar over the whole profile and reproducable. It is investigated how the change of experimental parameters influences the plasma density and some limitations are shown. To characterize the plasma, the electron temperature is calculated and compared to the plasma density evolution for different experimental parameters. To investigate the argon neutral gas and singly ionized atom evolution, laser induced fluorescence measurements of metastable argon densities are evaluated using the rate reaction model (chapter 4).

6.1   Plasma density profile

An important requirement for the use of PWFAs is a centrally peaked plasma density profile. In the central region the self modulated proton bunches and electrons travel through the helicon discharge and the desired high accelerating electric fields are created.
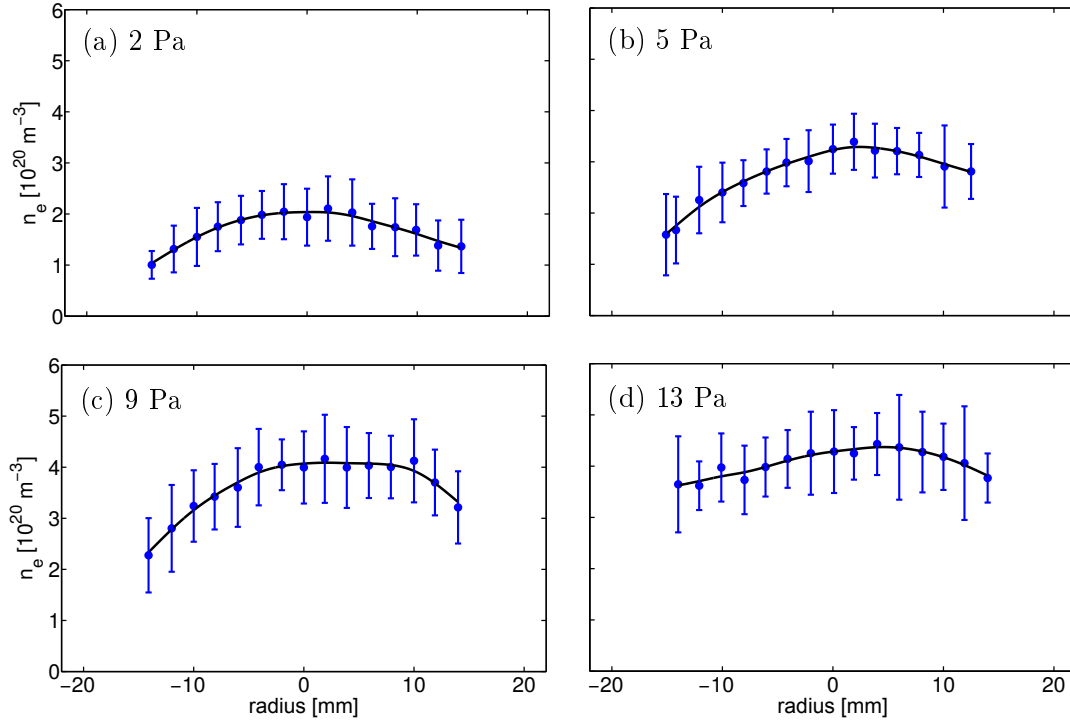
Figure 6.1: Density profile measurements at $B = 105\,\mathrm{mT}$, $P_{\mathrm{RF}} = 9\,\mathrm{kW}$ and a varying filling neutral gas pressure taken at the time instant of highest plasma density. The data points are shown in blue with their corresponding error bars. A spline fit is shown in black. At low pressures the profile is centrally peaked and rises in plasma density with increasing pressure by simultaneously building up a nearly flat top plasma density profile.

The shown interferometer measurements of profiles are conducted at varying filling neutral gas pressures, magnetic induction of $B = 105\,\mathrm{mT}$, and RF powers of $P_{\mathrm{RF}} = 9\,\mathrm{kW}$ and $P_{\mathrm{RF}} = 24\,\mathrm{kW}$ (figures 6.1 and 6.2). For all shown profiles the time instant of highest plasma density was chosen in each measurement and the axis limits are chosen equally for comparison reasons. In most cases shown in figures 6.1 (9 kW) and 6.2 (24 kW) the plasma density profile is centrally peaked or exhibits a region of high plasma density around the center of the discharge. Around $\pm 5\,\mathrm{mm}$ from the center of the discharge, the plasma density is at more than 90 % of the peak plasma density. At low filling gas pressure the plasma density profile is peaked, at high filling gas pressure discharge a nearly flat-top profile is found. In the evolution from low to high filling gas pressures the peak plasma density rises the higher the pressure gets with saturation starting at $p_0 = 9\,\mathrm{Pa}$. The biggest enhancement is between the three lowest pressure cases. Increasing the pressure from 2 Pa to 13 Pa, first in the positive part of the profile the plasma

density rises. At $p_0 = 13\,\mathrm{Pa}$ also the negative part rises, forming nearly a flat top profile. Comparing figures 6.1 (9 kW) and 6.2 (24 kW) the global behavior as described above is the same with the difference that in the higher power case higher plasma densities are achieved.
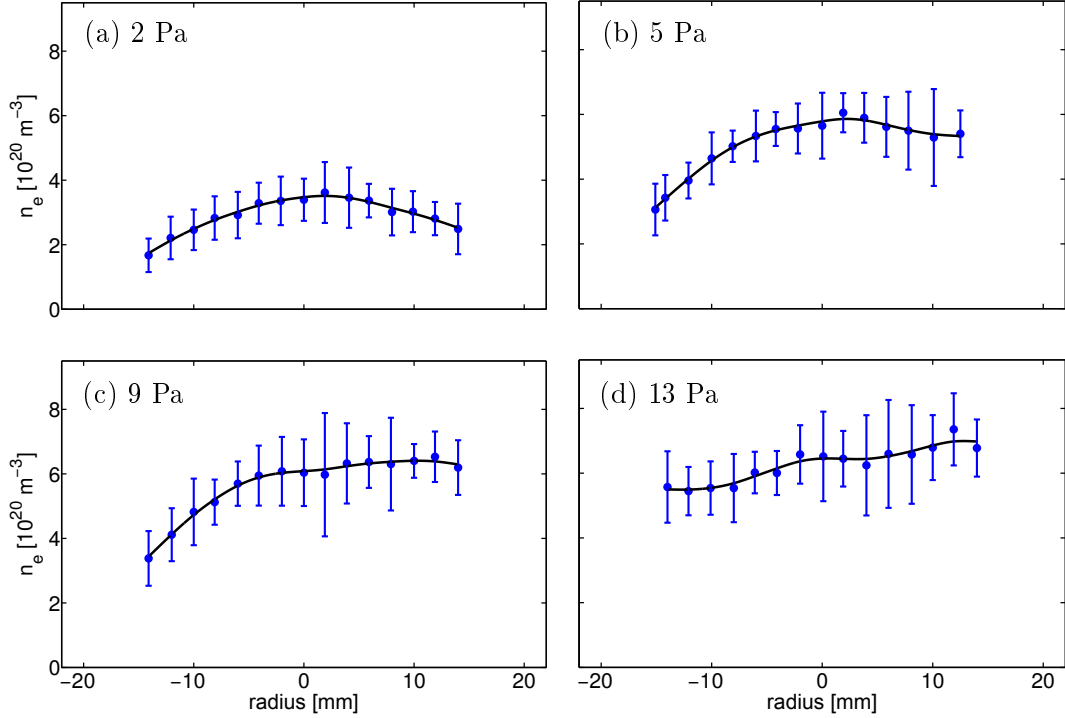
Figure 6.2: Profile measurements at $B = 105\,\mathrm{mT}$, $P_{\mathrm{RF}} = 24\,\mathrm{kW}$ and a varying filling neutral gas pressure taken at the time instant of highest plasma density. The data points are shown in blue with their corresponding error bars. A spline fit is shown in black. At low pressures the profile is centrally peaked and rises in plasma density with increasing pressure by simultaneously building up a nearly flat top plasma density profile.

In summary the plasma density profiles are characterized by the highest plasma density around the center of the discharge, with a peaked plasma density profile for lower gas pressures and a nearly flat top profile for higher filling gas pressures. Central heating and the development of a high plasma density region in the center of the discharge is a helicon discharge characteristic driven by non-resonant heating and ionization processes in the highly collisional helicon plasma. The maximum plasma density increases with increasing filling neutral gas pressure and increasing RF power.

6.1.1   Time evolution of plasma density profile

The previous section has shown the density profiles at their peak values measured with the laser interferometer. But the time evolution of the density profiles is also of interest.
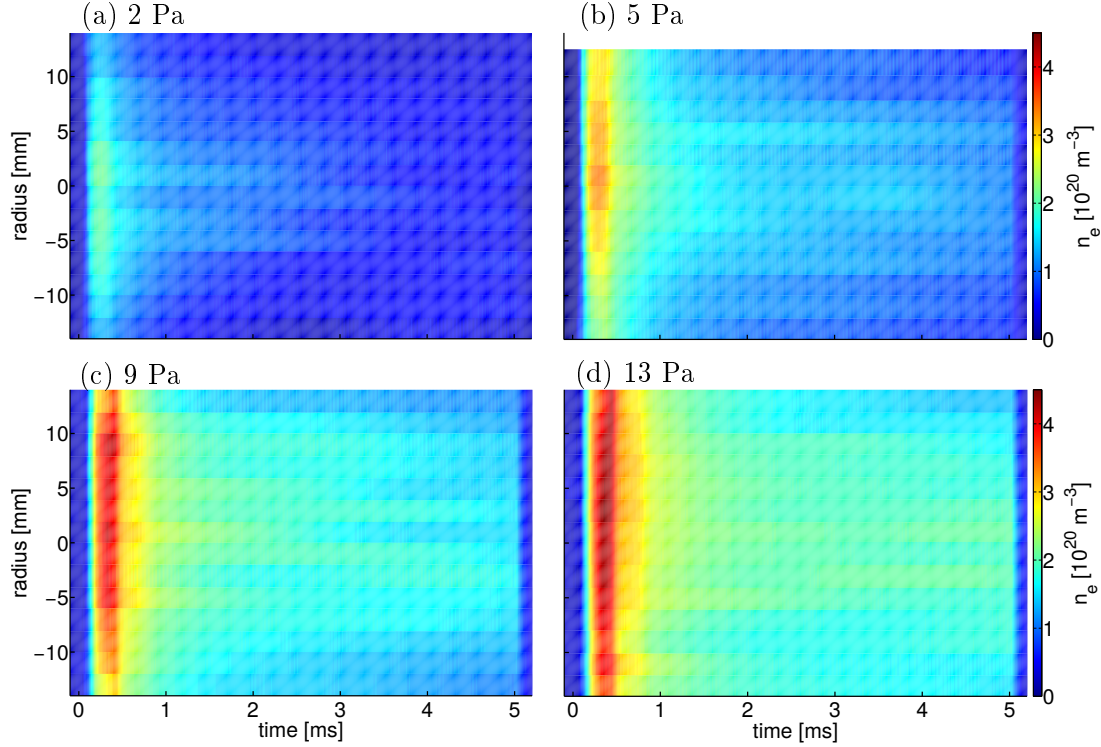
Figure 6.3: Time resolved plasma density profile measurements at $B = 105\,\mathrm{mT}$, $P_{\mathrm{RF}} = 9\,\mathrm{kW}$ and different filling neutral gas pressures of 2 Pa (a), 5 Pa (b), 9 Pa (c) and 13 Pa (d). The axes and color bars are chosen equally.

Figures 6.3 and 6.4 summarize the time evolution of plasma density profiles over the whole duration of the plasma discharge. The RF-heating is turned on at $t_{\mathrm{on}} = 0\,\mathrm{ms}$ and turned off at $t_{\mathrm{off}} = 5\,\mathrm{ms}$. Figures 6.3 and 6.4 correspond with parameters to the density profiles in figures 6.1 and 6.2. After switching on the RF power, the plasma density increases steeply over the first $250 - 350\,\mathrm{\mu s}$ to a maximum and decreases afterwards until the end of the discharge. After swiching off the RF power the plasma density decays nearly exponentially back to zero in less than $500\,\mathrm{\mu s}$. During the transient phase a Gaussian-like plasma density profile is established, independent of the starting density profile with the highest plasma densities. At low gas pressures (2 Pa and 5 Pa) a Gaussian-like starting profile is visible, whereas a more flat-top starting profile is established with increasing filling gas pressure.

90
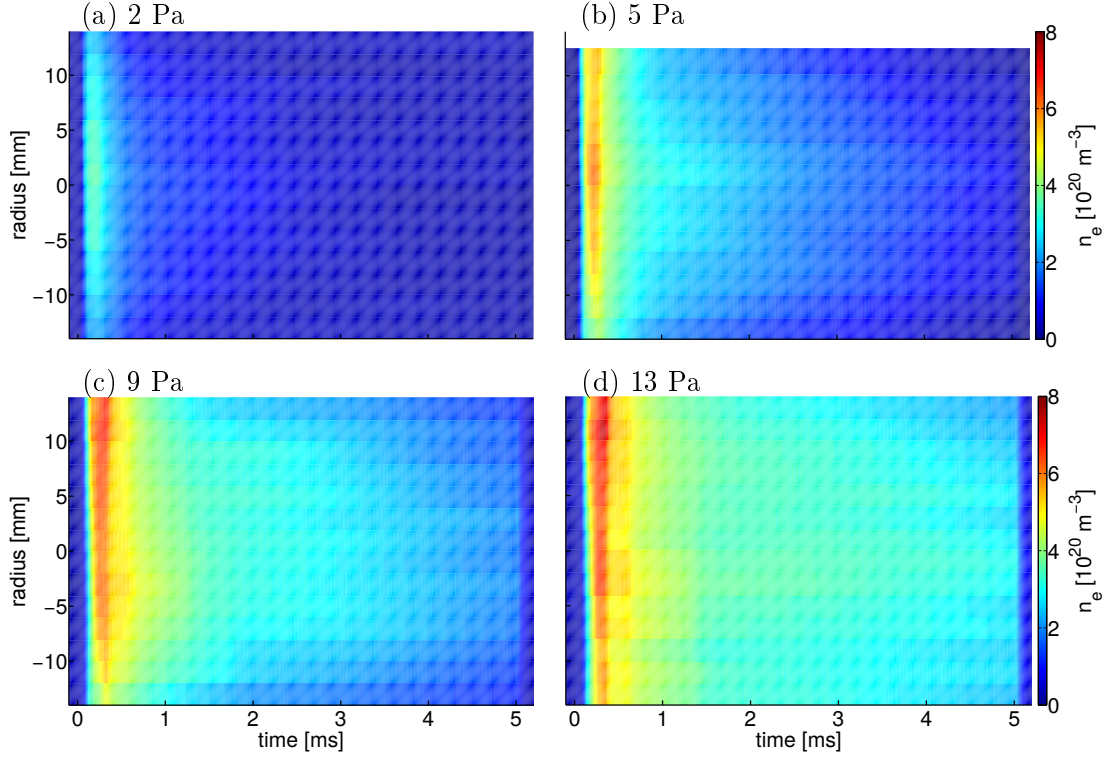
Figure 6.4: Time resolved plasma density profile measurements at $B = 105\,\mathrm{mT}$, $P_{\mathrm{RF}} = 24\,\mathrm{kW}$ and different filling neutral gas pressures of 2 Pa (a), 5 Pa (b), 9 Pa (c) and 13 Pa (d). The axes and color bars are chosen equally.

At $p_0 = 2\,\mathrm{Pa}$ centrally peaked profiles stay over the whole discharge time interval independent of different RF powers. It appears that the plasma density is limited by the neutral gas particles, especially at high RF power. A filling pressure of $p_0 = 2\,\mathrm{Pa}$ corresponds to a particle density of $n = 4.8 \cdot 10^{20}\,\mathrm{m}^{-3}$ and consequently, in the measurements at $p_0 = 2\,\mathrm{Pa}$ and $P_{\mathrm{RF}} = 24\,\mathrm{kW}$ an ionization degree of more than 80% is reached. That indicates a plasma density limit by the available number of argon atoms. In the case of high filling pressure and high RF power, the peak plasma density is not limited by the particle density but by the heating power coupled into the plasma, the increasing electron-neutral collision rate, and the increasing recombination rate of argon ions (figure 4.10). A neutral gas filling pressure of $p_0 = 13\,\mathrm{Pa}$ corresponds to a neutral particle density of $n = 3 \cdot 10^{21}\,\mathrm{m}^{-3}$, which corresponds to an ionization degree of 23%.

6.2 Plasma density dependencies

As discussed in the previous section the plasma density depends on various discharge parameters. To investigate the in more detail, measurements with different discharge and operation parameters (magnetic induction, filling neutral gas pressure, RF power) were performed. All measurements were performed at RF powers of $P_{RF} = 9\,\text{kW}$ and $P_{RF} = 24\,\text{kW}$, $p_0 = 9\,\text{Pa}$ filling neutral gas pressure and a magnetic induction of $B = 105\,\text{mT}$. In the measurements two parameters were kept fixed and one parameter is varied. With increasing magnetic induction the
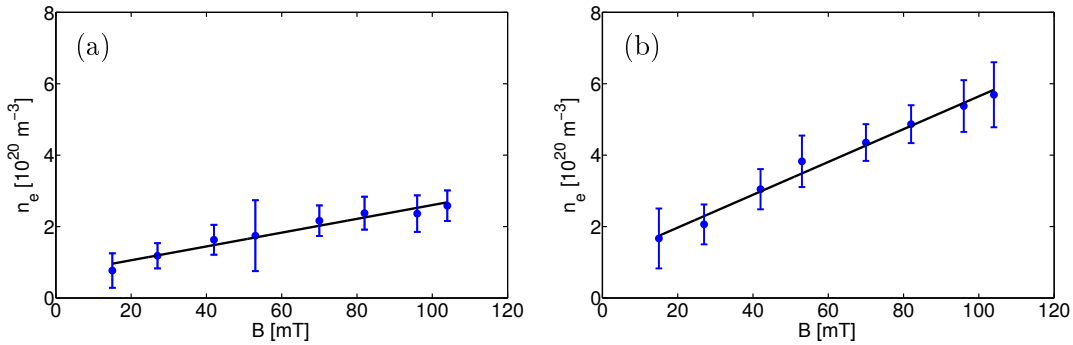
Figure 6.5: Plasma density for increasing magnetic field induction B at $P_{RF} = 9\,\text{kW}$ (a) and $P_{RF} = 24\,\text{kW}$ (b) at $p_0 = 9\,\text{Pa}$ filling gas pressure. The plasma density (blue) rises almost linearly with B. The black line is a linear best fit.

plasma density rises almost linearly, as shown in figure 6.5 for low and high RF power. The blue dots with error bars are the measured plasma densities and values and the black line is a linear best fit. The linear dependence of the plasma density on the magnetic field induction B is consistent with the helicon dispersion relation (3.4), which is proportional to the magnetic induction if $\omega_{LH} < \omega_{RF}$ (with ω_{LH} as lower hybrid frequency and ω_{RF} as RF frequency). Inside the range of the investigated magnetic field induction (limited by the maximum available coil current) no saturation or turning point in the plasma density development is found. The point where $\omega_{LH} \approx \omega_{RF} = 13.56\,\text{MHz}$ at an magnetic induction of $B \approx 130\,\text{mT}$ is not reached in the present study (see figure 3.2). The plasma density dependence on the filling neutral gas pressure (figure 6.6) exhibits a different behavior. First there is a linear increase in plasma density with increasing filling neutral gas pressure up to $p_0 \approx 5\,\text{Pa}$. This is a turning point and the plasma density reaches a maximum at $p_0 = 9 - 10\,\text{Pa}$. At higher filling neutral gas pressure the plasma density saturates at lower heating power ($P_{RF} = 9\,\text{kW}$) and

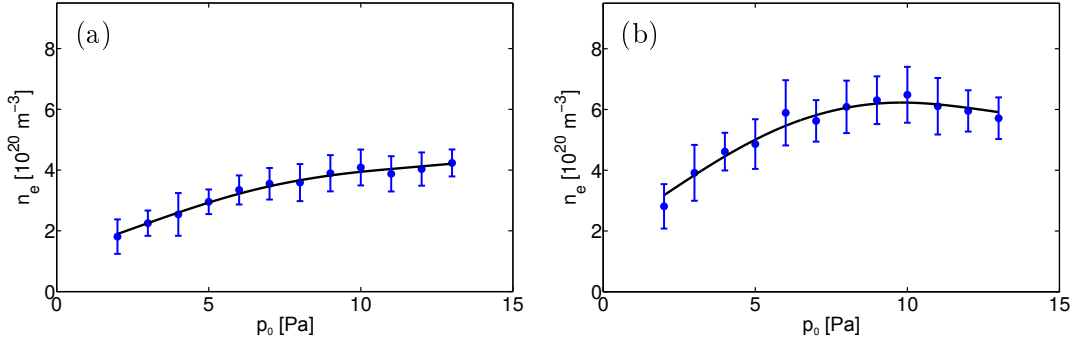Figure 6.6: Plasma density for increasing filling neutral gas pressure p_0 at $P_{RF} = 9\,\text{kW}$ (a) and $P_{RF} = 24\,\text{kW}$ (b) and a magnetic induction of $B = 105\,\text{mT}$. A linear increase in the plasma density (blue) up to a filling neutral gas pressure of $p_0 \approx 5\,\text{Pa}$ is found.

starts to decrease in the higher power case ($P_{RF} = 24\,\text{kW}$). The plasma density dependence on a varying filling neutral gas pressure reflects the prior findings. At higher filling neutral gas pressure the plasma density is limited by the heating power coupled into the plasma and the increasing recombination rate of argon ions (figure 4.10). With increasing heating power from the RF source the plasma density monotonically increases (figure 6.7) but there is no linear dependency and there is a certain saturation for increasing RF power. With more heating power input higher ionization level are possible. But a saturation process is visible with increasing heating power indicating a decreasing efficiency in heating power coupling into the plasma with simultaneously increasing recombination and neutral atom quenching rates .
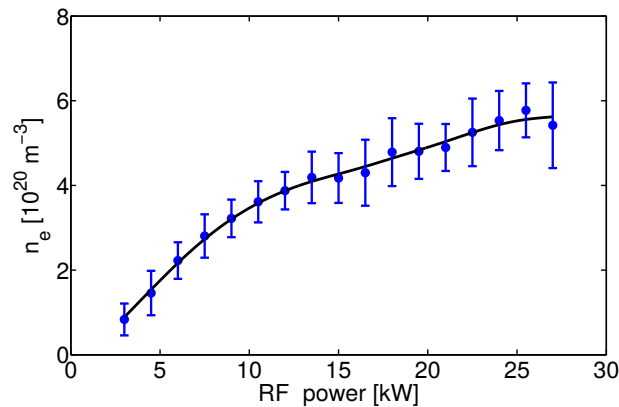
Figure 6.7: Plasma density for increasing RF heating power at $p_0 = 9\,\text{Pa}$ filling neutral gas pressure and a magnetic induction of $B = 105\,\text{mT}$. With increasing RF heating power the plasma density (blue) rises, but not linearly. The slope of the fit (black) decreases with increasing RF power, indicating a saturating process.

93

6.2.1   Plasma density time evolution

In this section we discuss the time evolution of the plasma density profiles for varying discharge and operation parameters: magnetic induction, filling neutral gas pressure, input RF power. The time evolution of the plasma density profiles in the center of the discharge is shown in figures 6.8, 6.9 and 6.10. The dependence of the peak plasma density from these different parameters was discussed above (section 6.2).   It is evident that the temporal evolution of the central plasma density shows for all cases the same characteristics as already described in section
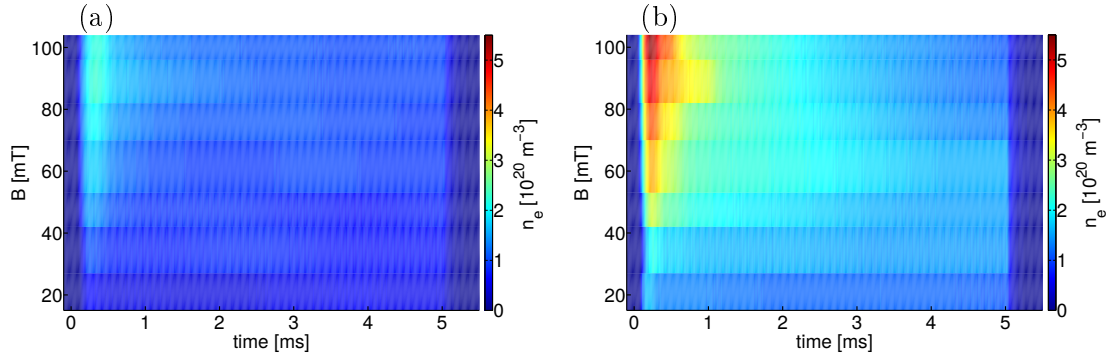
Figure 6.8: Time evolution of plasma density for increasing magnetic induction at $P_{\mathrm{RF}} = 9\,\mathrm{kW}$ (a) or $P_{\mathrm{RF}} = 24\,\mathrm{kW}$ (b) and $p_0 = 9\,\mathrm{Pa}$ filling gas pressure. With increasing magnetic induction the peak plasma density rises clearly and the width of the peaks seem to get broader.
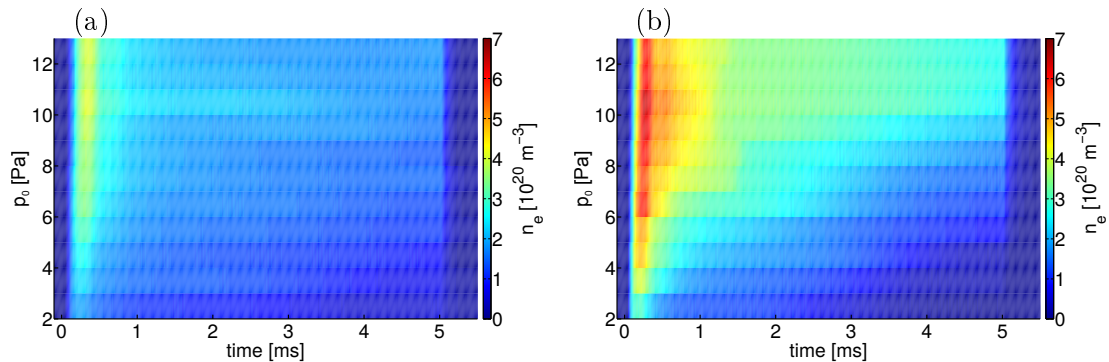
Figure 6.9: Time evolution of plasma density for increasing filling neutral gas pressure at $P_{\mathrm{RF}} = 9\,\mathrm{kW}$ (a) or $P_{\mathrm{RF}} = 24\,\mathrm{kW}$ (b) and a magnetic induction of $B = 105\,\mathrm{mT}$. There an obvious rise in peak plasma density with increasing filling neutral gas pressure, reaching a maximum around $p_0 = 10\,\mathrm{Pa}$. Also the equilibrium state reached at the end of the discharge rises in plasma density.

6.1.1. After switching on the RF power the plasma density increases steeply to a maximum value and decreases in a transient to an equilibrium value. The equilibrium value increases with increasing magnetic induction (figure 6.9) but this behavior is most pronounced in the pressure variation (figure 6.9). After switching off the RF power the plasma density decays fast back to zero in less than 500 μs. With the change of parameters it gets obvious that the peak plasma
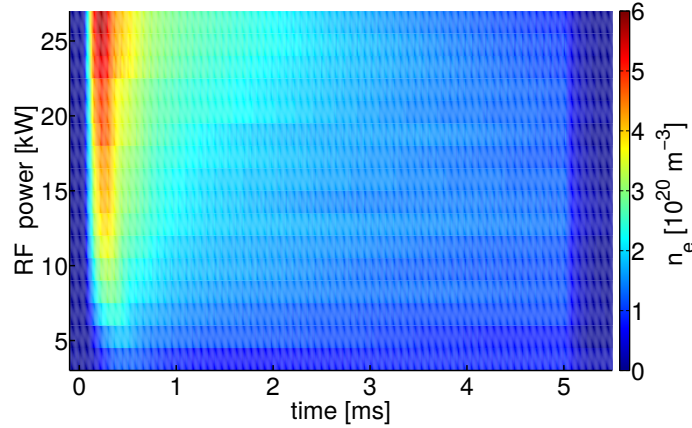

Figure 6.10: Time evolution of plasma density for increasing RF heating power at $p_0 = 9\,\mathrm{Pa}$ filling gas pressure and a magnetic induction of $B = 105\,\mathrm{mT}$. With increasing RF heating power the peak plasma density rises and the peaks of plasma density seem to occur earlier.

density is different in width and time of the plasma density peak. With increasing magnetic induction the peak gets broader and with increasing RF power the peaking of plasma density occurs earlier. The behavior is investigated in the next section to address the question how the time and width of the plasma density peak depend on operation parameters.

6.2.2   Plasma density peaking time

The design of a plasma cell for a PWFA requires a good understanding of the peak plasma density and the related control parameters. In this section, the same parameter variation as in the previous sections are made. The plasma density peaking time (PDPT) is investigated in the center of the discharge and shown in figures 6.11, 6.12 and 6.13 for varying magnetic induction, filling neutral gas pressure and RF power, respectively. In all three figures into account the density peaks in the time interval of $200 - 500\,\mathrm{μs}$, but the exact point in time depends on
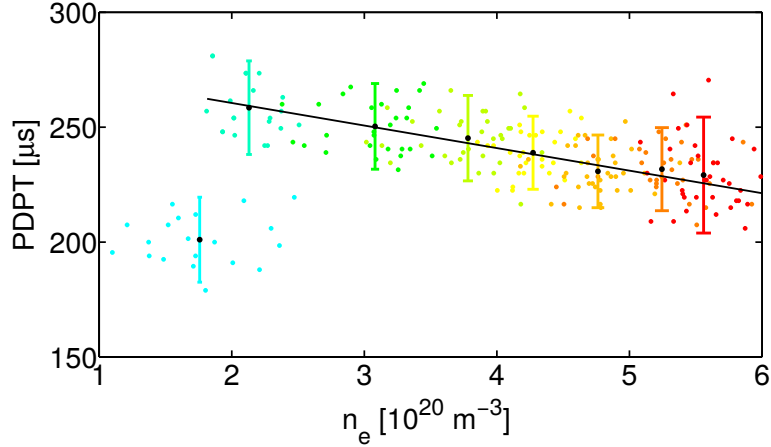
Figure 6.11: Plasma density peaking time for increasing peak plasma density for varying magnetic induction at $P_{RF} = 24\,\mathrm{kW}$ and $p_0 = 9\,\mathrm{Pa}$. The light blue color represents $B = 14\,\mathrm{mT}$ and the red color $B = 105\,\mathrm{mT}$ with $\Delta B = 14\,\mathrm{mT}$. Each dot indicates a single measurement. The black symbols show the mean values of the plasma density peaking time with respective error bars and a spline curve is shown to guide the eye.

the discharge parameter. For increasing magnetic induction a linear dependence of the PDPT is found if the first data points are neglected. In figure 6.11 the light blue color represents a magnetic induction of $B = 14\,\mathrm{mT}$ and the red color a magnetic induction of $B = 105\,\mathrm{mT}$ with steps of $\Delta B = 14\,\mathrm{mT}$ in between them. Each dot indicates a single measurement. The black symbols show the mean values in time and plasma density with the respective error bars. With increasing magnetic induction a higher variation in plasma density peaking time is observed, represented by the longer error bars. A step in the plasma density peaking time at low magnetic inductions of $B = 10 - 20\,\mathrm{mT}$ is observed, followed by a continuous decrease with increasing magnetic induction. The jump is likely to correspond to a mode-jump from the inductive into the helicon discharge mode. In addition, the distance in plasma density values decreases with increasing magnetic induction, which suggests a plasma density limit for increasing magnetic induction. With increasing filling neutral gas pressure, the plasma density peaks continuously later, as shown in figure 6.12. The dark blue color represents a gas pressure of $p_0 = 2\,\mathrm{Pa}$, the red color $p_0 = 13\,\mathrm{Pa}$ with steps of $\Delta p_0 = 1\,\mathrm{Pa}$ in between. As above each dot indicates a single measurement. If the measurements at highest filling neutral gas pressure are excluded, a quadratic increase of the plasma density peaking time with p is found. Again there is a plasma density limit at higher filling neutral gas pressure p, where the plasma density peaking time still rises, but the plasma density starts to decrease (see also figure 6.6). With increasing RF
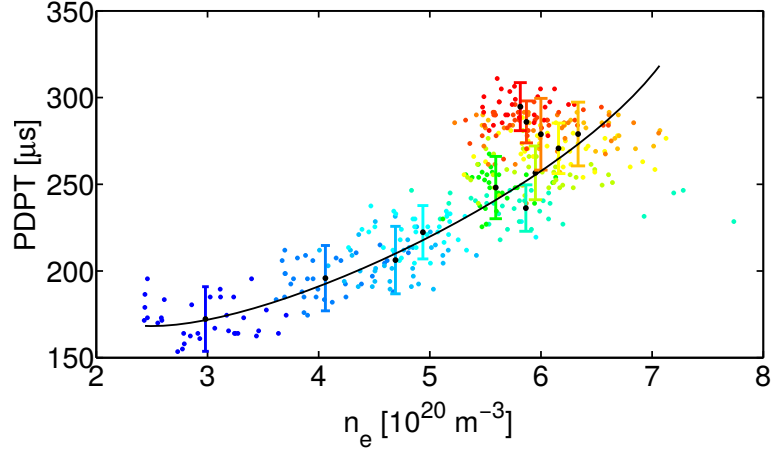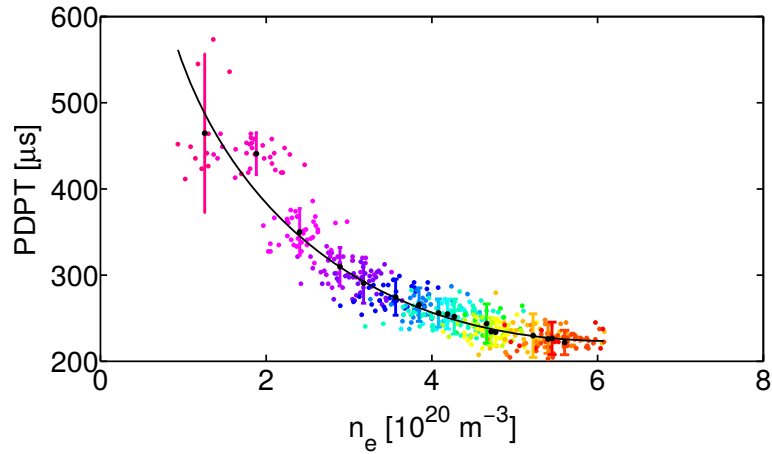
Figure 6.12: Plasma density peaking time for increasing peak plasma density for varying filling neutral gas pressure at $P_{\mathrm{RF}} = 24\,\mathrm{kW}$ and a magnetic induction of $B = 105\,\mathrm{mT}$. The dark blue color represents $p_0 = 2\,\mathrm{Pa}$ and the red color $p_0 = 13\,\mathrm{Pa}$ with $\Delta p_0 = 1\,\mathrm{Pa}$. Each dot indicates a single measurement. The black symbols show the mean values in plasma density peaking time with respective error bar and a spline curve is shown to guide the eye.

Figure 6.13: Plasma density peaking time for increasing peak plasma density for varying RF power at $p_0 = 9\,\mathrm{Pa}$ filling gas pressure and a magnetic induction of $B = 105\,\mathrm{mT}$. The magenta color represents $P_{\mathrm{RF}} = 1.5\,\mathrm{kW}$ and the red color $P_{\mathrm{RF}} = 27\,\mathrm{kW}$ with $\Delta P_{\mathrm{RF}} = 1.5\,\mathrm{kW}$. Each dot indicates a single measurement. The black symbols show the mean values in plasma density peaking time with respective error bar and a spline curve is shown to guide the eye.

power the plasma density peaking time decreases and saturates at high RF power values at around $220\,\mu s$, as shown in figure 6.13. The behavior can be fitted by an exponential function. The magenta color represents a RF power of $P_{RF} = 1.5\,kW$ and the red color $P_{RF} = 27\,kW$ with steps of $\Delta P_{RF} = 1.5\,kW$ in between. The PDPT strongly varies at low powers, indicating a fluctuating energy input and little reproducability. The variation lowers at higher powers. At the highest value of input heating power, the plasma density drops due to arcing inside the setup. All parameter studies have shown that the plasma denstiy peaking time varies within the time interval of $200 - 500\,\mu s$ and is controllable by adjusting the discharge parameters especially at the highest plasma densities. The optimum is found at a magnetic induction of $B = 105\,mT$, a RF power of $P_{RF} = 24\,kW$ and a filling gas pressure of $p_0 = 9\,Pa$ with a PDPT of around $t = 250\,\mu s$.

6.2.3 Plasma density peaking width

The peak plasma density must have a certain time duration. This is to make sure that in this time interval the proton bunch can move through the hundred meters long plasma column with a high plasma density region of a spatial variation of less than 1% (section 2.2.2). In the present section the width of the peak plasma density is investigated for the same parameters as in the previous two sections. Figures 6.14, 6.15 and 6.16 show the width at $98\,\%$ of peak plasma density for a range of magnetic induction, filling neutral gas pressure, and RF power, respectively. The width of the peak plasma density changes in a time interval of $20 - 100\,\mu s$, but is different for the respective discharge parameter. With increasing magnetic induction the plasma density peaking width (PDPW) increases and saturates at $\approx 60\,\mu s$ (figure 6.14). The light blue color indicates a magnetic induction $B = 14\,mT$ and the red color a magnetic induction of $B = 105\,mT$ with steps of $\Delta B = 14\,mT$ in between. At low magnetic induction a jump in the plasma density peaking width is observed at the same plasma density as for the plasma density peaking time plasma densty (figure 6.11). After the jump the PDPW increases with increasing magnetic induction. Simultaneously the variation in the plasma density peaking width decreases. The broadening of the peak plasma density profile width with increasing magnetic induction is due to reduced radial diffusive transport. The picture changes at higher magnetic induction, resulting in a weak decrease in plasma density peaking width and an increase in variation. The behavior is an indication for a discharge mode change
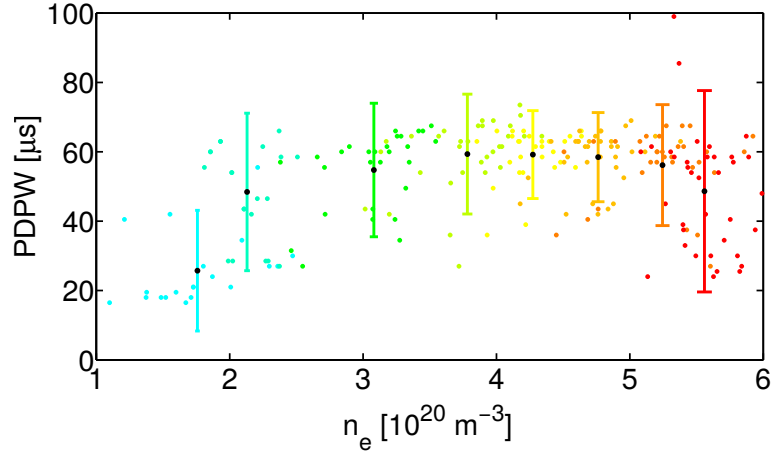
Figure 6.14: Plasma density peaking width for increasing peak plasma density for varying magnetic induction at $P_{RF} = 24\,kW$ and $p_0 = 9\,Pa$. The light blue color represents $B = 14\,mT$ and the red color $B = 105\,mT$ with $\Delta B = 14\,mT$. Each dot indicates a single measurement. The black data points show the mean values of the plasma density peaking width with the respective error bars.

to the so-called Trivelpiece-Gould mode (section 3.3) and that the current mode coupling gets inefficient. With higher filling gas pressure the peak plasma density peaking width shows no clear trend within the error bars, but is always in the range of $60\,\mu s$ (figure 6.15). The dark blue color represents a filling gas pressure of $p_0 = 2\,Pa$ and the red color $p_0 = 13\,Pa$ with steps of $\Delta p_0 = 1\,Pa$ in between. With increasing heating power the PDPW decreases and saturates at high power values at a width of $60\,\mu s$ (figure 6.16). The magenta color represents a RF power of $P_{RF} = 1.5\,kW$ and the color red $P_{RF} = 27\,kW$ with steps of $\Delta P_{RF} = 1.5\,kW$ in between. At low RF power the plasma density peaking widths exhibit a wide spread. The spread reduces to a low level at high powers. All investigated cases have in common that the plasma density peaking width changes within a time interval of $20 - 100\,\mu s$. The shortest PDPW is accomplished in a region of low variation and highest plasma density. This is found in the same parameter regime as for the plasma density peaking time described in the previous section, i.e. at a magnetic induction $B = 105\,mT$, a RF power $P_{RF} = 24\,kW$, and a filling neutral gas pressure $p_0 = 9\,Pa$. Here the plasma density peaking width is $\approx 60\,\mu s$ with a low variation. This particular PDPW is more than sufficient for a relativistic particle passing a 1 km long cell, corresponding to a time-of-flight of $5\,\mu s$.
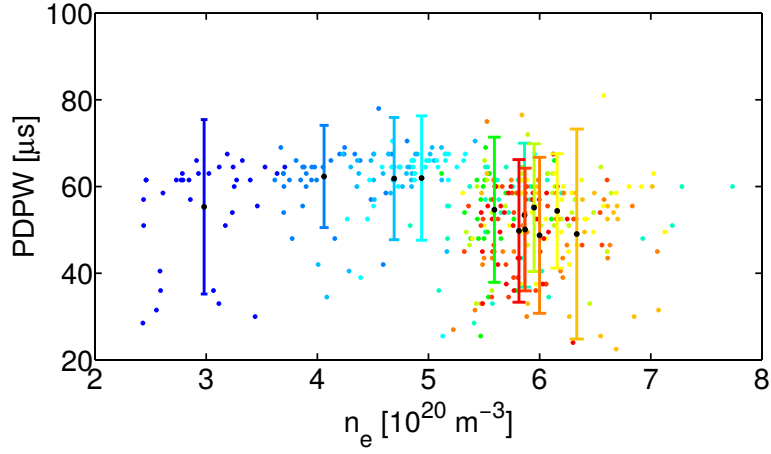
Figure 6.15: Plasma density peaking width for increasing peak plasma density for varying filling neutral gas pressure at $P_{\mathrm{RF}} = 24\,\mathrm{kW}$ and a magnetic induction $B = 105\,\mathrm{mT}$. The dark blue color represents $p_0 = 2\,\mathrm{Pa}$ and the red color $p_0 = 13\,\mathrm{Pa}$ with $\Delta p_0 = 1\,\mathrm{Pa}$. Each dot indicates a single measurement. The black data points show the mean values of the plasma density peaking width with the respective error bars.
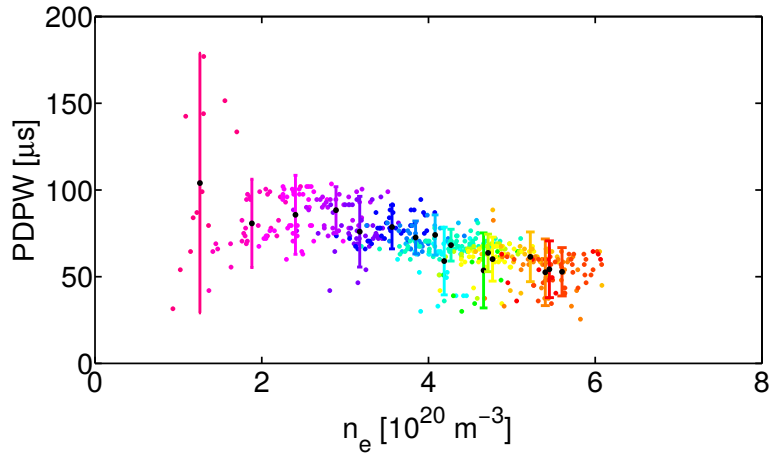

Figure 6.16: Plasma density peaking width for increasing peak plasma density for varying RF power at $p_0 = 9\,\mathrm{Pa}$ filling gas pressure and a magnetic induction $B = 105\,\mathrm{mT}$. The magenta color represents $P_{\mathrm{RF}} = 1.5\,\mathrm{kW}$ and the red color $P_{\mathrm{RF}} = 27\,\mathrm{kW}$ with $\Delta P_{\mathrm{RF}} = 1.5\,\mathrm{kW}$. Each dot indicates a single measurement. The black data points show the mean values in plasma density peaking width with the respective error bars.

6.3 Reproducability of plasma density evolution

Important for the use of plasma discharges for PWFAs is discharge reproducability. Especially the high plasma density peak has to be stable. The measurements of the time evolution of the plasma density are done for different filling neutral gas pressure, a magnetic induction $B = 105\,\mathrm{mT}$ and RF powers $P_{\mathrm{RF}} = 9\,\mathrm{kW}$ and $P_{\mathrm{RF}} = 24\,\mathrm{kW}$ (figures 6.17 and 6.18). All measurements are done at the center of the discharge and the axis limits are chosen equally. The mean value of all measurements is shown as a black line with a grey shaded area representing the standard deviation. The temporal behavior corresponds to the time evolution discussed in section 6.4. The RF heating is switched on at $t_{\mathrm{on}} = 0\,\mathrm{ms}$ and switched off at $t_{\mathrm{off}} = 5\,\mathrm{ms}$. After switching on the RF power the plasma density increases steeply over the first $250 - 350\,\mathrm{\mu s}$ to a maximum plasma density and decreases transiently until the end of the discharge. The peak value of plasma density increases with increasing gas pressure as well as with increasing RF power.
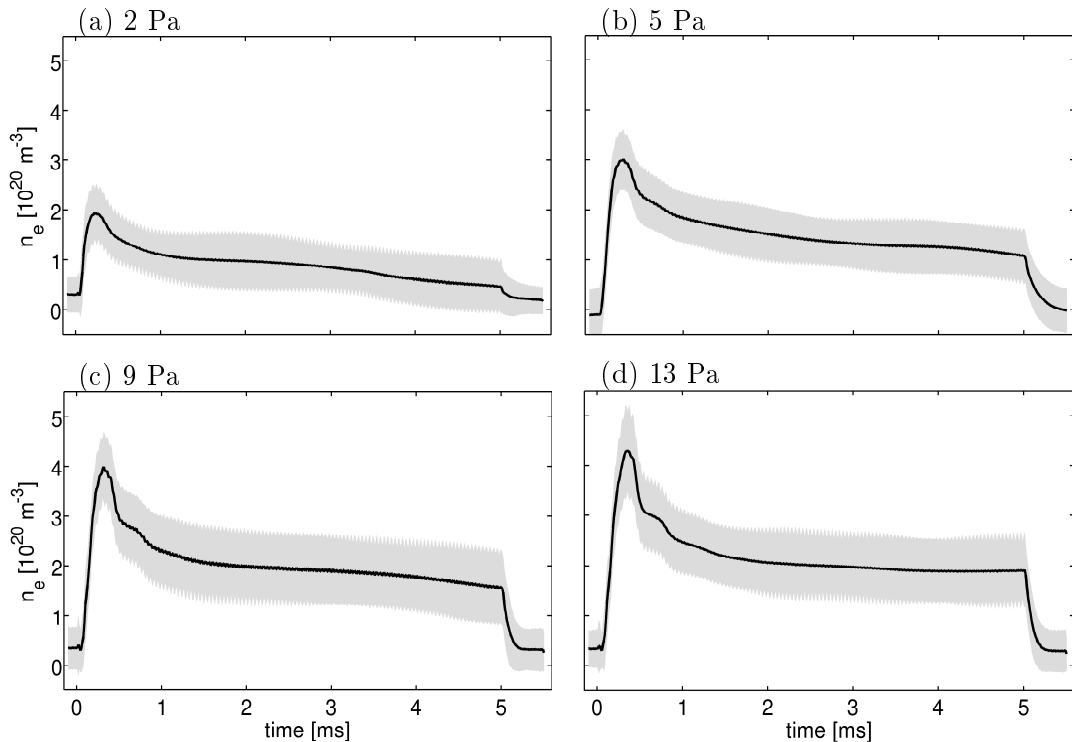

Figure 6.17: Time evolution of the plasma density at the center of the discharge for different filling gas pressures at $B = 105\,\mathrm{mT}$ and $P_{\mathrm{RF}} = 9\,\mathrm{kW}$. The mean value of all discharges is shown as a black curve with a grey shaded area representing the standard deviation. The RF power is switched on at $t_{\mathrm{on}} = 0\,\mathrm{ms}$ and turned off at $t_{\mathrm{off}} = 5\,\mathrm{ms}$.

The temporal evolution of the plasma density is always similar within the error bars. Even at high filling neutral gas pressure and high RF power, where the peak plasma density starts to decline (see figure 6.9), and at low magnetic induction or low heating power the time evolution is reliably reproducable.
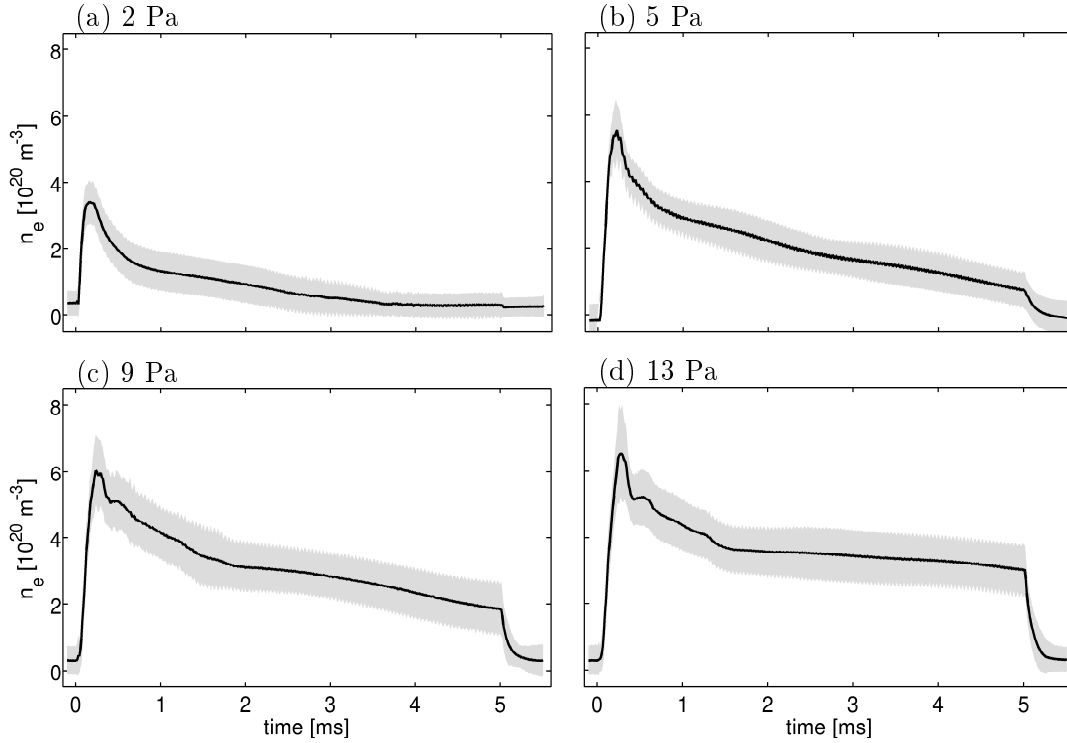

Figure 6.18: Time evolution of the plasma density at the center of the discharge for different filling gas pressures at $B = 105\,\mathrm{mT}$ and $P_{\mathrm{RF}} = 24\,\mathrm{kW}$. The mean value of all discharges is shown as a black curve with a grey shaded area representing the standard deviation. The RF power is switched on at $t_{\mathrm{on}} = 0\,\mathrm{ms}$ and turned off at $t_{\mathrm{off}} = 5\,\mathrm{ms}$.

6.4 Target plasma density

An indispensable specification for the use of the helicon plasma cell for PWFAs is the requirement to reach plasma density values of $n_{\mathrm{e}} > 7 \cdot 10^{20}\,\mathrm{m}^{-3}$. The results from the CO_2 laser interferometer measurements are obtained at high RF power of $P_{\mathrm{RF}} = 24\,\mathrm{kW}$, $p_0 = 9\,\mathrm{Pa}$ filling gas pressure and a magnetic induction of $B = 105\,\mathrm{mT}$. At these parameters the highest plasma density with a low variation and a sufficient width of the peak plasma density are reached. As seen in figure 6.19 the radial plasma density profile is rather flat-top than Gaussian.
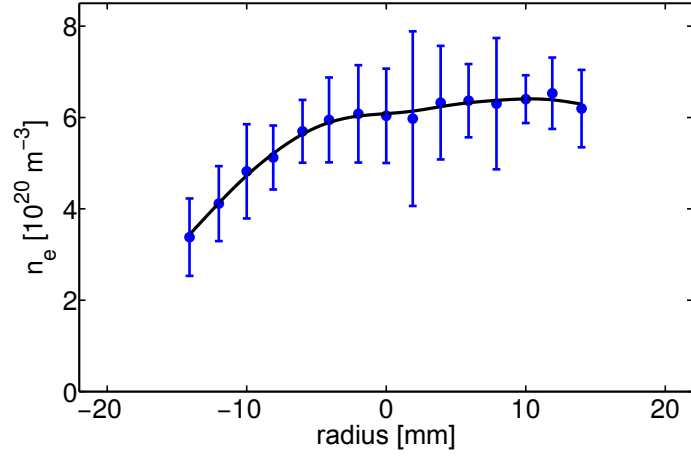
Figure 6.19: Radial profile measurement for the plasma density at the time instant of highest plasma density at $t = 270\,\mu s$. The density data points are shown in blue with their corresponding error bars. A fitted spline curve is shown in black to guide the eye. A flat top profile is found with a central plasma density of $n_e = 6 \pm 1 \cdot 10^{20}\,m^{-3}$.

The profile was measured at the time instant of highest plasma density around $270\,\mu s$. The flat-top profile has a center width of $\approx 10\,mm$ and with a peak density of $n_e = 6 \pm 1 \cdot 10^{20}\,m^{-3}$. Looking at the time evolution of the plasma density profile (figure 6.20) the flat top profile evolves quickly over the first few ms to a Gaussian-like profile, remaining the same shape over the residual time of the discharge but decreasing in density. The RF heating power is switched on at $0\,ms$ and switched off at $5\,ms$. One finds turning points in the density evolution in figure 6.20, more apparent in figure 6.21 which shows the density evolution in the center of the discharge. After the RF is switched on the plasma
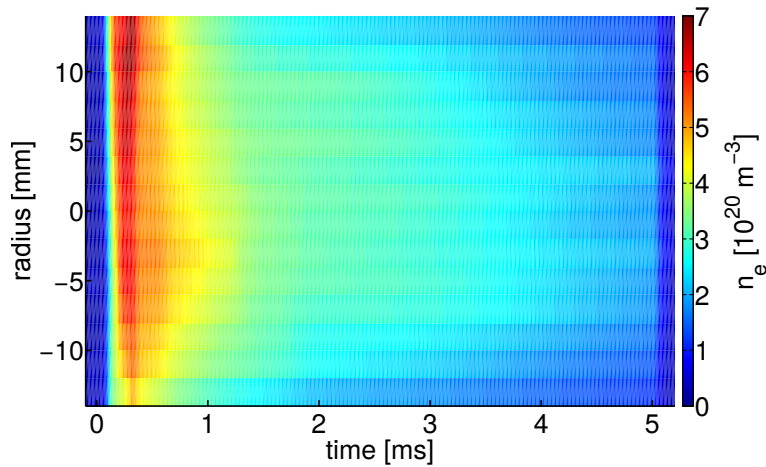

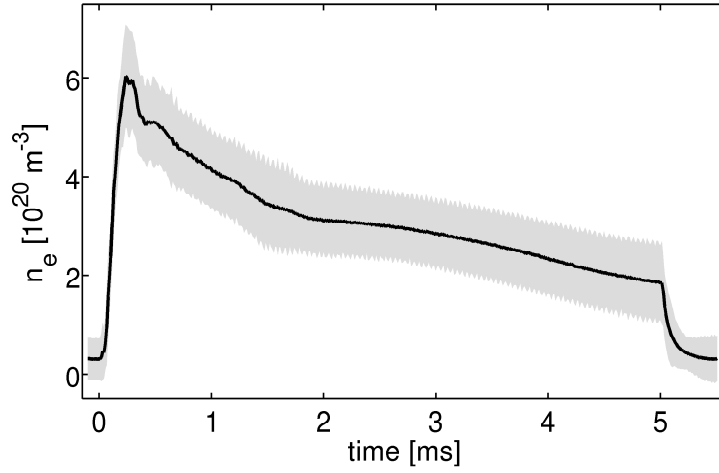Figure 6.20: Time evolution of the radial plasma density profile.

Figure 6.21: Time evolution of the plasma density in the center of the discharge. The mean value of the measurements is shown as a black line with a grey area representing the standard deviation.

density increases steeply over the first $250-350\,\mu s$ to the maximum density and decreases over $1\,ms$ faster than in the subsequent time interval until the end of the discharge. After switching off the RF power the electron density decreases nearly exponentially back to zero in less than $500\,\mu s$.

The plasma density peaking time depends on the radial position as shown in figure 6.22, i.e. in the center of the discharge the peak densities are reached earlier. Each dot represents a single discharge and the mean value of all discharges at each radius is shown in black grey error bar. The plasma density peaking time varies
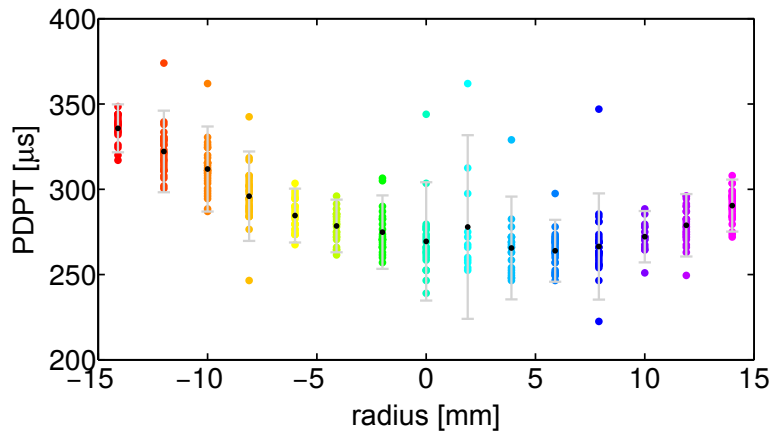

Figure 6.22: Plasma density peaking time at different radii. Each colored dot represents a single discharge. Each mean value at one radius value is shown in black and is underlined with a grey error bar.

from 340 μs at the edge to 270 μs in the center of the discharge. In the center of the discharge a low plasma density peaking time is reached, corresponding to the location of the highest plasma densities with a width of ≈ 10 mm.

The radial variation of the width of the plasma density peaking is shown in figure 6.23. It is determined as the time interval of $\pm 2\,\%$ of the respective peak plasma density. The color coding is the same as for figure 6.22. The width of the peak plasma density is found to be constant at about 50 μs over the whole radial plasma profile.
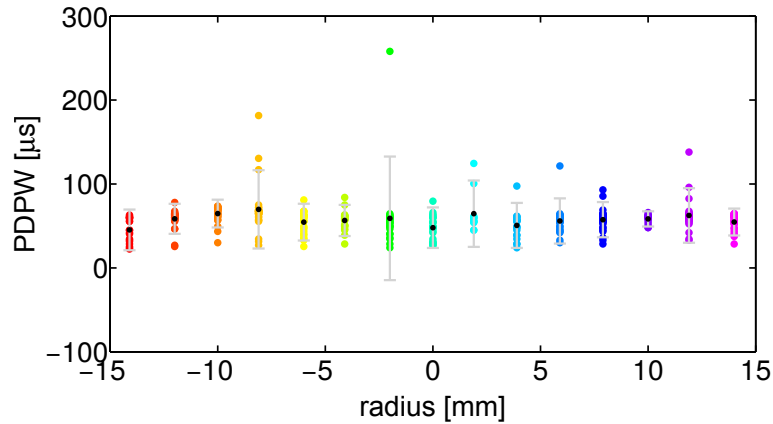

Figure 6.23: Plasma density peaking width for increasing radius. The measured radii are coded in different colors and each colored dot is representing a single discharge. Each calculated mean value of all discharges at a single radius is shown in black and is underlined with a grey error bar. The peak width is nearly constant around a width of about 50 μs over the whole profile.

The above measurements have shown that the required density of $n_e > 7 \cdot 10^{20}\,\text{m}^{-3}$ for the use in a wakefield accelerator can be accomplished. The peak plasma density is limited by the available RF power. It is also limited by the magnetic induction. The helicon dispersion relation, as shown in section 3.3, is proportional to the magnetic induction if $\omega_{\text{LH}} < \omega_{\text{RF}}$. At higher magnetic induction ω_{LH} gets close to ω_{RF} and n_e starts to saturate or even decrease, due to the change of coupling modes. This density limit is not yet reached here, but at a magnetic induction of 100 mT $\omega_{\text{LH}} \approx \omega_{\text{RF}}$. The high plasma densities at early plasma density peaking times indicate a more efficient heating in the center of the discharge as expected.

6.5 Temperature regime

Typical for a collision dominated helicon discharge is a low electron temperature regime. As discussed in section 5.2.5 the electron temperature can be determined by combining the collisional radiative model (section 4) with the line ratio of two spontaneously emitted LIF lines. The results are shown in figure 6.24. The maximum electron temperature is found at 1.4 eV for high heating power, high gas pressure and high magnetic induction. The electron temperature also varies
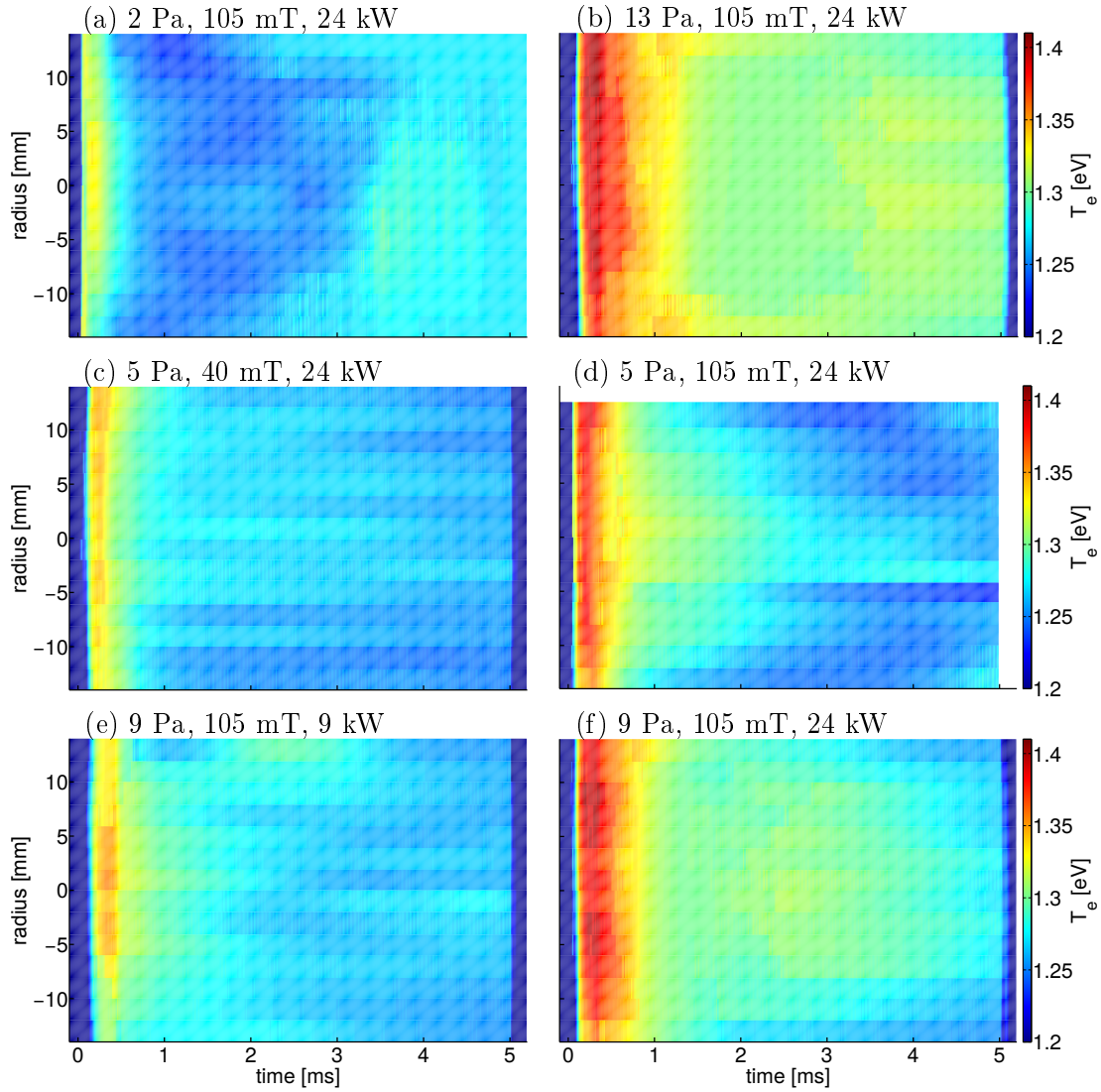

Figure 6.24: Time evolution of the radial electron temperature profile for different discharge parameters. The maximum electron temperature is ≈ 1.4 eV. The time evolution corresponds to the plasma density profile evolution shown in figure 6.4.

over time similar ro the plasma density. After switching on the RF power the electron temperature increases steeply over the first $200 - 250\,\mu s$ to a maximum value and decreases transiently until the end of the discharge. After switching off the heating power, the electron temperature decreases fast. The time behavior is analogous to the density evolution as described in the previous sections. The electron temperature profile is also Gaussian-like, similar to the plasma density profile and remains so over the whole discharge time. The electron temperature profile is consistent with helicon wave heating via collisional power dissipation.

6.5.1 Link to density evolution

A direct comparison of plasma density and electron temperature is shown in figure 6.25 for low and high RF powers $P_{RF} = 9\,\mathrm{kW}$ or $P_{RF} = 24\,\mathrm{kW}$ at $p_0 = 9\,\mathrm{Pa}$ and $B = 105\,\mathrm{mT}$. Comparing the plasma density and electron temperature it is seen that the time evolution of the electron temperature profile closely follows that of the plasma density profile for different parameters. Taking a closer look, the plasma density peaking time and the increase of the electron temperature occurs just before the plasma density peaks, respectively starts to rise. Additionally, the electron temperature peaking width (ETPW) seems to be greater than the plasma density peaking width. Electron temperature profiles taken at the time instant of highest plasma density are shown in figure 6.26. At low heating power the temperature profile is centrally peaked but shows a higher temperature for $r > 10\,\mathrm{mm}$, similar to the plasma density profiles shown in figure 6.1. For high heating power a nearly flat top electron temperature profile is found from $-10...10\,\mathrm{mm}$ as already found in the plasma density profiles shown in figure 6.2. This is expected for a centrally heated helicon discharge. In figures 6.27 and 6.28 the evolution of plasma density and electron temperature in the center of the discharge are shown in a single plot for low and high RF power. For both cases it is found that the electron temperature rises first and the plasma density follows. The peak of the electron temperature is clearly broader than for the plasma density, resulting in an earlier and faster decrease of the plasma density. This development is even more pronounced for a high RF power discharge. A high plasma density and pressure gradient in the center of the discharge results in an increased loss of particles at the axial and radial boundaries of the discharge. The high plasma density also reduces the ionization mean-free path of argon neutrals moving radial inwards from the wall to just a few mm. The can lead to a depletion of argon neutrals in the center
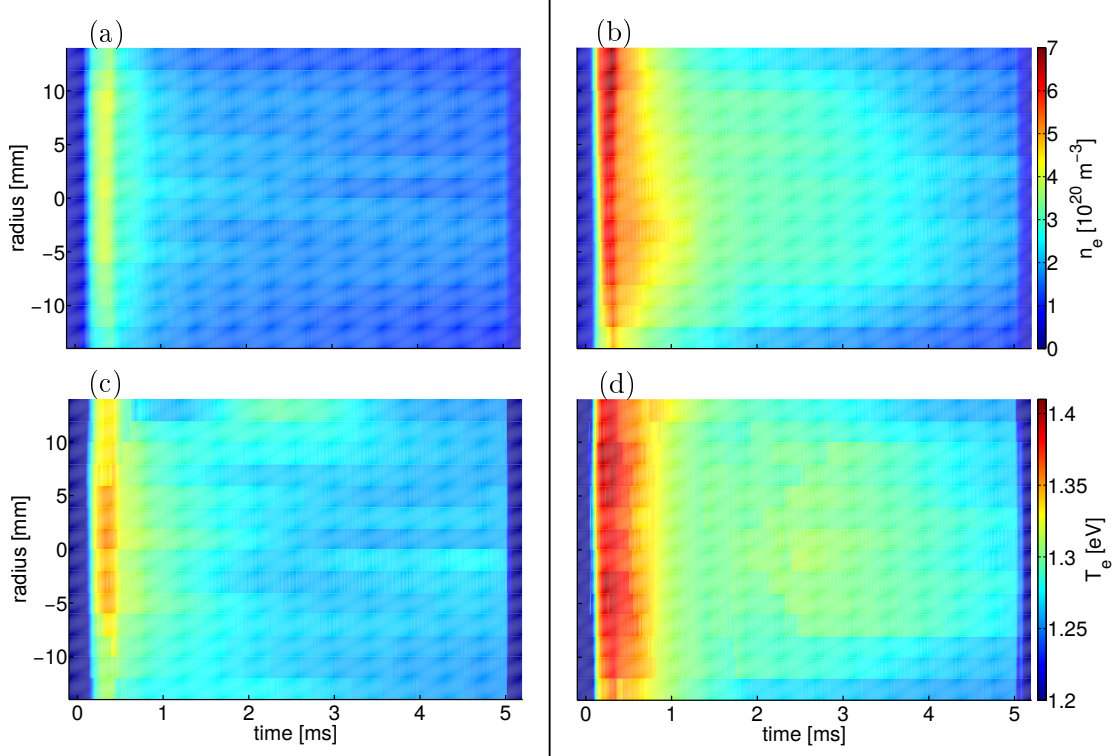
Figure 6.25: Comparison of plasma density (a,b) and electron temperature (c,d) for RF powers of 9 kW (a,c) and 24 kW (b,d) at $p_0 = 9$ Pa and $B = 105$ mT. The time evolution of the electron temperature follows the time evolution of the plasma density.
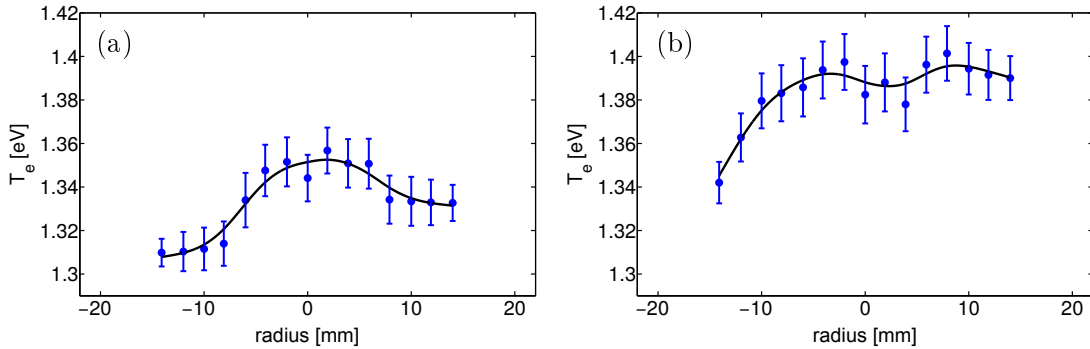
Figure 6.26: Electron temperature profile for measurements at $B = 105$ mT, $p_0 = 9$ Pa and $P_{RF} = 9$ kW (a) and $P_{RF} = 24$ kW (b) taken at the time instant of highest plasma density. The data points are shown in blue with their respective error bars. A spline curve is shown in black to indicate the profile.

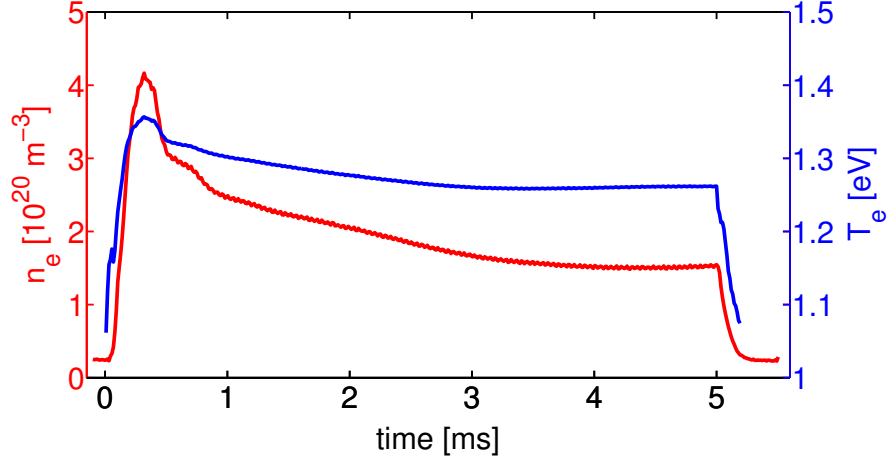Figure 6.27: Comparison of plasma density and electron temperature at $p_0 = 9\,\mathrm{Pa}$, $B = 105\,\mathrm{mT}$ and $P_{\mathrm{RF}} = 9\,\mathrm{kW}$.

of the discharge, resulting in a decrease of plasma density after the neutrals were partially ionized and the plasma density peak was reached. This behavior is investigated in more detail in the next section, where LIF measurements of neutrals and ions are discussed. In figures 6.29 and 6.30 a comparison between the Plasma density peaking time and width, and electron temperatures for low and high RF power cases are shown. At low power the plasma density peaking time is usually lower than the electron temperature peaking time, except for the center of the discharge where they are similar. At high heating power the peaking times are almost the same. The electron temperature peaking width is more than a factor of 10-15 larger than the plasma density peaking width. In figure 6.29 it is seen that the radial profile of both peaking time and peaking width of the electron temperature are hollow. In the center of the discharge the lowest values are found, as expected from the central heating of a helicon discharge. The fast increase of the electron temperature prior to the plasma density is owing to the increasing collisional ionization rates for higher electron temperatures. The earlier peaking time and lower peaking width of the plasma density is due to increased particle losses, decreasing ionization and increasing recombination rates (figure 4.10).
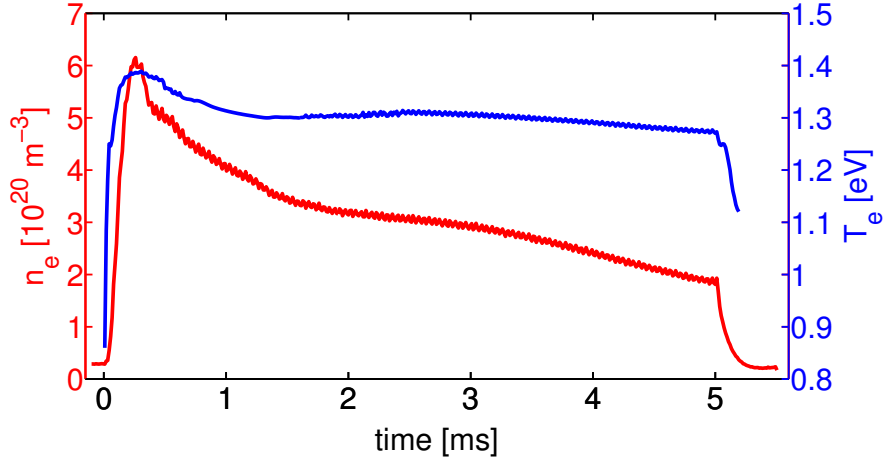
Figure 6.28: Comparison of plasma density and electron temperature at $p_0 = 9\,\mathrm{Pa}$, $B = 105\,\mathrm{mT}$ and $P_\mathrm{RF} = 24\,\mathrm{kW}$.
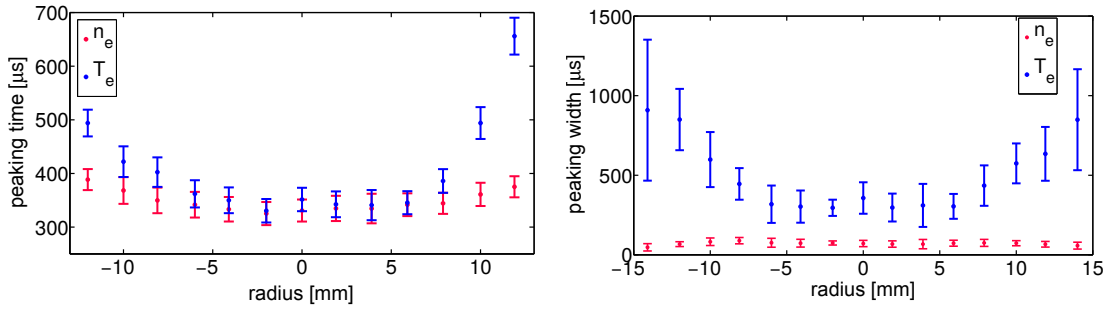
Figure 6.29: Comparison of the plasma density and electron temperature peaking time and width at $p_0 = 9\,\mathrm{Pa}$, $B = 105\,\mathrm{mT}$ and $P_\mathrm{RF} = 9\,\mathrm{kW}$.
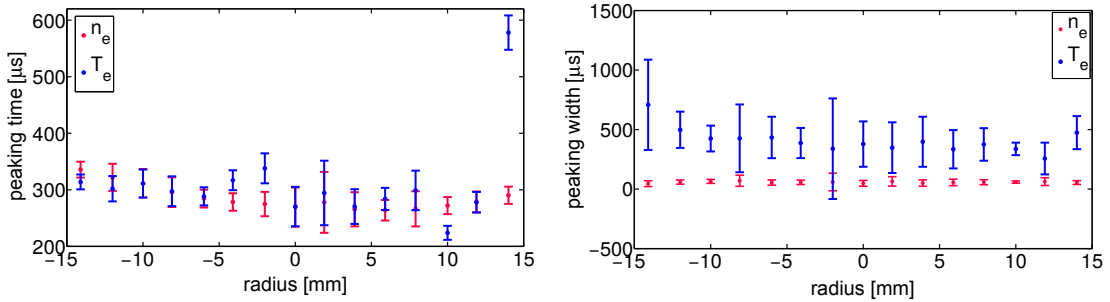
Figure 6.30: Comparison of the plasma density and electron temperature peaking time and width at $p_0 = 9\,\mathrm{Pa}$, $B = 105\,\mathrm{mT}$ and $P_\mathrm{RF} = 24\,\mathrm{kW}$.

6.6 LIF measurements

LIF measurements for neutral and singly ionized argon were conducted (see also section 5.2.2). The time-resolved neutral gas and ion density profile measurements complement the previously evaluated measurements. Figures 6.31 and 6.32 show the argon neutral and ion metastable density profiles obtained with LIF measurements at $p_0 = 9\,\mathrm{Pa}$ and $B = 105\,\mathrm{mT}$ for two different RF powers $P_{\mathrm{RF}} = 9\,\mathrm{kW}$ and $P_{\mathrm{RF}} = 24\,\mathrm{kW}$. The argon neutral metastable density shows for both RF powers a hollow profile with a low density in the center of the discharge. At the edges the neutral argon metastable density is more than three times higher than in the center for the first ms of the discharge. Later between $2 - 4\,\mathrm{ms}$ the density at the edges drops and a flat profile is obtained. For high RF power of $24\,\mathrm{kW}$ the maximum neutral metastable density is more than 30% lower than for low RF power of $9\,\mathrm{kW}$. The argon ion metastable density shows a similar

Figure 6.31: Argon neutral metastable density measured with LIF at $p_0 = 9\,\mathrm{Pa}$, $B = 105\,\mathrm{mT}$ and different RF power.
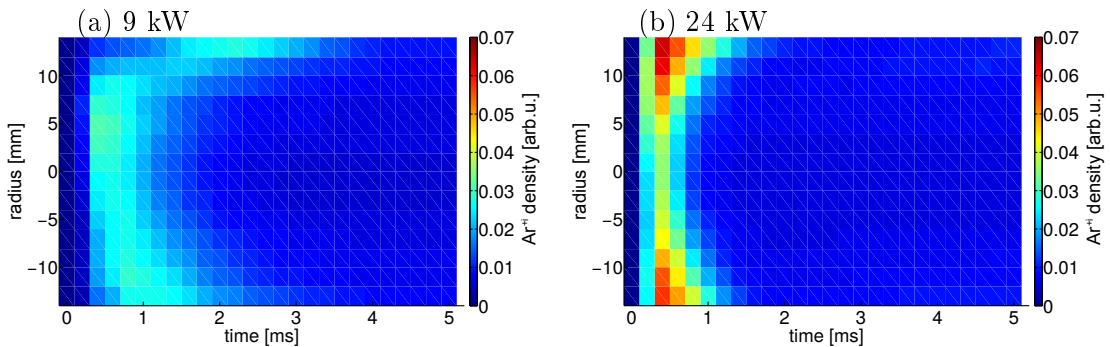
Figure 6.32: Argon ion metastable density measured with LIF at $p_0 = 9\,\mathrm{Pa}$, $B = 105\,\mathrm{mT}$ and different RF power.

behavior for high heating power, with the difference that the metastable ion density in the center is not as much as depleted as for neutral metastable density. The ion metastable density rises for higher heating power $P_{RF} = 24\,\text{kW}$, which results in an increasing ionization rate. For the lower power $P_{RF} = 9\,\text{kW}$ the ion metastable density profile resembles a centrally peaked profile. The hollow profile of ion metastables indicates higher ionization processes or higher damping rates of metastable levels by electron quenching. These processes play an even more important role in the profile evolution of neutral metastable states (section 4.2.2). Neutral depletion can be the cause for hollow profiles. Figures 6.33 and 6.34 show neutral or ion metastable density profiles, obtained with LIF measurements at $p_0 = 2\,\text{Pa}$ with similar magnetic induction and RF power as before. The evolution of argon neutral or ion metastable densities is not changing significantly in comparison to the measurements at $p_0 = 9\,\text{Pa}$. The ion metastable density at
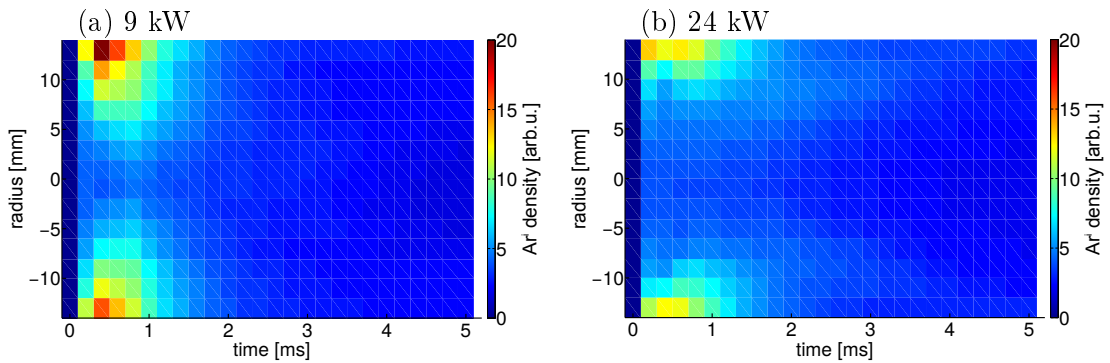

Figure 6.33: Argon neutral metastable density measured with LIF at $p_0 = 2\,\text{Pa}$, $B = 105\,\text{mT}$ and different RF power.
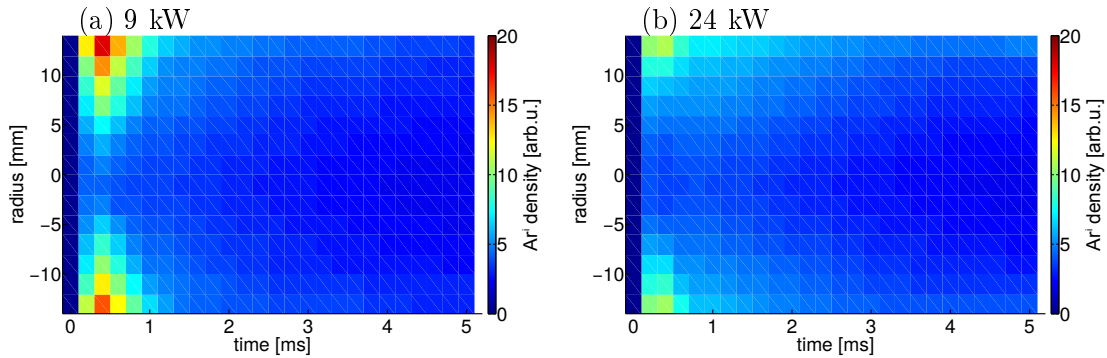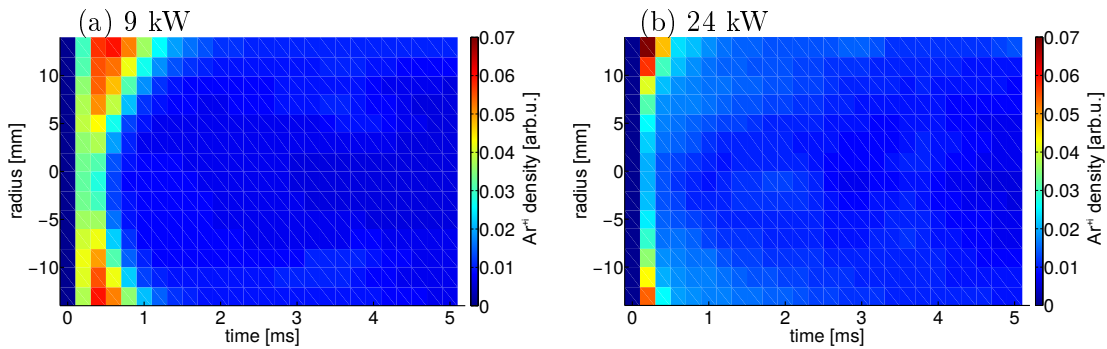

Figure 6.34: Argon ion metastable density measured with LIF at $p_0 = 2\,\text{Pa}$, $B = 105\,\text{mT}$ and different RF power.

low RF power has a hollow profile, what is caused by the highly ionized plasma at low filling gas pressures leading to a higher electron quenching rate also for ion metastables.

To discuss the correlations of density time-evolutions and to investigate the importance of quenching or neutral depletion processes the metastable profile for argon metastable neutrals and ions are not fully sufficient without the knowledge of all dependencies.

6.6.1 Metastable dependencies

As apparent from the distinct dependencies of the metastable argon state Ar^i described in section 4.2.2 the specific state is highly determined by electron temperature and filling neutral gas pressure. In this section LIF measurements are shown for the neutral metastable densities and temperatures for increasing RF power and magnetic induction to get an inkling of the evolution of metastable neutrals for further measurements and calculations.

A fast decline of neutral metastable density is visible in figure 6.35a for measurements at $p_0 = 5\,\mathrm{Pa}$, $B = 55\,\mathrm{mT}$ and varying RF power. The shown neutral metastable densities and temperatures are evaluated in the center of the discharge over the whole discharge as mean value and not taken at a certain time point. Only for low RF powers of $P_{\mathrm{RF}} < 3\,\mathrm{kW}$ a high metastable density is prominent. Higher RF powers exhibit a low neutral metastable density with increasing temperature of Ar^i as the RF power rises, see figure 6.35b. Starting from room temperature at low RF powers the metastable temperature starts to increase as the metastable density reaches a low level for higher RF power. A similar behavior
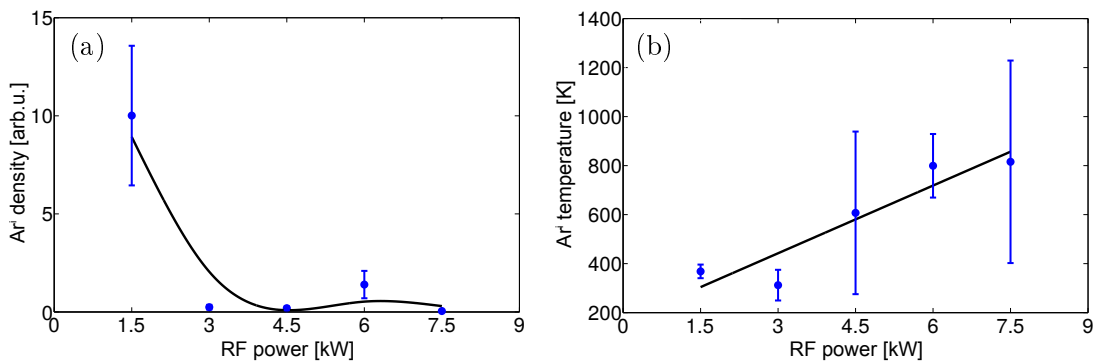
Figure 6.35: Neutral metastable density (a) and temperature (b) for increasing RF power at $p_0 = 5\,\mathrm{Pa}$ and $B = 55\,\mathrm{mT}$ in the center of the discharge.
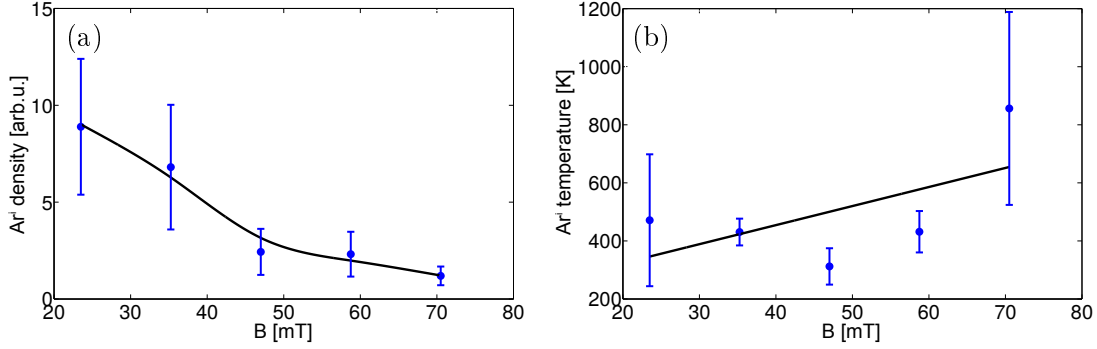
Figure 6.36: Neutral metastable density (a) and temperature (b) for increasing magnetic induction measured at $p_0 = 5\,\mathrm{Pa}$ and $P_{\mathrm{RF}} = 3\,\mathrm{kW}$ in the center of the discharge.

is visible in figure 6.36 for the dependency of the neutral metastable density from the magnetic induction for measurements at $p_0 = 5\,\mathrm{Pa}$ and $P_{\mathrm{RF}} = 3\,\mathrm{kW}$ in total. With increasing magnetic induction the neutral metastable density decreases. Just as the neutral metastable density reaches a low level for high magnetic induction the temperature of the neutral metastables rises.

For both cases a time-resolved measurement was done and is shown in figure 6.37. The measurements show the same behavior as described before considering the time instant of highest neutral metastable densities at the start of the discharge. During the first $500\,\mathrm{\mu s}$ the highest plasma densities and electron temperatures are found as shown in section 6.1.1 and 6.5. As already shown in figure 4.12, the neutral metastable density dependents on the electron temperature. With increasing electron temperature the loss channels (e.g. electron quenching) for the metastable states determine the density evolution (see figure 4.14) and thereby the
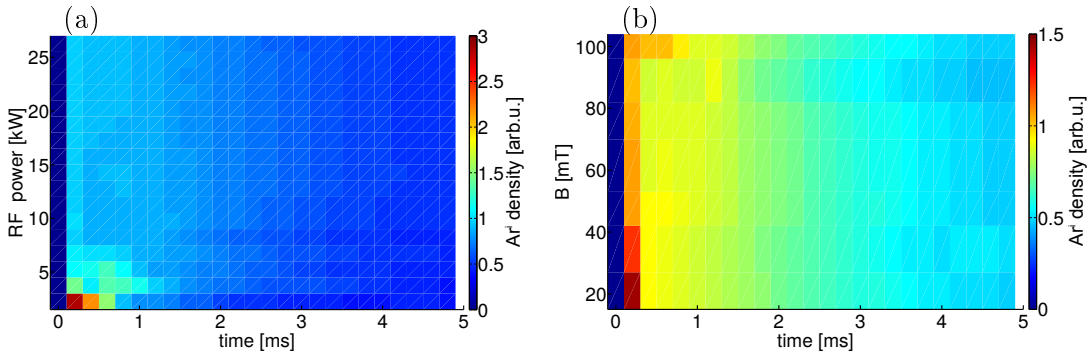
Figure 6.37: Time-resolved neutral metastable density for increasing RF power measured at $p_0 = 5\,\mathrm{Pa}$ and $B = 55\,\mathrm{mT}$ (a), and magnetic field induction measured at $p_0 = 5\,\mathrm{Pa}$ and $P_{\mathrm{RF}} = 3\,\mathrm{kW}$ (b) in the center of the discharge.
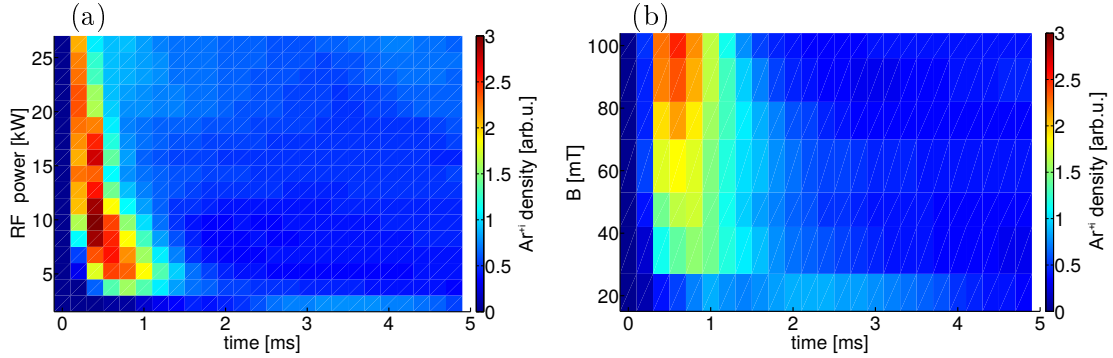
Figure 6.38: Time-resolved ion metastable density for increasing RF power measured at $p_0 = 5\,\mathrm{Pa}$ and $B = 105\,\mathrm{mT}$ (a), and magnetic field induction measured at $p_0 = 5\,\mathrm{Pa}$ and $P_{\mathrm{RF}} = 6\,\mathrm{kW}$ (b) in the center of the discharge.

neutral metastable density, which drops with increasing RF power and magnetic induction. The same measurements were performed for the argon metastable ions but with higher RF power or magnetic induction to obtain higher fluorescence signals. The measurements were performed at $p_0 = 5\,\mathrm{Pa}$ and $B = 105\,\mathrm{mT}$ for varying RF power and at $p_0 = 5\,\mathrm{Pa}$ and $P_{\mathrm{RF}} = 6\,\mathrm{kW}$ for varying magnetic induction and are shown in figure 6.38. Due to an increase of the plasma ionization degree with increasing RF power, magnetic induction and thereby electron temperature (as discussed in section 6.2 and shown in figure 4.13) the metastable ion density of argon rises with increasing RF power and magnetic induction. Furthermore the ion metastable density peaking width and time reduces with increasing RF power and magnetic induction. This happens due to higher plasma densities and temperatures and correspondly lower mean free paths and higher collision frequencies for higher heating power. It is also seen that the peak density for the argon ion metastable state reduces with increasing RF power after a maximum is reached around a heating power of $P_{\mathrm{RF}} \approx 10\,\mathrm{kW}$. This is not found in the diagram shown in figure 4.13, where an increase in metastable ion density is observed. The decreasing peak density indicate higher ionization states than ArII or a higher background noise due to higher RF power that results in a reducing of the total signal.

The argon metastable states have various dependencies on plasma density and electron temperature. Thus, the investigated metastable argon states do not represent the argon ground state. In the next paragraph, the measured plasma density, the calculated electron temperature and the reaction rate model are taken into account to determine the argon neutral and ion ground state density.

6.6.2 Ground state calculations

The argon neutral and ion ground state density are calculated using the reaction rate model (see chapter 4), the measured plasma density, the calculated electron temperature and the argon metastable fluorescence signals as input parameters. For the singly ionized argon ground state all argon ion states (ArII) were summed up. Figure 6.39 shows the time-resolved profile for the argon neutral (a) and ion ground state (b), the evolution of density for the argon neutral (c) and ion ground state (d) in the center of the discharge and the density profile for the argon neutral (e) and ion ground state (f) at the time instant of highest plasma density around $t = 250\,\mu$s (see figure 6.4). The measurements were done at $p_0 = 2\,$Pa, $B = 105\,$mT and $P_{\mathrm{RF}} = 24\,$kW. The neutral density (a) starts at values off scale and decreases quickly to very low densities. The argon ion density (b) starts at zero and increases after the RF-heating is switched on. Notice that both ground state densities are hollow in the center of the discharge (c,d) and no Gaussian-like profile is established in the first millisecond. The highest densities are reached at the edges of the discharge for neutral and singly ionized argon, representing recombination of argon ions and refilling of argon neutrals into the center. The high density regions at the edges in (a) and (b) spread over a longer time interval of $1 - 4\,$ms. Comparing the penetration depths (the ionization mean-free path of both densities) the negative gradient towards the center of the discharge is higher for the argon neutral density than for the ion density. This suggests increased ionization of neutral argon atoms while moving towards the center of the discharge, especially over the first 15 mm. The value corresponds well to the theoretical mean-free path for given plasma densities at low filling gas pressures

$$\lambda = \frac{1}{\sqrt{2}n_{\mathrm{e}}\sigma} = \frac{1}{\sqrt{2} \cdot 2 \cdot 10^{14}\,\mathrm{cm}^{-3} \cdot 2 \cdot 10^{-16}\,\mathrm{cm}^2} \approx 20\,\mathrm{mm}, \qquad (6.1)$$

with σ as cross section for ionization by electron collisions. The evolution of both densities in the center of the discharge (e,f) shows a small refilling effect of neutrals over time with a corresponding increase of the ion density. Particularly at the beginning of the discharge the density profile of the argon ions is not correlating with the plasma density profile (figure 6.4). This indicates higher ionization level than ArII in the starting phase of the discharge. As described in section 6.1.1 the discharge has a peak ionization of over 80% for the case of $p_0 = 2\,$Pa at the start of the discharge. At the ionization degree, higher ionization levels are
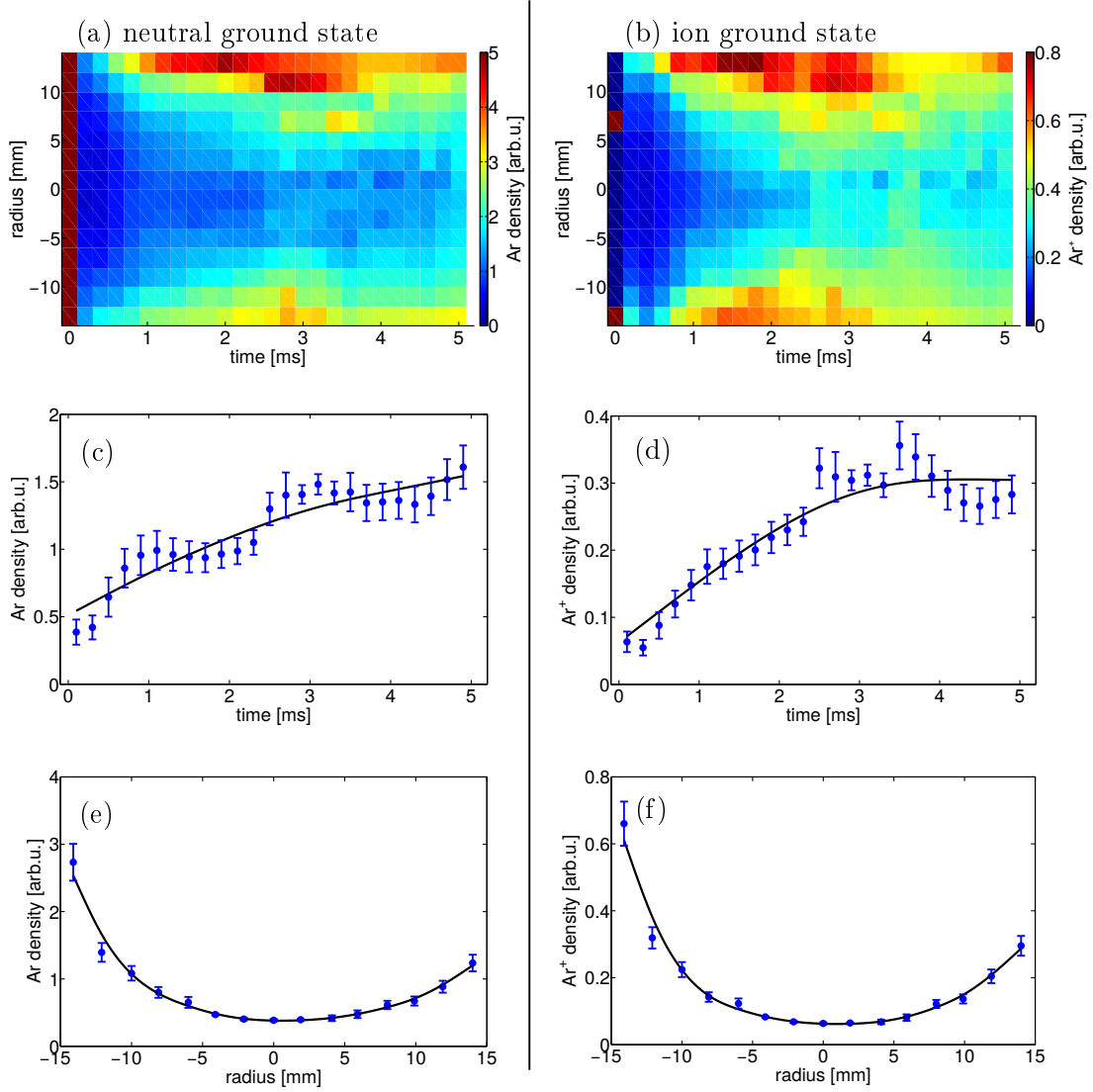
Figure 6.39: Time-resolved profile for argon neutrals (a) and ions (b), the evolution of density in the center of the discharge (c,d) and the density profile at the time instant of highest plasma density around $t = 250\,\mu\text{s}$ (e,f). The measurements were done at $p_0 = 2\,\text{Pa}$, $B = 105\,\text{mT}$ and $P_{\text{RF}} = 24\,\text{kW}$. The data points are shown in blue with their respective error bars. A spline curve is shown in black to indicate the trend. Both ground state densities are hollow.

indeed expected. A different explanation of the increase of argon ion density is the recombination of higher level argon ions due to the low electron temperature over the last 4 ms of the discharge, see figure 6.24. Over the first ms of the discharge high plasma densities and pressure gradients in the center of the discharge result in an increasing loss of charged particles to the axial and radial ends of the discharge. The high plasma density also reduces the ionization mean-free path of argon neutrals that move radially inwards from the wall. This leads to a depletion of argon neutrals in the center of the discharge, resulting in a fast decrease of the plasma density after the neutrals were partially ionized and the density peak was reached. The behavior of edge localized densities and hollow profiles is also observed for measurements at $p_0 = 5 \, \mathrm{Pa}$, $B = 105 \, \mathrm{mT}$ and $P_{\mathrm{RF}} = 24 \, \mathrm{kW}$ (figure 6.40). Figure 6.4 shows correlating measurements at high filling gas pressure and higher peak plasma density. The ionization mean-free path consequently decreases (see equation 6.1) and the neutral argon density reduces due to the higher plasma density and lower ionization mean-free path of neutrals moving inwards. The argon neutral density is lower in the case of $p_0 = 2 \, \mathrm{Pa}$, even at the edge of the discharge, and exhibits a hollow profile. Due to the small ionization mean-free path, the neutral and consequently the ion density at the edge increases slowly over time. The ion ground state displays a hollow profile, even during the first milliseconds with highest plasma densities, suggesting higher ionization levels. The relatively low electron temperatures are however inconsistent with higher ionization levels. In figure 6.41, the argon neutral (a) and ion ground state (b) are shown for the discharges of highest plasma density as investigated in section 6.4. These measurements are done at $p_0 = 9 \, \mathrm{Pa}$, $B = 105 \, \mathrm{mT}$ and
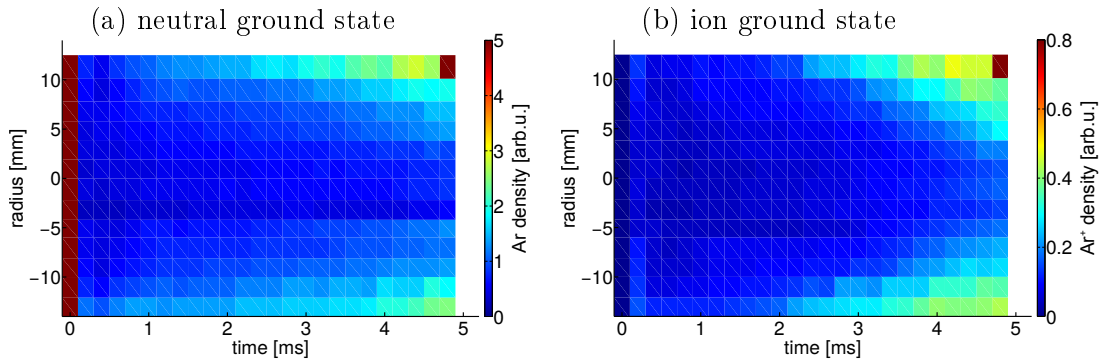
Figure 6.40: Time-resolved profile for argon neutrals (a) and ions (b). The measurements were done at $p_0 = 5 \, \mathrm{Pa}$, $B = 105 \, \mathrm{mT}$ and $P_{\mathrm{RF}} = 24 \, \mathrm{kW}$.

$P_{\mathrm{RF}} = 24\,\mathrm{kW}$. These measurements at higher filling gas pressure result in higher peak and mean plasma densities and temperatures (as discussed in the previous sections). It directly leads to lower neutral argon density levels in comparison to the previous cases (lower filling gas pressure and plasma densities). Hollow profiles over the full discharge time interval are observed for argon neutrals and ions (e,f) with no significant refilling of neutrals or ions (c,d) into the center of the discharge. This is due to the high plasma densities in the center of up to $n_{\mathrm{e}} < 7 \cdot 10^{20}\,\mathrm{m}^{-3}$, resulting in a ionization mean free path of $\lambda \approx 4\,\mathrm{mm}$. The highest densities occur at the start of the discharge at the edge but only for a time interval of $100 - 200\,\mathrm{\mu s}$ and a width of a few millimeter. The time evolution of the neutral density in the center (c) shows a fast decrease at the beginning of the discharge, followed by a stagnation on a relatively low density level. At the end of the discharge a fast increase occurs due to recombination of ions. For argon ions (d) a first peak is visible at the start of the discharge, followed by a decrease to a low level density. At the end of the discharge the ion density increases. The first peak and the increase in ion density at the end of the discharge are an indication of higher level ionization. At first ArII is ionized, which results in a peaking and a low ion density level. At the end of the discharge the higher level ions recombinate back to ArII, resulting in an increase of the ion density. This behavior is not seen in figure 6.39. This is due to the low electron temperatures resulting in recombination before the discharge ends.
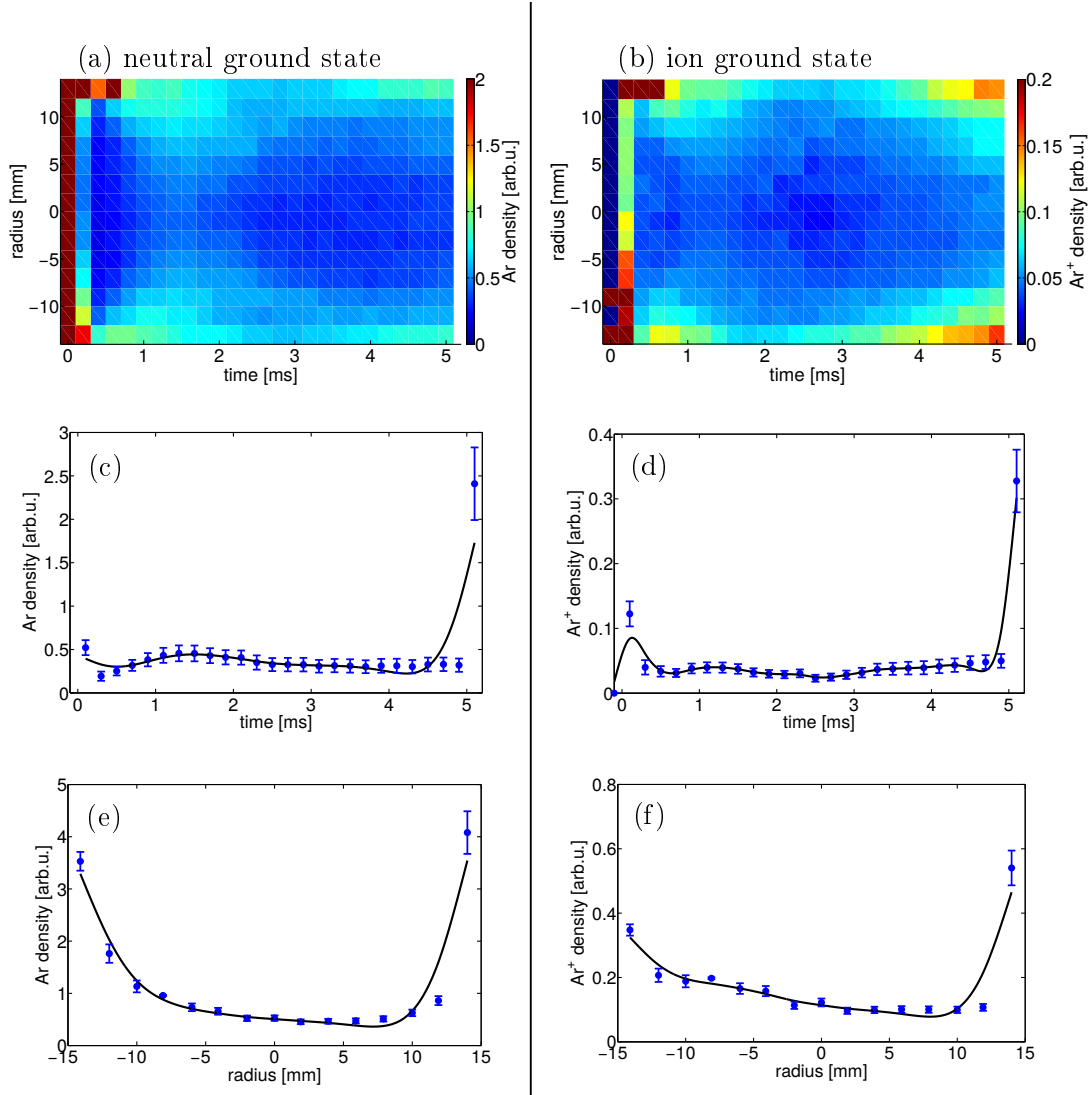
Figure 6.41: Time-resolved profile for argon neutrals (a) and ions (b), the evolution of density in the center of the discharge (c,d) and the density profile at the time instant of highest plasma density around $t = 250\,\mu s$ (e,f). The measurements were done at $p_0 = 9\,\mathrm{Pa}$, $B = 105\,\mathrm{mT}$ and $P_{\mathrm{RF}} = 24\,\mathrm{kW}$. The data points are shown in blue with their respective error bars. A spline curve is shown in black to indicate the trend. Both ground state densities are hollow over the whole discharge.

6.7 Correlation of ion and plasma density

In this section a direct comparison of the calculated argon ion ground state and the plasma densities is made for various filling neutral gas pressures. For measurements at $B = 105\,\mathrm{mT}$ and $P_{\mathrm{RF}} = 9\,\mathrm{kW}$ or $P_{\mathrm{RF}} = 24\,\mathrm{kW}$ ion ground state and plasma densities are shown together in figure 6.42 or 6.43, respectively. Assuming a low temperature plasma consisting of electrons and singly ionized argon and a small fraction of ArIII, the time-resolved profile calculations of the argon ion density provide the profile evolution of the plasma density. Comparing the argon ion and the plasma density a contradiction between measurement and calculation occurs. A hollow profile is found for various parameters. The evolution of the ion density is clearly different from the plasma density for various parameters like filling gas pressure or RF power. The first peak in the plasma density over the first millisecond does not occur in the evolution of the ion density, as already discussed in the previous section 6.6.2. At high filling neutral gas pressures (c,d) the highest ion densities are found at the start of the discharge together with high plasma densities. The ion densities increase with increasing gas pressure. For high filling neutral gas pressure, the number of particles is more than sufficient to sustain a constant ionization rate, even for higher ionization levels. A significant density of ArII is measured at the starting phase of the discharge for high plasma densities and electron temperatures. In regions of lower plasma densities towards the end of the discharge (therefore lower electron temperatures), the ion density rises again (a,b,c). It represents recombination effects of ions or an ionization of refilled neutrals moving towards the center. With higher filling gas pressure, the ionization of refilling neutrals is higher due to the decreasing ionization mean free path. The difference in argon ion and plasma density is explainable by a higher ionization level than just ArII in the starting phase of the discharge or as a result of an incomplete model that does not represent a plasma discharge under the given experimental conditions. With increasing filling gas pressure higher peak plasma densities and higher electron temperatures are reached. At these increasing parameter values, the ion density decreases, suggesting higher ionization levels. A higher axial loss of particles with increasing gas pressure also has an impact, but is not investigated here. The limited resolution of the time-resolved LIF measurements can also be a reason why the first peak of high ion density is not visible. As discussed in section 5.2.2, a higher resolution results in a fast increase of measurement time since the integration time is kept nearly constant.

Figure 6.42: Time-resolved profiles for argon ion ground state densities (left) and plasma densities (right) for filling neutral gas pressures of $2\,\mathrm{Pa}$ (a), $5\,\mathrm{Pa}$ (b), $9\,\mathrm{Pa}$ (c) and $13\,\mathrm{Pa}$ (d). The measurements were done at $B = 105\,\mathrm{mT}$ and $P_{\mathrm{RF}} = 9\,\mathrm{kW}$.
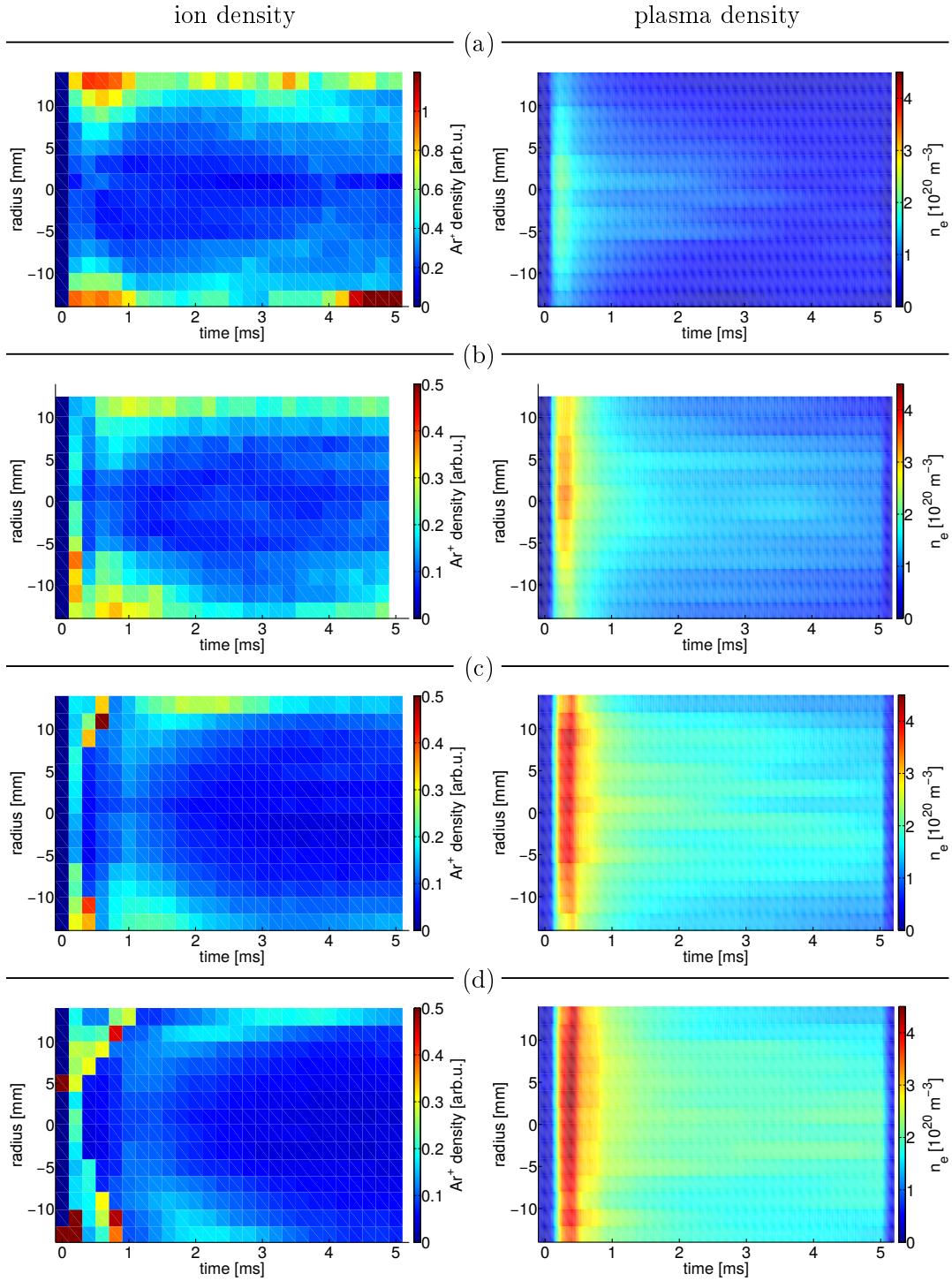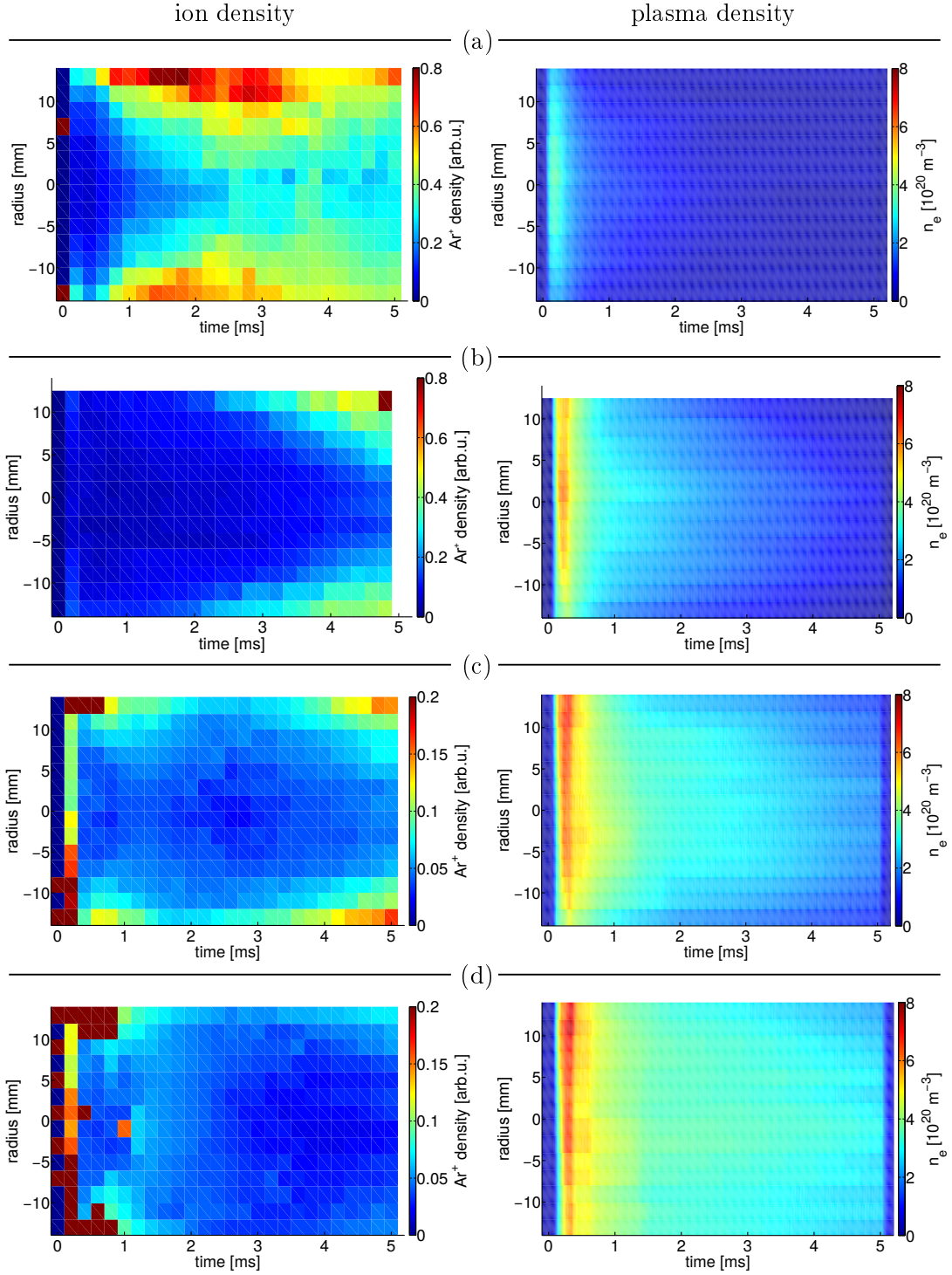
Figure 6.43: Time-resolved profiles for argon ion ground state density (left) and plasma density (right) for filling neutral gas pressures of 2 Pa (a), 5 Pa (b), 9 Pa (c) and 13 Pa (d). The measurements were done at $B = 105\,\text{mT}$ and $P_{\text{RF}} = 24\,\text{kW}$.

Chapter 7

Summary

In the present work high density helicon plasma discharges are created and characterized as a promising concept towards the realization of plasma wakefield accelerators to build up electric fields in the order of GV/m to accelerate electrons to energies in the TeV range with proton driving bunches. For such a concept plasma sources are needed that are able to maintain discharges with plasma densities of $n_e \geq 7{\cdot}10^{20}\,\mathrm{m}^{-3}$ over long distances with a low variation in plasma density. Measurements at the PROMETHEUS-A device are performed for variable parameters, like magnetic induction, RF heating power and filling gas pressure. A CO_2 laser interferometer, a laser induced fluorescence diagnostic and a reaction rate model are combined to give a consistent picture. It is shown that in most cases the plasma density is centrally peaked with a high density region $\pm 5\,\mathrm{mm}$ from the center. The peak plasma density increases with increasing filling gas pressure, RF heating power and magnetic induction, limited by the number of neutral particles in low pressure discharges, by the transferred heating power and the increasing recombination and electron quenching rates of argon ions in high filling pressure cases. The increase in plasma density with increasing magnetic induction correlates to the direct proportionality in the helicon dispersion relation. For all investigated operational parameters the time evolution of the helicon discharge shows the same characteristics and is reliably reproducable inside the error bars. The electron temperature is determined by combining the collisional radiative model with line ratio measurements of two spontaneously emitted LIF lines. The low electron temperature regime of $1.2\,\mathrm{eV} < T_e < 1.4\,\mathrm{eV}$ and the electron temperature profiles are consistent with helicon wave heating via collisional power

dissipation. The maximum plasma density of $n_e = 6 \pm 1 \cdot 10^{20}\,\mathrm{m}^{-3}$ is measured at high RF power of $P_{\mathrm{RF}} = 24\,\mathrm{kW}$, $p_0 = 9\,\mathrm{Pa}$ filling gas pressure and a magnetic induction of $B = 105\,\mathrm{mT}$ with a maximum electron temperature at $1.4\,\mathrm{eV}$. At these operational parameters the plasma density peaking time and width are determined to be $270\,\mathrm{\mu s}$ and $50\,\mathrm{\mu s}$, respectively. This shows that the specific plasma density requirements for the use of a wakefield accelerator are reachable and the duration of the peak plasma density is sufficient for a relativistic particle to pass a $1\,\mathrm{km}$ long plasma cell. Time-resolved LIF profile measurements for neutral and singly ionized argon were conducted to complement the previously evaluated measurements. The time resolution of the LIF diagnostic was chosen in a way to adequately represent the evolution of densities and to allow full profile measurements over one day. A resolution of $\Delta t = 200\,\mathrm{\mu s}$ was chosen. The time-resolved neutral and ion metastable densities show hollow profiles with high densities at the edges over the first ms indicating higher ionization levels and increasing electron quenching rates. The metastable densities are highly determined by electron temperature, RF heating power and filling neutral gas pressure and do not reflect the neutral argon evolution. To investigate the influence of neutral depletion on the density evolution and maximum plasma density, the argon neutral and ion ground state densities are determined. Both time-resolved density profiles show a hollow profile with highest densities at the edges over a longer time interval of $3-4\,\mathrm{ms}$. The penetration depths (ionization mean-free paths) indicate increased ionization of neutral argon while dissipating inwards, corresponding well to the theoretical value of $\lambda = 20\,\mathrm{mm}$. This results in a depletion of neutrals in the center of the discharge, leading to a limitation and a fast decrease of plasma density after the neutrals are partially ionized. The shown refilling effect of neutral argon is too slow to have an important impact. At operation parameters for highest plasma density, the calculated ground states also show a fast increase in density at the end of the discharge after the RF-heating is switched off. This indicates recombination effects to these atomic states and higher ionization levels than ArII in the helicon discharge.

Appendix

Included reactions and corresponding reaction rates

	Reaction	Sort of atom	Reaction rate coefficient		label
ionization	$Ar + e \rightarrow Ar^+ + e + e$		$1.5912 \cdot 10^{-8} \sqrt{\frac{T_e}{1eV}} \left(1 + \frac{T_e}{1eV}\right) \exp\left(-\frac{14.612eV}{T_e}\right)$ cm^3/s	[1990b][LANLb][LANLa]	k_1
	$Ar^i + e \rightarrow Ar^+ + e + e$		$1.7412 \cdot 10^{-8} \sqrt{\frac{T_e}{1eV}} \left(1 + \frac{T_e}{1eV}\right) \exp\left(-\frac{4.132eV}{T_e}\right)$ cm^3/s	[1990b][LANLb][LANLa]	k_2
	$Ar^e + e \rightarrow Ar^+ + e + e$		$3.2244 \cdot 10^{-8} \sqrt{\frac{T_e}{1eV}} \left(1 + \frac{T_e}{1eV}\right) \exp\left(-\frac{2.2716eV}{T_e}\right)$ cm^3/s	[1990b][LANLb][LANLa]	k_3
	$Ar^f + e \rightarrow Ar^+ + e + e$		$3.5676 \cdot 10^{-9} \sqrt{\frac{T_e}{1eV}} \left(1 + \frac{T_e}{1eV}\right) \exp\left(-\frac{3.956eV}{T_e}\right)$ cm^3/s	[1990b][LANLb][LANLa]	k_4
	$Ar^i + e \rightarrow Ar^{+f} + e + e$		$7.8485 \cdot 10^{-10} \sqrt{\frac{T_e}{1eV}} \left(1 + \frac{T_e}{1eV}\right) \exp\left(-\frac{20.768eV}{T_e}\right)$ cm^3/s	[1990b][LANLb][LANLa]	k_5
	$Ar^f + e \rightarrow Ar^{+f} + e + e$		$8.8973 \cdot 10^{-11} \sqrt{\frac{T_e}{1eV}} \left(1 + \frac{T_e}{1eV}\right) \exp\left(-\frac{20.593eV}{T_e}\right)$ cm^3/s	[1990b][LANLb][LANLa]	k_6
el. coll. excitation	$Ar + e \rightarrow Ar^i + e$		$3.799 \cdot 10^{-10} \sqrt{\frac{T_e}{1eV}} \left(1 + \frac{T_e}{1eV}\right) \exp\left(-\frac{11.416eV}{T_e}\right)$ cm^3/s	[1990b][LANLb][LANLa]	k_7
	$Ar + e \rightarrow Ar^e + e$		$6.4788 \cdot 10^{-10} \sqrt{\frac{T_e}{1eV}} \left(1 + \frac{T_e}{1eV}\right) \exp\left(-\frac{13.326eV}{T_e}\right)$ cm^3/s	[1990b][LANLb][LANLa]	k_8
	$Ar + e \rightarrow Ar^f + e$		$9.4485 \cdot 10^{-10} \sqrt{\frac{T_e}{1eV}} \left(1 + \frac{T_e}{1eV}\right) \exp\left(-\frac{11.565eV}{T_e}\right)$ cm^3/s	[1990b][LANLb][LANLa]	k_9
recombination	$Ar^+ + e \rightarrow Ar$		$4.3 \cdot 10^{-12}$ cm^3/s	[Wanless, 1971]	k_{10}
metastable pooling	$Ar^x + Ar^y \rightarrow Ar^+ + Ar + e$	$x = i,e,f, x = y$	$6.2 \cdot 10^{-10}$ cm^3/s	[Lee, 1995]	k_{11}
	$Ar^x + Ar^x \rightarrow Ar + Ar^{xx}$	$x = i,e,f$	$1 \cdot 10^{-10}$ cm^3/s	estimated	k_{12}
	$Ar^x + Ar \rightarrow Ar + Ar$	$x = i,e,f$	$2.3 \cdot 10^{-15}$ cm^3/s	[Stefanović]	k_{13}
electron quenching	$Ar^x + e \rightarrow Ar + e$	$x = i,e,f$	$2 \cdot 10^{-7}$ cm^3/s	[Stefanović][Lee, 1995][Shimada]	k_{14}
spontaneous emission	$Ar^e \rightarrow h\nu + Ar^i$		$2.36 \cdot 10^5$ s^{-1}	[NIST]	k_{15}
	$Ar^e \rightarrow h\nu + Ar^f$		$4.45 \cdot 10^7$ s^{-1}	[NIST]	k_{16}
	$Ar^i \rightarrow h\nu + Ar$		$1.19 \cdot 10^8$ s^{-1}	[NIST]	k_{17}
	$Ar^f \rightarrow h\nu + Ar$		$5.1 \cdot 10^8$ s^{-1}	[NIST]	k_{18}
penning ionization	$Ar^x + Ar^y \rightarrow Ar^+ + Ar + e$	$x = i,e,f, x \neq y$	$5 \cdot 10^{-10}$ cm^3/s	[Lam][Elson, 1996]	k_{19}
excited state kinetics	$Ar^e + Ar \rightarrow Ar^f + Ar$		$1 \cdot 10^{-10}$ cm^3/s	[Kannari et al., 1985]	k_{19}
three body collisions	$Ar^+ + 2e \rightarrow Ar + e$	$x = i,e,f$	$1.019 \cdot 10^{-29}$ cm^6/s	[Lee, 1995]	k_{20}
	$Ar^x + Ar + Ar \rightarrow Ar + Ar + Ar$	$x = g,i,e,f$	$1.5 \cdot 10^{-32}$ cm^6/s	[Lee, 1995]	k_{21}
	$Ar^+ + e + Ar^{xx} \rightarrow Ar + Ar^{xx}$		$1 \cdot 10^{-26}$ cm^6/s	[Lee, 1995]	k_{22}
	$Ar^+ + e + e \rightarrow Ar^i + e$		$2.1 \cdot 10^{-28} \cdot \left(\frac{T_e}{1eV}\right)^{-9/2}$ cm^6/s	[Lawless, 1995]	k_{23}
	$Ar^+ + e + e \rightarrow Ar^f + e$		$2.1 \cdot 10^{-27} \cdot \left(\frac{T_e}{1eV}\right)^{-9/2}$ cm^6/s	[Lawless, 1995]	k_{24}
wall interaction	$Ar^x + wall \rightarrow Ar$	$x = i,e,f$	$1.3427 \cdot 10^4$ s^{-1}	[Lee, 1995][2001][Lieberman]	$k_{w(met)}$

Table 8.1: Reactions with neutral argon.

	Reaction	Sort of atom	Reaction rate coefficient		label
ionization	$Ar^+ + e \rightarrow Ar^{++} + e + e$		$1.4883 \cdot 10^{-9} \sqrt{\frac{T_e}{1eV}} \left(1 + \frac{27.488eV}{T_e}\right) \exp\left(-\frac{27.488eV}{T_e}\right)$ cm³/s	[1990b][LANLb][LANLa]	k_{25}
	$Ar^{+i} + e \rightarrow Ar^{++} + e + e$		$2.5609 \cdot 10^{-9} \sqrt{\frac{T_e}{1eV}} \left(1 + \frac{9.7846eV}{T_e}\right) \exp\left(-\frac{9.7846eV}{T_e}\right)$ cm³/s	[1990b][LANLb][LANLa]	k_{26}
	$Ar^{+e} + e \rightarrow Ar^{++} + e + e$		$4.4447 \cdot 10^{-9} \sqrt{\frac{T_e}{1eV}} \left(1 + \frac{8.0558eV}{T_e}\right) \exp\left(-\frac{8.0558eV}{T_e}\right)$ cm³/s	[1990b][LANLb][LANLa]	k_{27}
	$Ar^{+f} + e \rightarrow Ar^{++} + e + e$		$1.0817 \cdot 10^{-9} \sqrt{\frac{T_e}{1eV}} \left(1 + \frac{10.805eV}{T_e}\right) \exp\left(-\frac{10.805eV}{T_e}\right)$ cm³/s	[1990b][LANLb][LANLa]	k_{28}
el. coll. excitation	$Ar^+ + e \rightarrow Ar^{+i} + e$		$4.5035 \cdot 10^{-10} \sqrt{\frac{T_e}{1eV}} \left(1 + \frac{17.6948eV}{T_e}\right) \exp\left(-\frac{17.6948eV}{T_e}\right)$ cm³/s	[1990b][LANLb][LANLa]	k_{29}
	$Ar^+ + e \rightarrow Ar^{+e} + e$		$1.0588 \cdot 10^{-10} \sqrt{\frac{T_e}{1eV}} \left(1 + \frac{19.549eV}{T_e}\right) \exp\left(-\frac{19.549eV}{T_e}\right)$ cm³/s	[1990b][LANLb][LANLa]	k_{30}
	$Ar^+ + e \rightarrow Ar^{+f} + e$		$1.4984 \cdot 10^{-10} \sqrt{\frac{T_e}{1eV}} \left(1 + \frac{16.7486eV}{T_e}\right) \exp\left(-\frac{16.7486eV}{T_e}\right)$ cm³/s	[1990b][LANLb][LANLa]	k_{31}
	$Ar^{+i} + e \rightarrow Ar^{+e} + e$		$2.6874 \cdot 10^{-8} \sqrt{\frac{T_e}{1eV}} \left(1 + \frac{1.8543eV}{T_e}\right) \exp\left(-\frac{1.8543eV}{T_e}\right)$ cm³/s	[1990b][LANLb][LANLa]	k_{32}
penning ionization	$Ar^{++} + Ar \rightarrow Ar^{++} + Ar^+ + e$		$2.0746 \cdot 10^{-9} \sqrt{\frac{T_e}{1eV}} \left(1 + \frac{15.6eV}{T_e}\right) \exp\left(-\frac{15.6eV}{T_e}\right)$ cm³/s	[1990b][Puerta, 1985]	k_{33}
	$Ar^{+x} + Ar^x \rightarrow Ar^{++} + Ar + e$	$x = i,e,f$	$5.2200 \cdot 10^{-9} \sqrt{\frac{T_e}{1eV}} \left(1 + \frac{1eV}{T_e}\right) \exp\left(-\frac{1eV}{T_e}\right)$ cm³/s	[1990b][Jones et al., 1959]	k_{34}
metastable pooling	$Ar^{++} + Ar \rightarrow Ar^+ + Ar^+$		$1.3385 \cdot 10^{-9} \sqrt{\frac{T_e}{1eV}} \left(1 + \frac{1eV}{T_e}\right) \exp\left(-\frac{1eV}{T_e}\right)$ cm³/s	[1990b][Puerta, 1985]	k_{35}
	$Ar^{++} + Ar \rightarrow Ar^{+i} + Ar^+$		$1.3385 \cdot 10^{-9} \sqrt{\frac{T_e}{1eV}} \left(1 + \frac{5.8eV}{T_e}\right) \exp\left(-\frac{5.8eV}{T_e}\right)$ cm³/s	[1990b][Puerta, 1985]	k_{36}
	$Ar^{++} + Ar \rightarrow Ar^{+e} + Ar^+$		$1.3385 \cdot 10^{-9} \sqrt{\frac{T_e}{1eV}} \left(1 + \frac{7.7eV}{T_e}\right) \exp\left(-\frac{7.7eV}{T_e}\right)$ cm³/s	[1990b][Puerta, 1985]	k_{37}
	$Ar^{++} + Ar \rightarrow Ar^{+f} + Ar^+$		$1.3385 \cdot 10^{-9} \sqrt{\frac{T_e}{1eV}} \left(1 + \frac{4.7eV}{T_e}\right) \exp\left(-\frac{4.7eV}{T_e}\right)$ cm³/s	[1990b][Puerta, 1985]	k_{38}
	$Ar^{++} + Ar^x \rightarrow Ar^{+x} + Ar^+$	$x = i,e,f$	$2.0077 \cdot 10^{-9} \sqrt{\frac{T_e}{1eV}} \left(1 + \frac{1eV}{T_e}\right) \exp\left(-\frac{1eV}{T_e}\right)$ cm³/s	[1990b][Puerta, 1985]	k_{39}
recombination	$Ar^{+x} + e \rightarrow Ar$	$x = i,e,f$	$8.6 \cdot 10^{-12}$ cm³/s	estimated	k_{40}
	$Ar^{++} + e \rightarrow Ar^+$		$4.3 \cdot 10^{-11}$ cm³/s	[2007]	k_{41}
spontaneous emission	$Ar^{+e} \rightarrow h\nu + Ar^{+f}$		$8.17 \cdot 10^7$ s⁻¹	[NIST]	k_{42}
	$Ar^{+e} \rightarrow h\nu + Ar^{+i}$		$1.07 \cdot 10^7$ s⁻¹	[NIST]	k_{43}
	$Ar^{+e} \rightarrow h\nu + Ar^+$		$4.02 \cdot 10^7$ s⁻¹	[NIST]	k_{44}
	$Ar^{+f} \rightarrow h\nu + Ar^+$		$3.1 \cdot 10^7$ s⁻¹	[NIST]	k_{45}
excited state kinetics	$Ar^{+x} + Ar \rightarrow Ar^+ + Ar$	$x = i,e,f$	$2.5 \cdot 10^{-10}$ cm³/s	[Belikov et al., 1995]	k_{46}
wall interaction	$Ar^{+x} + wall \rightarrow Ar$	$x = g,i,e,f$	$A \cdot 2.9602 \cdot 10^5 \sqrt{\frac{T_e}{1eV}}$ s⁻¹	[Lee, 1995][2001][Lieberman]	$k_{w(charge)}$
	$Ar^{++} + wall \rightarrow Ar$		$A \cdot 2.9602 \cdot 10^5 \sqrt{\frac{T_e}{1eV}}$ s⁻¹	[Lee, 1995][2001][Lieberman]	$k_{w(charge)}$

Table 8.2: Reactions with singly ionized argon.

	Reaction	Sort of atom	Reaction rate coefficient		label
dimer and trimer formation	$Ar^+ + Ar + Ar \rightarrow Ar_2^+ + Ar$	$x=i,e,f$	$2.5\cdot10^{-31}\left(\frac{300}{T_G}\right)^{\frac{3}{2}}$ cm^6/s	[Neeser][Lam]	k_{47}
	$Ar^x + Ar \rightarrow Ar_2^+ + e$		$3.2\cdot10^{-10}$ cm^3/s	[Franklin][Dahler et al., 1962]	k_{48}
	$Ar_2^+ + Ar + Ar \rightarrow Ar_3^+ + Ar$		$7.0\cdot10^{-32}\left(\frac{300}{T_G}\right)^{\frac{3}{2}}$ cm^6/s	[Neeser][Turner, 1979][Lam]	k_{49}
	$Ar^e + Ar + Ar \rightarrow Ar_2^e + Ar$		$2.5\cdot10^{-32}$ cm^6/s	[Lam]	k_{50}
	$Ar^i + Ar + Ar \rightarrow Ar_2^i + Ar$		$\frac{1\cdot10^{-32}}{\left(1+6\cdot10^4\frac{n_e}{n_{Ar}}\right)}$ cm^6/s	[Neeser][Lam]	k_{51}
	$Ar^f + Ar + Ar \rightarrow Ar_2^f + Ar$		$\frac{1\cdot10^{-32}}{\left(1+6\cdot10^4\frac{n_e}{n_{Ar}}\right)}$ cm^6/s	[Neeser][Lam]	k_{52}
ionization	$Ar_2^e + e \rightarrow Ar_2^+ + e + e$		$3\cdot10^{-6}\left(\frac{T_e}{1eV}\right)^{-\frac{6}{2}}\exp\left(-\frac{3.75eV}{T_e}\right)$ cm^3/s	[Lawless, 1995]	k_{53}
	$Ar_2^x + e \rightarrow Ar_2^+ + e + e$	$x=i,f$	$6.26\cdot10^{-6}\left(\frac{T_e}{1eV}\right)^{-\frac{6}{2}}\exp\left(-\frac{3.75eV}{T_e}\right)$ cm^3/s	[Lawless, 1995]	k_{54}
recombination	$Ar_2^+ + e + e \rightarrow Ar_2^x + e$	$x=i,f$	$1\cdot10^{-27}\left(\frac{T_e}{1eV}\right)^{-\frac{9}{2}}$ cm^6/s	[Lawless, 1995]	k_{55}
collisional dissociation	$Ar_3^+ + e \rightarrow Ar^e + Ar + Ar$	$x=i,f$	$1.3\cdot10^{-5}\left(\frac{T_e}{1eV}\right)^{-\frac{1}{2}}$ cm^3/s	[Lawless, 1995]	k_{56}
	$Ar_3^+ + e \rightarrow Ar^x + Ar + Ar$		$1.6\cdot10^{-7}\left(\frac{T_e}{1eV}\right)^{-0.54}$ cm^3/s	[Elson, 1996][Neeser]	k_{57}
	$Ar_3^+ + Ar \rightarrow Ar_2^+ + Ar + Ar$		$3.5\cdot10^{-12}$ cm^3/s	[Neeser]	k_{58}
	$Ar_2^+ + e \rightarrow Ar^e + Ar$	$x=i,f$	$2\cdot10^{-7}\left(\frac{T_e}{1eV}\right)^{-\frac{1}{2}}$ cm^3/s	[Lawless, 1995]	k_{59}
	$Ar_2^x + e \rightarrow Ar + Ar + e$		$1\cdot10^{-7}\exp\left(-\frac{1eV}{T_e}\right)$ cm^3/s	estimated	k_{60}
	$Ar_2^i + e \rightarrow Ar^i + Ar + e$		$1\cdot10^{-8}\exp\left(-\frac{1eV}{T_e}\right)$ cm^3/s	[Neeser]	k_{61}
	$Ar_2^f + e \rightarrow Ar^f + Ar + e$		$1\cdot10^{-8}\exp\left(-\frac{1eV}{T_e}\right)$ cm^3/s	[Neeser]	k_{62}
	$Ar_2^+ + Ar \rightarrow Ar^+ + Ar + Ar$	$x=i,e,f$	$1\cdot10^{-11}$ cm^3/s	estimated with [Stephan, 1985] [Gochelashvily et al., 1992]	k_{63}
	$Ar_2^e + Ar \rightarrow Ar^x + Ar + Ar$	$x=i,e,f$	$1\cdot10^{-11}$ cm^3/s		k_{64}
	$Ar_2^x + Ar_2^x \rightarrow Ar_2^+ + Ar + Ar + Ar$	$x=i,e,f$	$1.266\cdot10^{-10}$ cm^3/s	[Thompson, 1982]	k_{65}
	$Ar_2^x + Ar_2^x \rightarrow Ar^+ + Ar + Ar + Ar + Ar$	$x=i,e,f$	$2.267\cdot10^{-10}$ cm^3/s	[Thompson, 1982]	k_{66}
	$Ar_2^x + Ar_2^x \rightarrow Ar_3^+ + Ar$	$x=i,e,f$	$2.56\cdot10^{-11}$ cm^3/s	[Thompson, 1982]	k_{67}
spontaneous dissociation	$Ar_2^+ \rightarrow Ar + Ar^+$		$2.5\cdot10^{-31}\left(\frac{300}{T_G}\right)^{\frac{3}{2}}$ cm^6/s $\cdot n_{Ar}^2$	estimated with [Stephan, 1985]	k_{68}
	$Ar_2^e \rightarrow h\nu + Ar + Ar$		$3.13\cdot10^9$ s^{-1}	[Lam]	k_{69}
	$Ar_2^x \rightarrow h\nu + Ar + Ar$		$2.38\cdot10^8$ s^{-1}	[Lam]	k_{70}
el. coll. excitation	$Ar_2^x + e \rightarrow Ar_2^e + e$	$x=i,f$	$5\cdot10^{-8}$ cm^3/s	estimated	k_{71}
penning ionization	$Ar_2^x + Ar_2^x \rightarrow Ar_2^+ + Ar + Ar + e$	$x=i,e,f$	$5\cdot10^{-10}$ cm^3/s	[Lam][Kannari et al., 1985]	k_{72}
	$Ar^x + Ar^x \rightarrow Ar_2^+ + e$	$x=i,e,f$	$5\cdot10^{-10}$ cm^3/s	[Lam]	k_{73}
	$Ar_2^x + Ar_2^x \rightarrow Ar_2^+ + Ar + e$	$x=i,e,f$	$6\cdot10^{-10}$ cm^3/s	[Lam][Neeser]	k_{74}
wall interaction	$Ar_2^x + wall \rightarrow Ar + Ar$	$x=i,e,f$	$0.9494\cdot10^4$ s^{-1}	[Lee, 1995][2001][Lieberman]	$k_{w(di)}$
	$Ar_2^+ + wall \rightarrow Ar + Ar$		$A\cdot2.0932\cdot10^5\sqrt{\frac{T}{1eV}}$ s^{-1}	[Lee, 1995][2001][Lieberman]	$k_{w(dicharged)}$
	$Ar_3^+ + wall \rightarrow Ar + Ar + Ar$		$A\cdot1.7091\cdot10^5\sqrt{\frac{T}{1eV}}$ s^{-1}	[Lee, 1995][2001][Lieberman]	$k_{w(tricharged)}$

Table 8.3: Reactions with argon dimers and trimers.

Bibliography

[Abdalla, 2004] Abdalla, M. A. A. (2004). *Temperature and Density Measurements at an Inductively RF Excited Hydrogen Plasma Discharge*. PhD thesis, Universität Duisburg-Essen.

[Abel, 1826] Abel, N. (1826). Auflösung einer mechanischen Aufgabe. *Journal für die reine und angewandte Mathematik*, 1:153–157.

[Adli et al., 2018] Adli, E. et al. (2018). Acceleration of electrons in the plasma wakefield of a proton bunch. *Nature*, 561:363–367.

[Aicheler et al., 2012] Aicheler, M. et al. (2012). A multi-tev linear collider based on clic technology: Clic conceptual design report. CERN-2012-007 (CERN, Geneva, 2012). Accessed: 2018-11-28.

[Akhiezer, 1956] Akhiezer, A. and Polovin, R. (1956). Theory of wave motion of an electron plasma. *Sov. Phys. JETP*, 3:696.

[APS, 2017] American Physical Society. APS news: Particle physicists gather to plan next accelerator. `https://www.aps.org/publications/apsnews/updates/accelerator.cfm`. Accessed: 2017-12-20.

[2012] Annaloro, J., Morel, V., Bultel, A., and Omaly, P. (2012). Global rate coefficients for ionization and recombination of carbon, nitrogen, oxygen, and argon. *Physics of Plasmas*, 19(7):073515.

[Assmann et al., 2014] Assmann, R. et al. (2014). Proton-driven plasma wakefield acceleration: a path to the future of high-energy particle physics. *Plasma Physics and Controlled Fusion*, 56(8):084013.

[1963b] Asundi, K. K. and Kurepa, M. V. (1963). Ionization cross sections in He, Ne, Ar, Kr and Xe by electron impact. *Journal of Electronics and Control*, 15(1):41–50.

[Baeva et al., 2012] Baeva, M., Kozakov, R., Gorchakov, S., and Uhrlandt, D. (2012). Two temperature chemically non equilibrium modelling of transferred arcs. *Plasma Sources Science and Technology*, 21(5):055027.

[Barbalat, 1994] Barbalat, O. (1994). Applications of particle accelerators.

[Belikov et al., 1995] Belikov, A. E., Kusnetsov, O. V., and Sharafutdinov, R. G. (1995). The rate of collisional quenching of $N_2O^+(B^2\sum)$, $N_2^+(B^2\sum)$, $O_2^+(b^4\sum)$, $O^+(3d)$, $O(3p)$, $Ar^+(4p')$, $Ar(4p,4p')$ at the temperature $\leqslant$ 200 K. *The Journal of Chemical Physics*, 102(7):2792.

[Bingham et al., 2004] Bingham, R., Mendonca, J., and Shukla, P. (2004). Plasma based charged-particle accelerators. *Plasma Phys. Contr. Fusion*, 46:R1.

[Blumenfeld et al., 2007] Blumenfeld, I. et al. (2007). Energy doubling of 42 GeV electrons in a metre-scale plasma wakefield accelerator. *Nature Physics*, 445:741–744.

[1961b] Bockasten, K. (1961). Transformation of observed radiances into radial distribution of the emission of a plasma. *J. Opt. Soc. Am.*, 51(9):943–947.

[Bogaerts et al., 2002] Bogaerts, A., Neyts, E., Gijbels, R., and van der Mullen, J. (2002). Gas discharge plasmas and their applications. *Spectrochimica Acta Part B: Atomic Spectroscopy*, 57(4):609 − 658.

[1949b] Bohm, D. (1949). *The Characteristics of Electrical Discharges in Magnetic fields*. McGraw-Hill, New York.

[Boivin et al., 2001] Boivin, R. F., Kline, J. L., and Scime, E. E. (2001). Electron temperature measurements by a helium line intensity ratio method in helicon plasmas. *Physics of plasmas*, 8:5303.

[Boivin, 2003] Boivin, R. F. and Scime, E. E. (2003). Laser induced fluorescence in Ar and He plasmas with a tunable diode laser. *Review of Scientific Instruments*, 74(10):4352.

[Boswell, 1984] Boswell, R. W. (1984). Very efficient plasma generation by whistler waves near the lower hybrid frequency. *Plasma Physics and Controlled Fusion*, 26(10):1147–1162.

[Braithwaite, 2000] Braithwaite, N. (2000). Introduction to gas discharges. *Plasma Sources Sci. Technol.*, 9:517–527.

[1986] Bretagne, J., Callede, G., Legentil, M., and Puech, V. (1986). Relativistic electron beam produced plasmas. ii. energy apportionment and plasma formation. *Journal of Physics D: Applied Physics*, 19(5):779.

[Buttenschön et al., 2018] Buttenschön, B., Fahrenkamp, N., and Grulke, O. (2018). A high power, high density helicon discharge for the plasma wakefield accelerator experiment AWAKE. *Plasma Physics and Controlled Fusion*, 60(7):075005.

[Buttenschön et al., 2013] Buttenschön, B., Kempkes, P., Grulke, O., and Klinger, T. (2013). A helicon plasma source as a prototype for a proton-driven plasma wakefield accelerator. *Proceedings of 40th EPS Conference on Plasma Physics (Espoo, Finland, 2013)*, page P2.208.

[Buttenschön et al., 2014] Buttenschön, B., Kempkes, P., Grulke, O., and Klinger, T. (2014). A high power helicon discharge as a plasma cell for future plasma wakefield accelerators. *Proceedings of 41st EPS Conference on Plasma Physics (Berlin, Germany, 2014)*, page P2.102.

[Caldwell et al., 2016] Caldwell, A. et al. (2016). Path to awake : evolution of the concept. *Nuclear Instruments and Methods in Physics Research Section A: Accelerators, Spectrometers, Detectors and Associated Equipment*.

[Caldwell et al., 2009] Caldwell, A., Lotov, K., Pukhov, A., and Simon, F. (2009). Proton-driven plasma-wakefield acceleration. *Nature Physics*, 5:363.

[Carbajo et al., 2015] Carbajo, S. et al. (2015). Direct laser acceleration of electrons in free-space. *ArXiv*.

[Caron, 1993] Caron, J.-L. (1993). The LHC injection complex. L'ensemble d'injection du LHC. AC Collection. Legacy of AC. Pictures from 1992 to 2002.

[Chakraborty et al., 2012] Chakraborty, T. S. et al. (2012). Laser induced fluorescence measurements of ion velocity and temperature of drift turbulence driven sheared plasma flow in a linear helicon plasma device. *Physics of Plasmas*, 19(8):082102.

[1971] Chan, Y. W. (1971). Ultraintense laser radiation as a possible energy booster for relativistic charged particle. *Phys. Lett. A*, 35:305.

[Chen, 1984] Chen, F. F. (1984). *Introduction to Plasma Physics and Controlled Fusion*. Plenum Press, New York.

[Chen, 2015] Chen, F. F. (2015). Helicon discharges and sources: a review. *Plasma Sources Science and Technology*, 24(1):014001.

[Chen, 1997] Chen, F. F. and Arnush, D. (1997). Generalized theory of helicon waves. I. Normal modes. *Physics of Plasmas (1994-present)*, 4(9):3411–3421.

[Chen et al., 1985] Chen, P., Dawson, J., Huff, R., and Katsouleas, T. (1985). Acceleration of electrons by the interaction of a bunched electron beam with a plasma. *Phys. Rev. Lett.*, 54:693–696.

[Conrads and Schmidt, 2000] Conrads, H. and Schmidt, M. (2000). Plasma generation and plasma sources. *Plasma Sources Sci. Technol.*, 9:441–454.

[Dahler et al., 1962] Dahler, J. S., Franklin, J. L., Munson, M. S. B., and Field, F. H. (1962). Rare-Gas Molecule-Ion Formation by Mass Spectrometry. Kinetics of Ar_2^+, Ne_2^+, and He_2^+ Formation by Second- and Third-Order Processes. *The Journal of Chemical Physics*, 36(12):3332.

[2017] De Micheli, E. (2017). A fast algorithm for the inversion of abel's transform. *Applied Mathematics and Computation*, 301:12 – 24.

[Donley et al., 2005] Donley, E. A. et al. (2005). Double-pass acousto-optic modulator system. *Review of Scientific Instruments*, 76(6):063112.

[1963] Drawin, H. (1963). Zur spektroskopischen Temperatur und Dichtemessung von Plasmen bei Abwesenheit thermodynamischen Gleichgewichtes. *Zeitschrift für Physik*, 172(4):429–452.

[1961] Drawin, H. W. (1961). Zur formelmäßigen Darstellung der Ionisierungsquerschnitte gegenüber Elektronenstoß. *Zeitschrift für Physik*, 164(5):513–521.

[EG CERN, 2017] Education, Communications and Outreach Group (2017). LHC the guide.

[Elson, 1996] Elson, E. and Rokni, M. (1996). An investigation of the secondary electron kinetics and energy distribution in electron-beam-irradiated argon. *Journal of Physics D: Applied Physics*, 29(3):716.

[Esarey et al., 2009] Esarey, E., Schroeder, C. B., and Leemans, W. P. (2009). Physics of laser-driven plasma-based electron accelerators. *Rev. Mod. Phys.*, 81:1229–1285.

[Esarey et al., 1996] Esarey, E., Sprangle, P., Krall, J., and Ting, A. (1996). Overview of plasma-based accelerator concepts. *IEEE Trans. Plasma Sci.*, 24:252–288.

[1949] Fermi, E. (1949). On the origin of the cosmic radiation. *Phys. Rev.*, 75:1169.

[Franck, 2003] Franck, C. M. (2003). *Experiments on Whistler Wave Dispersion in Bounded Magnetised Plasmas*. PhD thesis, Universität Greifswald.

[Franklin] Franklin, J. L. (1972). *Ion-Molecule Reactions, Volume 2*. Plenum Press, New York.

[Freegarde, 1997] Freegarde, T. G. M. and Hancock, G. (1997). A Guide to Laser-Induced Fluorescence Diagnostics in Plasmas. *Le Journal de Physique IV*, 07(C4):C4–15–C4–29.

[Fridman, 2011] Fridman, A. and Kennedy, L. A. (2011). *Plasma physics and Engeneering, Second edition*. CRC Press.

[RP-Photonics GmbH, 2018] GmbH, R. P. C. Acousto-optic modulators. `https://www.rp-photonics.com/acousto_optic_modulators.html`. Accessed: 2018-06-08.

[Gochelashvily et al., 1992] Gochelashvily, K., Demyanov, A., Kochetov, I., and Yangurazova, L. (1992). Fluorescence model of noble gas dimers in pulsed self-sustained discharges. *Optics Communications*, 91:66–70.

[Goeckner, 1989] Goeckner, M. J. and Goree, J. (1989). Laser-induced fluorescence measurement of plasma ion temperatures: Corrections for power saturation. *Journal of Vacuum Science & Technology A*, 7(3):977–981.

[Goeckner et al., 1993] Goeckner, M. J., Goree, J., and Sheridan, T. E. (1993). Saturation broadening of laser-induced fluorescence from plasma ions. *Review of Scientific Instruments*, 64(4):996.

[Gooch, 2018] Gooch and Housego. Introduction to acousto-optic modulators and deflectors.

[Grill, 1994] Grill, A. (1994). *Cold plasmas in Materials Fabrication: From fundamentals to applications*. IEEE Press, New-York.

[Gschwendtner et al., 2016] Gschwendtner, E. et al. (2016). Awake, the advanced proton driven plasma wakefield acceleration experiment at cern. *Nuclear Instruments and Methods in Physics Research Section A: Accelerators, Spectrometers, Detectors and Associated Equipment*, 829(Supplement C):76 – 82. 2nd European Advanced Accelerator Concepts Workshop - EAAC 2015.

[Gudmundsson, 2001] Gudmundsson, J. T. (2001). On the effect of the electron energy distribution on the plasma parameters of an argon discharge: a global (volume-averaged) model study. *Plasma Sources Science and Technology*, 10(1):76.

[Haken, 1987] Haken, H. and Wolf, H. C. (1987). *Atomic and Quantum Physics: An Introduction to the Fundamentals of Experiment and Theory*. Springer-Verlag, Berlin.

[Hardin et al., 2004] Hardin, R., Sun, X., and Scime, E. E. (2004). Three-dimensional laser-induced fluorescence measurements in a helicon plasma. *Review of Scientific Instruments*, 75(10):4103–4105.

[1959] Harrison, E. R. and Thompson, W. B. (1959). The low pressure plane symmetric discharge. *Proceedings of the Physical Society*, 74(2):145.

[Hartfuss et al., 1997] Hartfuss, H. J. et al. (1997). Heterodyne methods in millimetre wave plasma diagnostics with applications to ece, interferometry and reflectometry. *Plasma Physics and Controlled Fusion*, 39(11):1693–1769.

[Heiermann, 2002] Heiermann, J. (2002). *Ein Finite Volumen Verfahren zur Lösung magnetoplasmadynamischer Erhaltungsgleichungen.* PhD thesis, Universität Stuttgart.

[1967] Hoffert, M. I. and Lien, H. (1967). Quasi one dimensional, nonequilibrium gas dynamics of partially ionized two temperature argon. *The Physics of Fluids*, 10(8):1769–1777.

[Hogan et al., 2005] Hogan, M. J. et al. (2005). Multi-GeV energy gain in a plasma-wakefield accelerator. *Phys. Rev. Lett.*, 95.

[Holzer, 2017] Holzer, B. J. (2017). Introduction to particle accelerators and their limitations. *ArXiv*.

[Hopkins, 2000] Hopkins, M. B. and Lawler, J. F. (2000). Plasma diagnostics in industry. *Plasma Physics and Controlled Fusion*, 42(12B):B189.

[ILC, 2018] International linear collider. Specifications of ILC accelerator. `http://www.linearcollider.org/pdf/ILC_Accelerator_bynumbers.pdf`. Accessed: 2018-05-04.

[1924] Ising, G. (1924). Prinzip einer Methode zur Herstellung von Kanalstrahlen hoher Voltzahl. *Ark. Mat. Astron. Fys.*, 18(30):1–4.

[Jones et al., 1959] Jones, P. R., Ziemba, F. P., Moses, H. A., and Everhart, E. (1959). Total Cross Sections for Multiple Electron Stripping in Atomic Collisions at Energies to 100 keV. *Physical Review*, 113(1):182.

[Joshi et al., 1984] Joshi, C. et al. (1984). Ultrahigh gradient particle acceleration by intense laser-driven plasma density waves. *Nature Physics*, 311:525–529.

[Joshi, 2003] Joshi, C. and Katsouleas, T. (2003). Plasma accelerators at the energy frontier and on tabletops. *Phys. Today*, 56:47–53.

[Kannari et al., 1985] Kannari, F., Obara, M., and Fujioka, T. (1985). An advanced kinetic model of electron-beam-excited KrF lasers including the vibrational relaxation in KrF·(B) and collisional mixing of KrF·(B,C). *Journal of Applied Physics*, 57(9):4309.

[Kano et al., 2000] Kano, K., Suzuki, M., and Akatsuka, H. (2000). Spectroscopic measurement of electron temperature and density in argon plasmas based on collisional-radiatve model. *Plasma sources Sci. Technol.*, 9:314–322.

[Keesee, 2007] Keesee, A. M. and Scime, E. E. (2007). Neutral density profiles in argon helicon plasmas. *Plasma Sources Science and Technology*, 16(4):742.

[Keesee et al., 2004] Keesee, A. M., Scime, E. E., and Boivin, R. F. (2004). Laser-induced fluorescence measurements of three plasma species with a tunable diode laser. *Review of Scientific Instruments*, 75(10):4091–4093.

[Kelley et al., 1972] Kelley, G. G., Morgan, O., Stewart, L., Stirling, W., and H.K. Forsen, H. (1972). Neutral-beam-injection heating of toroidal plasmas for fusion research. *Nuclear Fusion*, 12(2):169.

[Kumar et al., 2010] Kumar, N., Pukhov, A., and Lotov, K. (2010). Self-modulation instability of a long proton bunch in plasmas. *Physical Review Letters*, 104(25).

[Kwak et al., 2000] Kwak, J. G. et al. (2000). Upper limit to the monotonic increasing dependence of the plasma density on the magnetic field in helicon discharges. *Physics Letters A*, 267(5-6):384–388.

[Lam] Lam, S. K., Zheng, C. E., Lo, D., Dem'yanov, A., and Napartovich, A. P. (2000). Kinetics of Ar* 2 in high-pressure pure argon. *Journal of Physics D: Applied Physics*, 33(3):242.

[1928] Langmuir, I. (1928). Oscillations in ionized gases. *Proceedings of the National Academy of Sciences of the United States of America*, 14(8):627–637.

[1929] Langmuir, I. (1929). The interaction of electron and positive ion space charges in cathode sheaths. *Phys. Rev.*, 33:954–989.

[Lawless, 1995] Lawless, J. L. and Lo, D. (1995). Comprehensive kinetic model for electron-beam-excited $XeCs^+$ ionic excimers. *Applied Physics B*, 60(4):391–403.

[Lee, 1995] Lee, C. (1995). Global model of Ar, O_2, Cl_2, and Ar/O_2 high-density plasma discharges. *Journal of Vacuum Science & Technology A: Vacuum, Surfaces, and Films*, 13(2):368.

[Lee et al., 2017] Lee, H.-C. et al. (2017). Evolution of electron temperature in inductively coupled plasma. *Applied Physics Letters*, 110(1):014106.

[Leemans et al., 2006] Leemans, W. et al. (2006). GeV electron beams from a centimetre-scale accelerator. *Nature Phys.*, 2:696–699.

[1988b] Lennon, M. A. et al. (1988). Recommended data on the electron impact ionization of atoms and ions: Fluorine to nickel. *Journal of Physical and Chemical Reference Data*, 17(3):1285–1363.

[Lichtenberg, 2005] Lichtenberg, A. J. and Lieberman, M. A. (2005). *Principles of plasma discharges and Material processing*. John-Wiley and Sons.

[Lieberman] Lieberman, M. A. (2003). *A Mini-Course on the principles of plasma discharges*.

[Light, 1995] Light, M. and Chen, F. F. (1995). Helicon wave excitation with helical antennas. *Physics of plasmas*, 2(4):1084–1093.

[2014] Litos, M. et al. (2014). High-efficiency acceleration of an electron beam in a plasma wakefield accelerator. *Nature Physics*, 515:92.

[2007] Loch, S. D., Abdel-Naby, S. A., Ballance, C. P., and Pindzola, M. S. (2007). Electron-impact ionization and recombination of M -shell atomic ions in the argon isonuclear sequence. *Physical Review A*, 76(2).

[LANLa] Los Alamos National Laboratory. Los Alamos Argon Atomic Data Sets. `https://www-amdis.iaea.org/LANL/argon/`. Accessed: 2015-12-01.

[LANLb] Los Alamos National Laboratory. Los Alamos Atomic Physics Codes. `http://aphysics2.lanl.gov/tempweb/lanl/`. Accessed: 2015-11-20.

[Lotov, 2010] Lotov, K. (2010). Simulation of proton driven plasma wakefield acceleration. *Phys. Rev. ST Accel. Beams*, 13:041301.

[Lotov et al., 2013a] Lotov, K., Sosedkin, A., and Mesyats, E. (2013a). Simulation of self-modulating particle beams in plasma wakefield accelerators. *Proceedings, 4th International Particle Accelerator Conference (IPAC 2013): Shanghai, China, May 12-17*, page TUPEA048.

[Lotov, 2015] Lotov, K. V. (2015). Physics of beam self-modulation in plasma wakefield accelerators. *Physics of Plasmas*, 22(10):103110.

[Lotov et al., 2013b] Lotov, K. V. et al. (2013b). Natural noise and external wakefield seeding in a proton-driven plasma accelerator. *Phys. Rev. ST Accel. Beams*, 16:041301.

[Lotov et al., 2013c] Lotov, K. V., Pukhov, A., and Caldwell, A. (2013c). Effect of plasma inhomogeneity on plasma wakefield acceleration driven by long bunches. *Physics of Plasmas*, 20(1):013102.

[1967b] Lotz, W. (1967). An empirical formula for the electron impact ionization cross-section. *Zeitschrift für Physik*, 206(2):205–211.

[1968] Lotz, W. (1968). Electron impact ionization cross sections and ionization rate coefficients for atoms and ions from hydrogen to calcium. *Zeitschrift für Physik*, 216(3):241–247.

[Lu et al., 2005] Lu, W. et al. (2005). Limits of linear plasma wakefield theory for electron or positron beams. *Phys. Plasmas*, 12:063101.

[1974] Maxwell, B. R. and Wessling, F. C. (1974). Expansion of partially ionized argon through a supersonic nozzle. *The Physics of Fluids*, 17(2):493–495.

[1950] McMillan, E. M. (1950). The origin of cosmic rays. *Phys. Rev.*, 79:498.

[1990b] Meyyappan, M. and Kreskovsky, J. P. (1990). Glow discharge simulation through solutions to the moments of the Boltzmann transport equation. *Journal of Applied Physics*, 68(4):1506.

[Molvik et al., 1997] Molvik, A. W. et al. (1997). Hot-electron production and wave structure in a helicon plasma source. *Physical Review Letters*, 79(2):233–236.

[Muggli, 2009] Muggli, P. and Hogan, M. J. (2009). Review of high-energy plasma wakefield experiments. *Comptes Rendus Physique*, 10:116.

[NIST] National Institute of Standards and Technology. NIST Atomic Spectra Database Lines. `http://physics.nist.gov/PhysRefData/ASD/lines_form.html`. Accessed: 2015-10-12.

[Neeser] Neeser, S., Kunz, T., and Langhoff, H. (1997). A kinetic model for the formation of excimers. *Journal of Physics D: Applied Physics*, 30(10):1489.

[1960] Nestor, O. and Olsen, H. (1960). Numerical methods for reducing line and surface probe data. *SIAM Review*, 2(3):200–207.

[Öz, 2014] Öz, E. and Muggli, P. (2014). A novel Rb vapor plasma source for plasma wakefield accelerators. *Nuclear Instruments and Methods in Physics Research Section A: Accelerators, Spectrometers, Detectors and Associated Equipment*, 740(Supplement C):197 – 202. Proceedings of the first European Advanced Accelerator Concepts Workshop 2013.

[1972] Palmer, R. B. (1972). Interaction of relativistic particles and free electromagnetic waves in the presence of a static helical magnet. *J. Appl. Phys.*, 43:3014.

[Palomares et al., 2013] Palomares, J., Graef, W., Hübner, S., and van der Mullen, J. (2013). Time resolved laser induced fluorescence on argon intermediate pressure microwave discharges: Measuring the depopulation rates of the 4p and 5p excited levels as induced by electron and atom collisions. *Spectrochimica Acta Part B: Atomic Spectroscopy*, 88:156–166.

[1993] Passchier, J. D. P. and Goedheer, W. J. (1993). A two dimensional fluid model for an argon rf discharge. *Journal of Applied Physics*, 74(6):3744–3751.

[Peerenboom et al., 2010] Peerenboom, K. S. C., Goedheer, W. J., van Dijk, J., and van der Mullen, J. J. A. M. (2010). Integral simulation of the creation and expansion of a transonic argon plasma. *Plasma Sources Science and Technology*, 19(2):025009.

[1992] Pretzler, G. et al. (1992). Comparison of Different Methods of Abel Inversion Using Computer Simulated and Experimental Side-On Data. *Zeitschrift Naturforschung Teil A*, 47:955–970.

[Puerta, 1985] Puerta, J. and Huber, B. A. (1985). Single electron capture by state-prepared Ar^{2+} projectiles in Ar. *Journal of Physics B: Atomic and Molecular Physics*, 18(22):4445.

[Pukhov et al., 2011] Pukhov, A. et al. (2011). Phase velocity and particle injection in a self-modulated proton-driven plasma wakefield accelerator. *Phys. Rev. Lett.*, 107:145003.

[Pukhov et al., 2012] Pukhov, A. et al. (2012). Principles of self-modulated proton driven plasma wake field acceleration. *AIP Conference Proceedings*, 1507(1):103–110.

[Raju, 2004] Raju, G. G. (2004). Electron-atom collision cross sections in argon: an analysis and comments. *IEEE Transactions on Dielectrics and Electrical Insulation*, 11(4):649–673.

[Riemann, 1991] Riemann, K.-U. (1991). The bohm criterion and sheath formation. *Journal of Physics D: Applied Physics*, 24(4):493.

[1988] Rosenzweig, J. B. et al. (1988). Experimental observation of plasma wakefield acceleration. *Phys. Rev. Lett.*, 61:98–101.

[Roston, 2012] Roston, G. D. and Helmi, M. S. (2012). Temperature dependence of the pressure broadening of spectral lines. *Journal of Physics: Conference Series*, 397:012041.

[Ruth et al., 1985] Ruth, R., Chao, A., Morton, P., and Wilson, P. (1985). A plasma wake field accelerator. *Particle Accelerators*, 17:171–189.

[USdoe, 2018] S. departement of energy, U. The benefits of particle accelerators for society. http://www.acceleratorsamerica.org/files/AcceleratorsFactSheet_102309_Final.pdf. Accessed: 2018-05-17.

[2001] Scheubert, P. (2001). *Modelling and Diagnostics of Low Pressure Plasma Discharges*. PhD thesis, Technische Universität München.

[Schmidt et al., 2015] Schmidt, J., Upadhyay, P. P., Herdrich, G., and Bauder, U. (2015). Review of reaction rate coefficients of non-equilibrium argon for electron impact ionization. *University of Stuttgart, Institute of space systems*.

[1924b] Schottky, W. (1924). Diffusionstheorie der positiven Säule. *Phys. Zeitschr.*, 25(342):635.

[Schroeder et al., 2011] Schroeder, C. B. et al. (2011). Growth and phase velocity of self-modulated beam-driven plasma waves. *Phys. Rev. Lett.*, 107:145002.

[Schulz-von der Gathen, 1996] Schulz-von der Gathen, V. and Döbele, H. F. (1996). Critical comparison of emission spectroscopic determination of dissociation in hydrogen rf discharges. *Plasma Chemistry and Plasma Processing*, 16(4):461–486.

[Scime et al., 2005] Scime, E. et al. (2005). Laser induced fluorescence in a pulsed argon plasma. *Review of Scientific Instruments*, 76(2):026107.

[Scime et al., 1998] Scime, E., Keiter, P. A., et al. (1998). Control of ion temperature anisotropy in a helicon plasma. *Plasma Sources Sci. and Technol.*, 7:186–191.

[Severn et al., 1998] Severn, G. D., Edrich, D. A., and McWilliams, R. (1998). Argon ion laser-induced fluorescence with diode lasers. *Review of Scientific Instruments*, 69(1):10.

[Shamrai, 1996] Shamrai, K. P. and Taranov, V. B. (1996). Volume and surface rf power absorption in a helicon plasma source. *Plasma Sources Science and Technology*, 5(3):474–491.

[Shimada] Shimada, M., Tynan, G. R., and Cattolica, R. (2008). Neutral depletion in inductively coupled plasmas using hybrid-type direct simulation Monte Carlo. *Journal of Applied Physics*, 103(3):033304.

[1990] Simpson, S. W. (1990). Ionisation and recombination rates in argon plasmas. *Journal of Physics D: Applied Physics*, 23(9):1161.

[2010] Singh, O. P., Singh, V. K., and Pandey, R. K. (2010). A stable numerical inversion of abel's integral equation using almost bernstein operational matrix. *Journal of Quantitative Spectroscopy and Radiative Transfer*, 111(1):245 – 252.

[1988c] Smith, L. M., Keefer, D. R., and Sudharsanan, S. I. (1988). Abel inversion using transform techniques. *Journal of Quantitative Spectroscopy and Radiative Transfer*, 39(5):367 – 373.

[1930] Smith, P. T. (1930). The ionization of helium, neon, and argon by electron impact. *Physical Review*, 36:1293–1302.

[Sobel'man et al., 1995] Sobel'man, I. I., Vainshtein, L. A., and Yukov, E. A. (1995). *Excitation of Atoms and Broadening of Spectral Lines*. Springer-Verlag, Heidelberg.

[Spitzer, 1958] Spitzer, L. (1958). The stellarator concept. *The Physics of Fluids*, 1(4):253–264.

[Stark, 2006] Stark, A. (2006). *Ion dynamics in magnetized plasmas*. PhD thesis, Ernst-Moritz-Arndt-Universität Greifswald.

[Stark et al., 2006] Stark, A. et al. (2006). Phase-resolved measurements of ion dynamics with laser-induced fluorescence. *Physica Scripta*, T122:8–10.

[Stefanović] Stefanović, I., Kuschel, T., Schröter, S., and Böke, M. (2014). Argon metastable dynamics and lifetimes in a direct current microdischarge. *Journal of Applied Physics*, 116(11):113302.

[Stephan, 1985] Stephan, K. and Märk, T. D. (1985). Metastable dissociation of Ar_2^+ produced by associative ionization. *Physical Review A*, 32(3):1447–1450.

[1994] Stewart, R. A., Vitello, P., and Graves, D. B. (1994). Two dimensional fluid model of high density inductively coupled plasma sources. *Journal of Vacuum Science & Technology B: Microelectronics and Nanometer Structures Processing, Measurement, and Phenomena*, 12(1):478–485.

[Stix, 1958] Stix, T. H. (1958). Generation and thermalization of plasma waves. *The Physics of Fluids*, 1(4):308–317.

[1986b] Tachibana, K. (1986). Excitation of the $1s^5$, $1s^4$, $1s^3$, and $1s^2$ levels of argon by low-energy electrons. *Physical Review A*, 34(2):1007.

[Tajima, 1979] Tajima, T. and Dawson, J. M. (1979). Laser electron accelerator. *Phys. Rev. Lett.*, 43:267–270.

[Thompson, 1982] Thompson, D. L. (1982). Trimer formation, atom exchange, and dissociation in argon dimer collisions. *The Journal of Chemical Physics*, 77(3):1269.

[1912] Thomson, S. J. (1912). Xlii. ionization by moving electrified particles. *Philosophical Magazine*, 23(136):449–457.

[1929b] Tonks, L. and Langmuir, I. (1929). A general theory of the plasma of an arc. *Phys. Rev.*, 34:876–922.

[Turner, 1979] Turner, D. L. and Conway, D. C. (1979). Study of the $2Ar + Ar^{2+} = Ar + Ar^{3+}$ reaction. *The Journal of Chemical Physics*, 71(4):1899.

[Turner et al., 2016] Turner, M. et al. (2016). Indirect self-modulation instability measurement concept for the awake proton beam. *Nuclear Instruments and Methods in Physics Research Section A: Accelerators, Spectrometers, Detectors and Associated Equipment*, 829(Supplement C):314 – 317. 2nd European Advanced Accelerator Concepts Workshop - EAAC 2015.

[Vaseghi, 2000] Vaseghi, S. V. (2000). *Advanced Digital Signal Processing and Noise Reduction*. Wiley and Sons, Chichester, 2nd edition.

[Vieira et al., 2012a] Vieira, J. et al. (2012a). Transverse self-modulation of ultra-relativistic lepton beams in the plasma wakefield accelerator. *Phys. Plasmas*, 19:063105.

[Vieira et al., 2012b] Vieira, J., Fonseca, R. A., Mori, W. B., and Silva, L. O. (2012b). Ion motion in self-modulated plasma wakefield accelerators. *Phys. Rev. Lett.*, 109:145005.

[Vivek, 1999] Vivek, V. (1999). Optical switches.

[Vlcek, 1986] Vlcek, J. and Pelikan, V. (1986). Excited level populations of argon atoms in a non isothermal plasma. *Journal of Physics D: Applied Physics*, 19(10):1879.

[1973] Vriens, L. (1973). Energy balance in low pressure gas discharges. *Journal of Applied Physics*, 44(9):3980–3989.

[Wainman et al., 1995] Wainman, P. N., Lieberman, M. A., Lichtenberg, A. J., Stewart, R. A., and Lee, C. (1995). Characterization at different aspect ratios (radius/length) of a radio frequency inductively coupled plasma source. *Journal of Vacuum Science & Technology A: Vacuum, Surfaces, and Films*, 13(5):2464–2469.

[Wanless, 1971] Wanless, D. (1971). Electron-ion recombination in argon. *Journal of Physics B: Atomic and Molecular Physics*, 4(4):522.

[Wegner, 2010] Wegner, T. Vergleich von Leistungs- und Teilchenbilanzrechnung mit RF-Entladungen im Experiment VINETA. Bachelor Thesis, Universität Greifswald, 2010.

[Weiglein, 2004] Weiglein, G. (2004). Physics interplay of the LHC and the ILC. *ArXiv*.

[1987] Wetzel, R. C., Baiocchi, F. A., Hayes, T. R., and Freund, R. S. (1987). Absolute cross sections for electron impact ionization of the rare-gas atoms by the fast neutral beam method. *Phys. Rev. A*, 35:559–577.

[1928b] Wideröe, R. (1928). Über ein neues Prinzip zur Herstellung hoher Spannungen. *Archiv für Elektrotechnik*, 21(4):387–406.

[Wiese et al., 1966] Wiese, W. L., Smith, M. W., and Glennon, B. M. (1966). Atomic transitions probabilities. *National Standard Reference Data Systems*, Vol. 1.

[1975] Willis, W. J. (1975). A new collective-field acceleration mechanism using a powerful laser. CERN report, number 75-9.

[Zhang et al., 2011] Zhang, N., Sun, F., Zhu, L., et al. (2011). Electron temperature and density of the plasma measured by optical emission spectroscopy in vlpps conditions. *Journal of Thermal spray technology*, 20(6):1321.

[Zohm, 2012] Zohm, H. (2012). Plasmaphysik. Vorlesungsskript an der LMU München, 2012. `https://www.physik.uni-muenchen.de/lehre/vorlesungen/wise_15_16/A_Plasmaphysik/vorlesung/skript.pdf` Accessed: 2015-08-31.

Eigenständigkeitserklärung

Hiermit erkläre ich, dass diese Arbeit bisher von mir weder an der Mathematisch-Naturwissenschaftlichen Fakultät der Universität Greifswald noch einer anderen wissenschaftlichen Einrichtung zum Zwecke der Promotion eingereicht wurde. Ferner erkläre ich, dass ich diese Arbeit selbstständig verfasst und keine anderen als die darin angegebenen Hilfsmittel und Hilfen benutzt und keine Textabschnitte eines Dritten ohne Kennzeichnung übernommen habe.

_____

Unterschift des Promovenden

Curriculum Vitae

Nils Fahrenkamp

Personal Information

BIRTH:	Lehrte, Germany │ 28. November 1988
ADDRESS:	Nikolaikirchplatz 2, 17489 Greifswald
PHONE:	+49 3834 881903
EMAIL:	nils.fahrenkamp@web.de

Work Experience

Since 10/2018

Research Associate
UNIVERSITY OF GREIFSWALD & MAX-PLANCK INSTITUTE FOR PLASMA PHYSICS
- Preparation and execution of experiments in plasma physics
- Analysis and documentation of complex measurement data
- Investigation of particle dynamics in magnetized plasmas with laser spectroscopy
- Supervision and evaluation of the practical physics course
- Organization and instruction of seminars and excercises
- Maintenance and improvements in the laboratory

04/2014 - 09/2017

Physicist (PhD)
MAX-PLANCK INSTITUTE FOR PLASMA PHYSICS & UNIVERSITY OF GREIFSWALD
- Preparation, execution and analysis of experiments in plasma physics
- Investigation of neutral and charged particle dynamics in magnetized plasmas with laser diagnostics
- Setup and installation of data aquisition electronics
- Programming of data aquisition and analysis routines in LABVIEW and MATLAB
- Editing e.g. in LaTeX and presentation of results at conferences
- Maintenance of the gas or vacuum systems and electronics
- Supervision and evaluation of students and interns
- Talks and tours at the institute for visitors

01/2014

Intern
MAX-PLANCK INSTITUTE FOR PLASMA PHYSICS
- Setup of a laser-induced fluorescence system
- Investigation of plasma dynamics during magnetic reconnection

ACADEMICAL EDUCATION

10/2011 - 09/2013	**Master of Science (Physics)** UNIVERSITY OF ROSTOCK *Thesis: Radiaton due to collective laser plasma dynamics:* *analytical modelling and PIC-simulations* • Focus: molecules, clusters and plasmas • Supervision of practical courses in physics • Grade: 1.4
10/2008 - 09/2011	**Bachelor of Science (Physics)** UNIVERSITY OF ROSTOCK *Thesis: Particle-In-Cell simulations of intense laser-matter* *interaction* • Focus: theoretical and experimental physics, mathematics • Elective course: chemics, computer science • Grade: 1.7

EDUCATION

09/2000 - 07/2008	**Higher Education Entrance Qualification (Abitur)** LILIENTHAL GYMNASIUM ANKLAM • Advanced course: english, mathematics • Grade: 1.5

SELF-IMPROVEMENT

06/2018	**Electrically Instructed Person** TÜV-NORD AKADEMIE
06/2015	**Scientific Communication** HEATHER SILYN-ROBERTS / UNIVERSITY OF AUCKLAND
12/2014	**Time- and Self-Management** ROB THOMPSON / RTTA
11/2014	**Improved Reading** FRIEDRICH HASSE / IMPROVED READING OST, BERLIN

LANGUAGES

GERMAN:	Native speaker
ENGLISH:	Fluent
FRENCH:	Very basic

COMPUTER SKILLS

Proficient:	MATLAB
Capable:	C, C++, LABVIEW
Basic Knowledge:	PYTHON, CAD
Others:	UNIX Systems, Microsoft Office, LaTeX, INKSCAPE, GIMP

List of publications

Journal articles

- Buttenschön, B., Fahrenkamp, N., and Grulke, O. (2018). A high power, high density helicon discharge for the plasma wakefield accelerator experiment AWAKE. *Plasma Physics and Controlled Fusion*, 60(7):075005

Conference oral presentations

- Fahrenkamp, N., Buttenschön, B., and Grulke, O. (2017). Argon lif measurements in a high-power helicon discharge. *Verhandlungen der Frühjahrstagung der Deutschen Physikalischen Gesellschaft, Bremen, Germany*, (P 28.4)

Conference poster presentations

- Fahrenkamp, N., Buttenschön, B., and Grulke, O. (2015). Neutral argon measurements in a high-power helicon discharge. *Verhandlungen der Frühjahrstagung der Deutschen Physikalischen Gesellschaft, Bochum, Germany*, (P 16.3)

- Fahrenkamp, N., Buttenschön, B., and Grulke, O. (2016). Neutral argon measurements in a high-power helicon discharge. *Verhandlungen der Frühjahrstagung der Deutschen Physikalischen Gesellschaft, Hannover, Germany*, (P 5.20)

Danksagung

An dieser Stelle möchte ich mich bei all denjenigen Personen bedanken, die mich unterstützt und es mir ermöglicht haben diese Dissertation anzufertigen. Für die Möglichkeit am Max-Planck-Institut meine Arbeit anzufertigen, das interessante Thema, das sich über die Jahre der Arbeit auch thematisch ein wenig geändert hat, die fachlichen Gespräche und Hilfestellungen und für die Betreuung gilt mein Dank Prof. Dr. Olaf Grulke. Desweiteren möchte ich mich bei Prof. Dr. Thomas Klinger bedanken, der immer ein offenes Ohr hatte, mit Prof. Grulke die gesamte Arbeit Probegelesen, viel Zeit investiert und zusammen mit der gesamten VINETA- und E5-Gruppe ein angenehmes, freundschaftliches Arbeitsklima geschaffen hat, das zusätzlich mit dem lockeren Umgang untereinander positiv zum Verständnis komplizierter Sachverhalte beitrug. Des Weiteren sei auch insbesondere Dr. Adrian von Stechow und Dr. Buttenschön gedankt, die mir bei etwaigen elektro-technischen oder programmierbasierten Problemen im Labor oder Büro immer mit Rat und Tat zur Seite standen. Ein weiterer besonderer Dank gilt meiner Familie, die mich auf diesem, doch auch steinigen Weg, immer unterstützt haben und bestimmt froh sind, dass dieser jahrzehntelange, mit der Schule startende Ausbildungsmarathon ein Ende nimmt.